POLITECNICO DI MILANO

School of Industrial and Information Engineering

Department of Electronics, Information and Bioengineering

Master of Science in

Biomedical Engineering

Hemodynamic changes due to valve sparing surgery in ascending thoracic aortic aneurysm correction: a tailored multi-patient analysis exploiting the Coupled Momentum Method for Fluid-Solid Interaction

Supervisor:

Alberto Redaelli, PhD

Cosupervisor:

Alessandro Caimi, PhD

Simone Saitta, MSc

Jonathan Weinsaft, MD

Author of the thesis:

Valentina Scarponi

ID.916059

Academic Year 2019-2020

Contents

Sommario

Introduzione

L'aneurisma dell'arco aortico colpisce ogni anno tra le 5 e le 10 persone ogni 100000 abitanti[1–3], posizionandosi al diciannovesimo posto tra le cause di morte più diffuse al mondo [4, 5]. Circa il 60% degli aneurismi toracici interessa il tratto dell'aorta ascendete. Le linee guida indicano di procedere con il trattamento chirurgico quando il diametro dell'aneurisma supera i 55 mm, mentre con diametri maggiori di 60 mm indicano un notevole aumento del rischio di dissezione e rottura. L'intervento chirurgico consiste nel sostituire il tratto di aorta aneurismatico con un graft artificiale. Molto spesso, quando l'aneurisma interessa anche la radice aortica, il paziente presenta una valvola rigurgitante. In questo caso anche la valvola viene sostituita durante l'impianto del graft. Se invece il soggetto presenta una normale valvola tricuspide, questa viene reimpiantata all'interno del graft. Questa tecnica prende il nome di *valve-sparing-root replacement* (VSRR). La mortalità associata a questo trattamento è piuttosto bassa e va dall'1% per i pazienti più giovani a più del 5% per quelli più anziani [6, 7]. Le proprietà meccaniche del graft sono molto diverse da quelle del vaso naturale: l'impianto di quest'ultimo può quindi influenzare notevolmente l'emodinamica del paziente.

Data la grande incidenza di questa patologia, questo lavoro di tesi si concentra sugli effetti emodinamici prodotti dal trattamento dell'aneurisma dell'aorta ascendente con la tecnica della VSRR. Particolare attenzione verrà posta

al tratto discendente del vaso, che a causa delle modifiche emodinamiche prodotte dal graft potrebbe sviluppare nuove patologie. A questo scopo è stata analizzata tramite modelli numerici la situazione pre e post-operatoria di cinque diversi soggetti, tutti affetti da aneurisma dell'aorta ascendente e trattati con la tecnica della VSRR.

Stato dell'arte

Nel presente studio, ogni paziente è stato studiato tramite un'analisi fluido-strutturale (FSI) sfruttando le potenzialità del software SimVascular. Ad oggi, sono pochi gli studi computazionali che si concentrano sull'analisi dei cambiamenti emodinamici conseguenti al trattamento di aneurismi dell'aorta ascendente tramite VSRR.

Nel 2011 Vardoulis *et al* [8] hanno sviluppato un modello fluido-strutturale 1D per studiare i cambiamenti emodinamici introdotti dall'impianto del graft. Le pareti del vaso sono state considerate come non-lineari e viscoelastiche, mentre la funzione del ventricolo sinistro è stata riprodotta adottando il modello descritto da Sagawa [9]. Le condizioni di uscita sono state imposte sfruttando un modello di Windkessel a tre elementi. Questo lavoro ha mostrato come l'impianto del graft in posizione prossimale produca un aumento sia nella pressione sistolica che nell'impedenza caratteristica prossimale.

De Nisco *et al* [10] nel 2020 hanno sviluppato un modello computazionale fluido-dinamico (CFD) per studiare le differenze emodinamiche tra un soggetto sano e uno affetto da aneurisma dell'aorta ascendente. La geometria paziente-specifica è stata ricostruita per entrambi i soggetti e le condizioni al contorno all'ingresso e nei tre tronchi sovraortici sono state imposte estraendo i dati da immagini 4D-Flow. I vasi a valle dell'aorta discendente sono invece stati considerati tramite un modello Windkessel a tre elementi ed è stata adottata la condizione di pareti rigide. I risultati hanno mostrato importanti

variazioni degli sforzi di taglio (WSS) nel caso patologico. Per verificare questi risultati sarebbe stato necessario tenere conto della deformabilità della parete e considerare un numero più elevato di soggetti.

Il presente lavoro di tesi si è sviluppato a partire da un lavoro precedentemente condotto dal nostro gruppo di ricerca [11]. In questo studio, sono stati analizzati i cambiamenti fluido-dinamici indotti dalla tecnica di VSRR tramite sia un modello FSI che uno CFD. La geometria del paziente analizzato è stata ricostruita a partire dalle immagini di risonanza magnetica (MRA) del soggetto. Per imporre la condizioni all'ingresso sono stati sfruttati i dati di velocità estratti dal 4D-Flow, mentre per le uscite è stato utilizzato un modello Windkessel a tre elementi. Come solutore è stato adottato ANSYS, accoppiando il solutore strutturale a quello fluido per l'analisi FSI. Confrontando i risultati dei due modelli, è emerso come solo l'analisi FSI sia in grado di fornire informazioni riguardo ai cambiamenti emodinamici prodotti dall'impianto del graft.

L'approccio del CMM-FSI

Il limite principale dello studio precedente condotto dal nostro gruppo di ricerca risiedeva nel numero limitato di soggetti analizzati (solo uno) a causa della tecnica di simulazione adottata. Questa infatti risultava essere estremamente costosa in termini computazionali. Per aumentare il numero di pazienti considerati, in questo studio è stato utilizzato un innovativo approccio per la soluzione di problemi fluido-strutturali: il Coupled Momentum Method for Fluid-Solid Interaction (CMM-FSI) [12]). Quest'ultimo parte dalla forma stabilizzata della classica equazione di Navier-Stokes applicata agli elementi finiti in un dominio rigido. Questa formulazione viene poi modificata per tenere conto dell'effetto della deformazione delle pareti sul dominio fluido, semplificando notevolmente la risoluzione di problemi FSI e permettendo

quindi di studiare un maggiore numero di pazienti. Questa formulazione prevede di sostituire la condizione di velocità nulla alla superficie del dominio fluido con una forza di trazione dipendente dalla massa e dalla rigidezza del vaso. La parete è modellata come una membrana sottile. Tra parete del vaso e superficie laterale del dominio fluido viene imposta una condizione di accoppiamento forte. La forma debole della formulazione del CMM-FSI è riportata nell'Equazione 2 [12].

$$
B_G(\vec{w}, q, \vec{v}, p) = \underbrace{\int_\Omega \{\vec{w} \cdot (\rho \vec{v}_{,t} + \rho \vec{v} \cdot \nabla \vec{v} - \vec{f}) + \nabla \vec{w} : (-pI + \tau) - \nabla q \cdot \vec{v}\} d\vec{x}}_{\text{Navier-Stokes equation}} +
$$

$$
+ \underbrace{\int_{\Gamma_h} \{-\vec{w} \cdot \vec{h} + q v_n\} ds}_{\text{Inlet BCs}} + \underbrace{\int_{\Gamma_g} q v_n ds}_{\text{Outlet BCs}} +
$$

$$
\underbrace{\zeta \int_{\Gamma_s} \{\vec{w} \cdot \rho^s \vec{v}_{,t} + \nabla \vec{w} : \sigma^s(\vec{u})\} ds - \zeta \int_{\partial \Gamma_h} \vec{w} \cdot \vec{h}^s dl + \int_{\Gamma_s} q v_n ds = 0}_{\text{Term accounting the wall deformation}}
$$

$$(1)$$

Materiali e Metodi

In questo studio sono stati analizzati cinque pazienti affetti da aneurisma dell'aorta ascendete. Tutti i soggetti presentavano una normale valvola tricuspide e sono quindi stati operati con la tecnica di VSRR, presso il New York-Presbyterian Hospital (New York, NY). Per ogni configurazione pre e post-operatoria di ogni paziente sono stati simulati cinque cicli cardiaci, di cui tre con pareti rigide (CFD) e due con pareti deformabili (FSI). Lo studio preliminare tramite CFD è richiesto dal solutore di SimVascular per imporre correttamente la condizione iniziale per la simulazione FSI. Il flusso di lavoro adottato per ogni caso studiato è riportato in Figura 1.

Ricostruzione del modello, co-registrazione e generazione della mesh
L'anatomia pre e post-operatoria di ogni paziente è stata ricostruita a partire
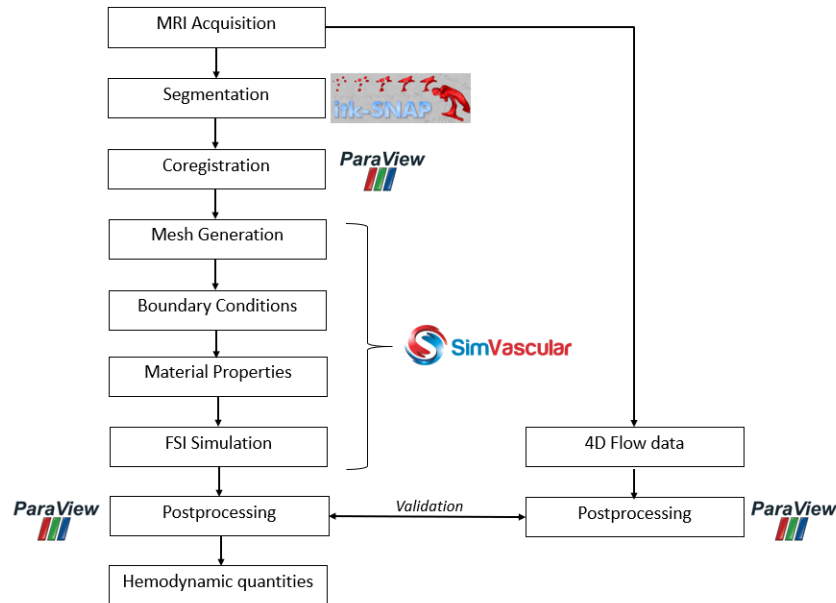
Figure 1: Workflow adottato per ogni paziente

dalle immagini MRA utilizzando il software ITK-SNAP 3.8 [13]. Il modello grezzo così ottenuto è stato poi esportato in Meshmixer (Autodesk Inc., San Rafael, CA, USA), dove è stato smussato e tagliato. I tre tronchi sovraortici sono stati tagliati alla base ed estrusi di 20 mm in direzione normale e il modello è stato tagliato a livello della giunzione sino-tubulare, isolando l'ingresso. La geometria così ottenuta è stata poi importata in Paraview, dove è stata eseguita l'operazione di co-registrazione sulle immagini di PC-MRA. Queste ultime sono state ottenute processando i dati 4D-Flow con un software sviluppato dal nostro gruppo di ricerca. Il risultato dell'operazione di co-registrazione può essere osservato in Figura 2. Le mesh dei modelli sono state generate in SimVascular con una dimensione caratteristica di 1mm, scelta grazie ad un'analisi di sensitività. Sono state così ottenute mesh di ~ 5 mln di elementi tetraedrici per tutte le configurazioni pre e post-operatorie.

Condizioni al contorno

Il modello della sezione d'ingresso è stato poi estratto dalla geometria co-registrata ed è stato utilizzato per estrarre i vettori velocità dai dati
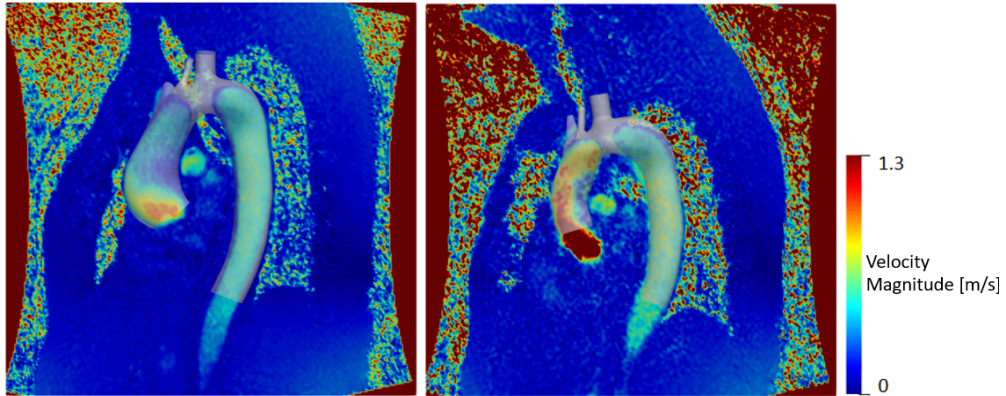
Figure 2: Risultato del processo di coregistrazione in un caso pre (a)
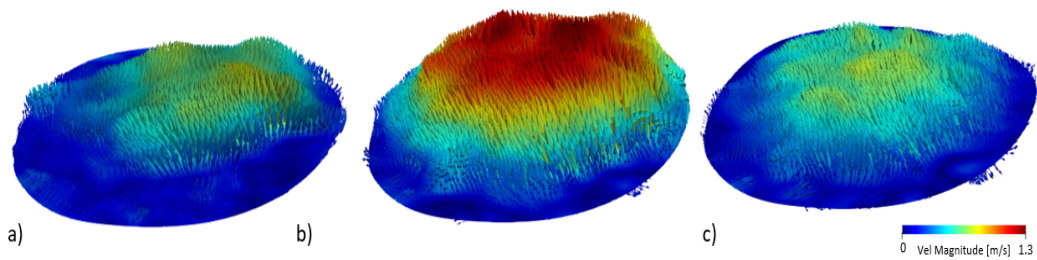e post (b) operatorio

Figure 3: Rappresentazione dei vettori velocità estratti dai dati 4D-Flow a
diversi istanti temporali del ciclo cardiaco: (a) inizio sistole b)picco sistolico
c)fine sistole)

4D-Flow, che sono poi stati utilizzati come condizioni d'ingresso della simulazione. I vettori estratti dai dati 4D-Flow sono mostrati in Figura 3. Per tenere conto dei vasi a valle dei tre tronchi sovraortici e dell'aorta discendente è stato adottato il modello di Windkessel a tre elementi, rappresentando questi vasi come una resistenza prossimale R_1, una compliance C e una resistenza distale R_2. Per il calcolo di questi valori sono state necessarie la pressione e la portata media attraverso l'uscita considerata. La portata in aorta discendente è stata calcolata come la media della portata estratta da cinque piani lungo la discendete. Per il calcolo della portata media attraverso i tronchi sovraortici, la differenza tra la portata in ingresso e quella in discendente è stata divisa tra
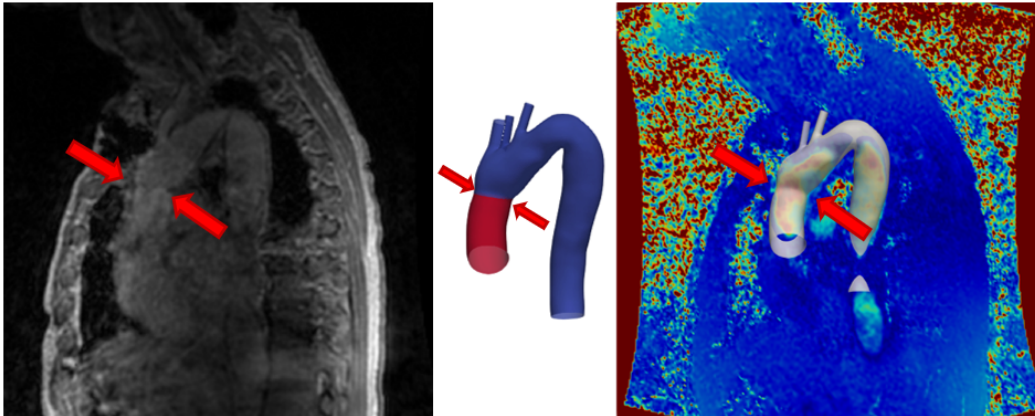
Figure 4: Da sinistra verso destra sono rappresentati il dato 4D-Flow, il modello e il dato PC-MRA di una configurazione post-operatoria. Le frecce indicano il sito di sutura del graft.

i tre vasi in base all'area della loro sezione di uscita.

Proprietà del materiale

SimVascular non permette di imporre proprietà meccaniche diverse in regioni differenti della stessa parete. Per tenere conto del graft è stato quindi necessario sviluppare un codice Python in grado di cambiare il *ModelFaceID* del modello. Questo rappresenta una proprietà del modello che viene creata automaticamente da SimVascular per differenziare gli ingressi, le uscite e la parete, consentendo di imporre le condizioni al contorno. Modificando il ModelFaceID nella regione desiderata, è stato quindi possibile assegnare proprietà diverse alla regione del modello destinata a rappresentare il graft. Questa zona è stata individuata in base alla posizione dell'impianto osservata dalle immagini di 4D-Flow, come rappresentato in Figura 4.

Riguardo alle proprietà meccaniche, per l'aorta è stato scelto uno spessore costante di 2mm [14, 15]. Il modulo di Young e la densità del vaso sono stati assegnati in base ai valori riportati da Khamdaeng *et al* [16] (rispettivamente 1.5MPa and 0.00112 g/mm^3). Infine per il graft sono stati adottati uno spessore di 0.305 mm e un modulo di Young di 11.84 MPa (Tasca *et al* [17]).

Parametri del solutore

Per tutte le simulazioni è stato adottato un *time step* di 1 ms, mentre la soluzione è stata salvata ogni 10 ms. Sono stati utilizzati due diversi solutori di SimVascular : NL solver per la CFD e GMRES per l'analisi FSI. Per ogni *time step*, SimVascular esegue un loop di iterazioni non lineari per ottenere all'istante corrente la soluzione del sistema non lineare che descrive il problema, utilizzando la strategia di Newton-Rapson. Il *residual criteria* e le *tollerenze* si riferiscono rispettivamente alla soluzione del sistema non lineare e quella del sistema linearizzato. Questi due parametri sono stati impostati rispettivamente a 0.001 e 0.0001. La *step construction* regola il numero massimo di iterazioni per ogni *time step*. Valori di 7 e 10 sono stati scelti rispettivamente per la simulazione con pareti rigide e con pareti deformabili.

Post-processing

Il post-processing dei risultati può essere diviso in due fasi: il confronto tra FSI e 4D-flow e il confronto tra la situazione pre e post-operatoria.

Confronto tra FSI e 4D-Flow. Per ogni paziente sono stati estratti quattro piani, uno lungo l'aorta ascendente e tre lungo quella discendente. Per ognuno di questi l'errore quadratico medio (RMSE) e l'errore quadratico medio relativo (RRMSE) sono stati calcolati per misurare la differenza tra le velocità ottenute dalla simulazione e quelle estratte dal 4D-Flow. Infine sono state confrontate le streamlines e le mappe di velocità ottenute attraverso le due metodologie.

Confronto tra situazione pre e post-operatoria. Per studiare i cambiamenti emodinamici in aorta discendente indotti dall'impianto del graft, sono stati calcolati i WSS e l'OSI (oscillatory shear index). Molti studi hanno dimostrato come un'alterazione in queste due quantità possa innescare il processo di aterogenesi. Infatti, quando le cellule endoteliali sono sottoposte a stimoli meccanici intensi, possono dare inizio sia al processo aterogenico che a quello
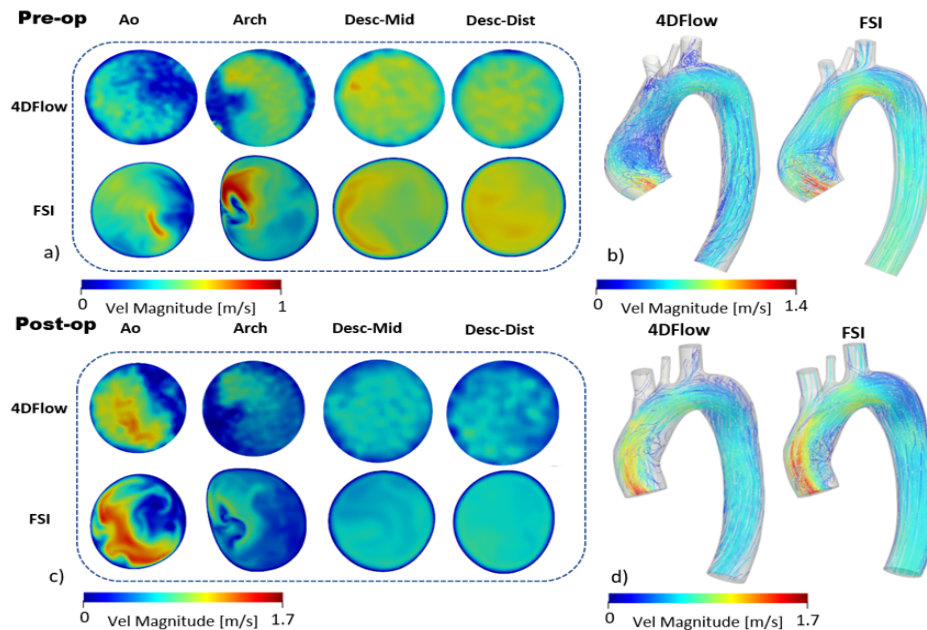
Figure 5: Confronto tra streamlines e mappe di colore ottenute dai dati 4D-Flow e dall'analisi FSI

di formazione di aneurismi. [18]. In particolare, valori di OSI vicino a 0.5 e WSS fuori dal range fisiologico sono da considerare come fattori di rischio [18–20].

Per le quantità biomeccaniche, sono state calcolate le deformazioni. Dato che SimVascular non fornisce questa grandezza tra le variabili di uscita, è stato sviluppato un codice Matlab in grado di calcolare le deformazioni a partire dagli spostamenti. A questo scopo è stata adottata la formulazione del tensore della deformazione di Green.

Risultati

Confronto tra 4D-Flow e FSI

Un buon confronto è emerso tra le streamlines e le mappe di colore (Figura 5) ottenute dai dati 4D-Flow e dai risultati dell'analisi FSI: sia i picchi di velocità che i vortici sono stati correttamente stimati dal modello numerico,

dimostrandone la capacità di riprodurre correttamente i pattern emodinamici.
É emersa una buona capacità dell'analisi FSI di riprodurre l'emodinamica del paziente anche dal confronto quantitativo delle due metodologie . Dal calcolo del RRMSE è stato infatti trovato un valore medio di 0.244 ± 0.059, confrontabile con i valori trovati in letteratura [21]. In generale è stata osservata una sovrastima della velocità lungo l'aorta ascendente, che ha portato ad ottenere un valore medio del RRMSE pari a 0.322 ± 0.043 in questa regione. Il miglior accordo tra le due metodologie è stato ritrovato lungo un piano posizionato a metà dell'aorta discendente, mostrando un RRMSE medio di 0.194 ± 0.031. In generale, i valori migliori di RRMSE sono stati osservati nel modello post-operatorio (0.274 ± 0.029 per il pre-operatorio e 0.213 ± 0.011 per il post-operatorio)

Confronto tra situazione pre e post-operatoria

I cambiamenti indotti dal graft sull'emodinamica post operatoria dell'aorta discendente sono stati analizzati tramite un *t-test*. In particolare, sono
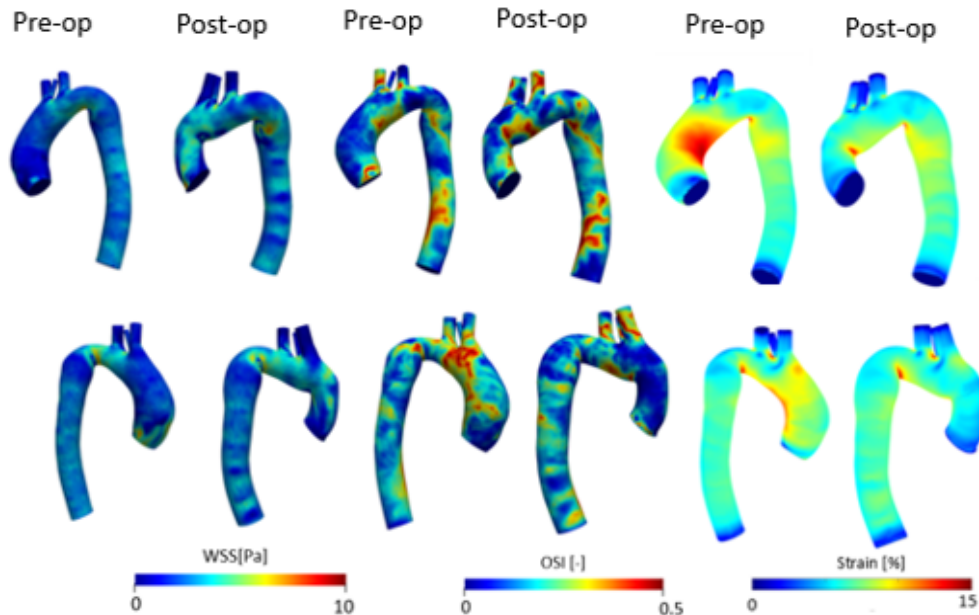

Figure 6: Distribuzione di WSS(a sinistra) , OSI (al centro) e deformazioni(a destra)

state confrontate le popolazioni di percentili di OSI, WSS e deformazioni tra configurazione pre e post-operatoria. I risultati di questo studio sono riportati in Figura 7.

Per quanto riguarda gli OSI, è stata riportata una differenza statistica solo nel caso del primo paziente. Dal confronto del 90° percentile (Tabelle C.1-C.2) è emerso un significativo incremento rispetto al caso pre-operatorio. Questa analisi ha quindi dimostrato come l'impianto del graft produca un incremento nel valore dell'OSI post-operatorio. L'unica eccezione a questo comportamento è stata mostrata nel Paziente 2, che non ha evidenziato nessun cambiamento tra il valore degli OSI pre e post-operatori. Questo comportamento può essere causato dalla riduzione della sezione dell'aorta all'istmo.

I WSS sono stati studiati al picco sistolico. In questo caso non è stato osservato nessun trend comune: i Pazienti 1 e 2 hanno mostrato un aumento di questa grandezza, i Pazienti 3 e 5 una riduzione, mentre il Paziente 4 non ha dimostrato nessuna differenza significativa. Questo comportamento può essere spiegato osservando le variazioni di velocità tra la situazione pre e quella post-operatoria: nei Pazienti 1 e 2 si è osservata una più alta velocità post-intervento, il Paziente 4 ha riportato un piccolo incremento, mentre nei Pazienti 3 e 5 è stata riportata una riduzione della velocità, probabilmente dovuta a una minore portata in ingresso. Il graft presenta una rigidezza maggiore rispetto alla parete dell'aorta e questo produce una dissipazione di energia minore rispetto a quella del vaso naturale, producendo un aumento di velocità nella configurazione post-operatoria, come riportato anche da studi precedenti [22]. In più l'impianto del graft riduce la sezione di ingresso del vaso, inducendo ulteriori aumenti di velocità. La conseguenza di questo aumento di velocità è un aumento dell'intensità dei WSS.

Analizzando invece il comportamento delle deformazioni al picco sistolico, per i Pazienti 1,2 e 4 non sono state riportate differenze tra la situazione
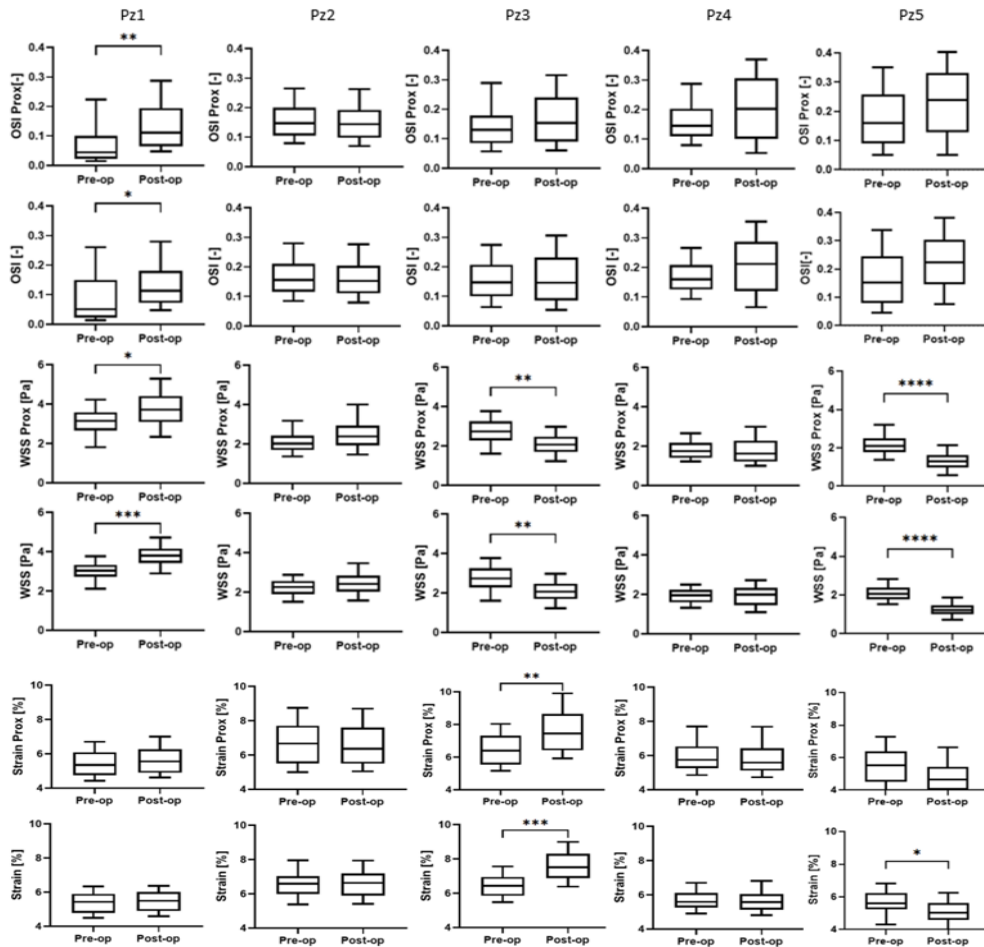
Figure 7: Boxplot ottenuti dal confronto della popolazione di percentili di WSS e deformazioni al picco sistolico e di OSI calcolati nella configurazione pre e post-operatoria. *=p<0.05, **=p<0.01,***=p<0.001,****=p<0.0001

pre e post-operatoria. Una variazione statistica è stata invece riportata nel caso dei Pazienti 3 e 5: il primo ha mostrato un importante aumento delle deformazioni, mentre il secondo una riduzione. Questo comportamento può essere spiegato dalle differenze di pressione osservate nei due casi: la pressione post operatoria è risultata maggiore per il terzo paziente e minore per il secondo. In conclusione, non è stata quindi trovata una relazione significativa tra la variazione delle deformazioni e l'impianto del graft. Un significativo aumento delle deformazioni è stato però osservato per tutti i pazienti lungo il

sito di sutura.

Considerazioni finali e conclusioni

Dal confronto delle velocità ottenute tramite l'analisi FSI sviluppata in questo lavoro e i dati 4D-Flow è emersa la buona capacità del modello numerico di riprodurre l'emodinamica dei pazienti.

Lo studio delle grandezze emodinamiche ha dimostrato una relazione tra l'impianto del graft e l'incremento di OSI e WSS lungo l'aorta discendente nel caso post-operatorio. Poiché diversi studi precedenti segnalano come un incremento di queste quantità possa essere indice di una stimolazione delle cellule endoteliali che può portare all'innesco del processo di aterogenesi [18–20], il tratto dell'aorta discendente deve essere considerato come una regione a rischio.

Un altro fattore di rischio osservato, riguarda il sito di sutura dell'aorta ascendente post-operatoria, in cui è stato riportato un aumento delle deformazioni.

Il modello FSI sviluppato in questo lavoro di tesi costituisce una metodologia innovativa per studiare i cambiamenti emodinamici indotti dal trattamento dell'aneurisma dell'aorta ascendente tramite VSRR. Le semplificazioni introdotte dalla formulazione del CMM-FSI per la soluzione di problemi fluido-strutturali, hanno permesso di riprodurre l'analisi su un numero elevato di pazienti. Grazie alla varietà di casi analizzati è stato quindi possibile ottenere una visione piuttosto ampia sugli effetti prodotti dal trattamento dell'aneurisma dell'aorta ascendente tramite graft, evidenziando tratti comuni e differenze tra i vari soggetti considerati.

Possibili sviluppi futuri includono l'ulteriore aumento della popolazione analizzata. Questo permetterebbe di verificare i risultati ottenuti in questo studio e di valutare se la forma dell'arco aortico può influenzare o meno i

cambiamenti emodinamici prodotti dal graft. Un altro aspetto interessante da analizzare potrebbe essere lo studio dell'effetto sull'emodinamica di diverse proprietà meccaniche del graft (e.g., la rigidezza, la lunghezza, lo spessore, etc.).

Abstract

Introduction

Aortic aneurysm incidence ranges from 5 to 10 per 100 000 person-years [1–3], representing the nineteenth leading cause of death overall [4, 5]. Almost 60% of all thoracic aneurysms (TAA) are constituted by ascending aortic aneurysms (ATAA) [23]. The guidelines [24] suggest to proceed with the surgical treatment when the diameter is ≥ 55 mm. With diameters $> 60\ mm$, the risk of dissection or rupture sharply increases [25]. The surgical treatment involves the substitution of the aneurysmatic portion of the aorta with a tube graft. If the aneurysm involves also the aortic root and if regurgitation is present, valve substitution is required too, otherwise the aortic valve-sparing technique is performed (VSRR), re-implanting patient's natural valve in the tube graft. The surgical mortality associated with aortic replacement goes from 1% for younger patients to $> 5\%$ for older ones [6, 7]. The graft shows different mechanical properties with respect to the vessel wall and may induce important hemodynamic variations. Given the important incidence of this pathology, the current work will focus its attention on the hemodynamic changes induced by surgical graft replacement of ascending aneurysmatic aorta, with particular focus on descending tract, which may develop further pathologies as a consequence of the surgical treatment. To this purpose, pre and post-operative configuration of five different patients treated with the VSRR technique will be analyzed through numerical models.

Numerical studies from literature

In this study, a Fluid-Solid Interaction (FSI) analysis was performed exploiting SimVascular software. To the best of the author's knowledge, there is a lack of computational studies comparing the pre and post-operative hemodynamics of patients who underwent VSRR treatment.

In 2011 Vardoulis *et al* [8] developed a 1D FSI cardiovascular tree model to assess hemodynamic modifications induced by a proximal and a distal graft. The wall mechanical behavior was considered to be nonlinear and viscoelastic. The function of the left ventricle was simulated adopting the varying elastance model described by Sagawa [9] and the distal vessels terminated with a three-element Winkessel model. As consequence of graft implant in the proximal region, this simplified model showed an increment in both the systolic arterial pressure and in the proximal aortic characteristic impedance.

In 2020, De Nisco *et al* [10] used SimVascular to perform a computational fluid dynamic (CFD) analysis to assess hemodynamic changes between one healthy subject and one patient affected by ATAA. Patient specific geometry was reconstructed and to impose the boundary conditions at the inlet and at the supra-aortic branches, 4D-Flow data were exploited, while at the descending aorta three-element Windkessel model was adopted. Rigid wall condition was assumed. The results reported localized marked wall shear stress (WSS) contraction regions in the pathological case. To verify these outcomes, deformable wall and a larger pool of patients would be needed.

This master thesis project takes its origin from a previous pilot work [11] developed by our research group. In this study both a CFD and an FSI analysis were performed to investigate fluid dynamic changes in patients treated with the VSRR procedure. The geometry was reconstructed starting from patient's MRA images. At the inlet, patient-specific velocities extracted from 4D-Flow data were used, while three-element Windkessel model was adopted at the

outlets. The analysis was run in ANSYS, coupling the structural solver and fluid solver for the FSI analysis. The comparison between FSI and CFD analysis demonstrated that hemodynamic changes can only be assessed through an FSI study.

The CMM-FSI Formulation

The main limitation of the previous study of our group was the small population analyzed (only one subject), due to the very consuming simulation technique adopted. To enlarge patient population, a new formulation for the FSI problem was adopted in the current study: the Coupled Momentum Method for Fluid-Solid Interaction (CMM-FSI) [12]. This formulation starts from a conventional stabilized finite element formulation for the Navier-Stokes equation in a rigid domain and modifies it in order to account for the effect of wall deformation on the fluid domain. This simplifies considerably the solution of the FSI problem, allowing to study a higher number of patients. In this formulation, the zero velocity condition on the lateral surface of the fluid domain is removed and replaced with a traction condition, linked to the mass and stiffness of the vessel wall. A strong coupling is assumed so the vessel wall and the boundary of the fluid domain have the same degrees of freedom. In equation 2 the weak form of the CMM-FSI formulation is reported [12].

$$
B_G(\vec{w}, q, \vec{v}, p) = \underbrace{\int_\Omega \{\vec{w} \cdot (\rho \vec{v}_{,t} + \rho \vec{v} \cdot \nabla \vec{v} - \vec{f}) + \nabla \vec{w} : (-pI + \tau) - \nabla q \cdot \vec{v}\} d\vec{x}}_{\text{Navier-Stokes equation}} +
$$

$$
+ \underbrace{\int_{\Gamma_h} \{-\vec{w} \cdot \vec{h} + q v_n\} ds}_{\text{Inlet BCs}} + \underbrace{\int_{\Gamma_g} q v_n ds}_{\text{Outlet BCs}} +
$$

$$
\underbrace{\zeta \int_{\Gamma_s} \{\vec{w} \cdot \rho^s \vec{v}_{,t} + \nabla \vec{w} : \sigma^s(\vec{u})\} ds - \zeta \int_{\partial \Gamma_h} \vec{w} \cdot \vec{h}^s dl + \int_{\Gamma_s} q v_n ds = 0}_{\text{Term accounting the wall deformation}}
$$

$$
(2)
$$

Materials and Methods

In this study five patients with a normal tricuspid valve affected by ascending aortic aneurysm and treated with the valve sparing technique were analyzed. All the patients were treated at New York-Presbyterian Hospital (New York, NY). For each patient, both the pre and the post-intervention configurations were simulated, performing five cardiac cycles for each subject, three with the rigid wall condition (CFD) and two with the deformable wall condition (FSI). The preliminary CFD simulation was required by SimVascular software to correctly set the initial condition of the deformable wall simulation. For each configuration, the workflow showed in Figure 8 was exploited.
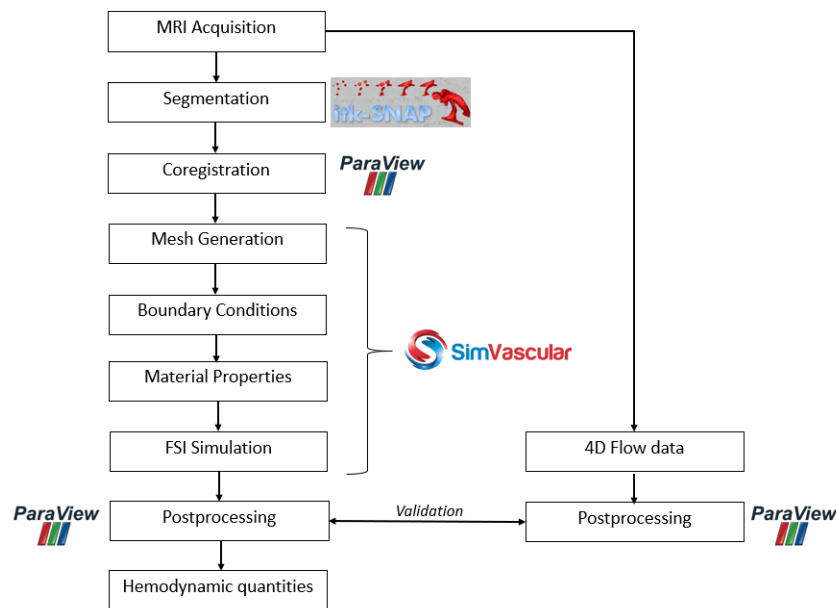

Figure 8: Workflow followed for each patient

Model reconstruction, co-registration and meshing

The pre and post-intervention anatomy of each patient were reconstructed using the software ITK-SNAP 3.8 [13], starting from MRA images. The rough model obtained was then saved as an STL file and exported in Meshmixer (Autodesk Inc., San Rafael, CA, USA), where it was smoothed and remeshed.
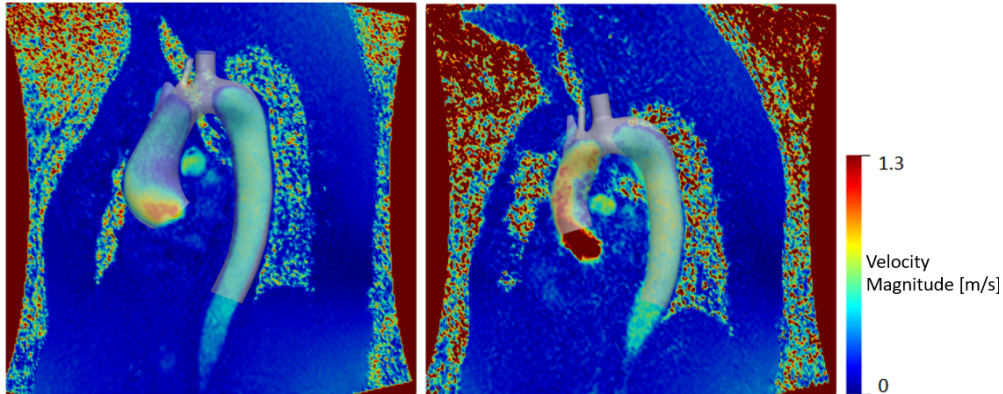
Figure 9: Pre (left) and post-operative (right) geometry co-registration on PC-MRA data

The three supra-aortic vessels were cut at the basis and extruded by 20 mm in the normal direction and the model was cut at the level of the sinotubular junction (STJ), isolating the inlet. The model was imported as an STL file in Paraview, where it was co-registered on patient's PC-MRA images. These images were obtained through the post-processing of 4D-Flow data, performed with an in-house Python code. The results of the co-registration process are shown in Figure 9. After a mesh sensitivity analysis, a characteristic dimension of 1mm was chosen for all the models. The meshes were generated using SimVascular and $\sim$ 5 mln elements tetrahedral meshes were obtained for all the patients.

Boundary conditions setting

Once the model was correctly co-registered, the inlet was extracted and used to obtain patient's velocity vectors from 4D-Flow data. These vectors were then used to impose patient-specific inlet boundary conditions. In Figure 10 the velocity vectors extracted from 4D-Flow data are reported. At the outlets, a three-element Windkessel model was adopted, which represents the downstream vessels as a proximal resistance R_1, a compliance C and a distal resistance R_2. RCR values computation required the mean pressure and flow
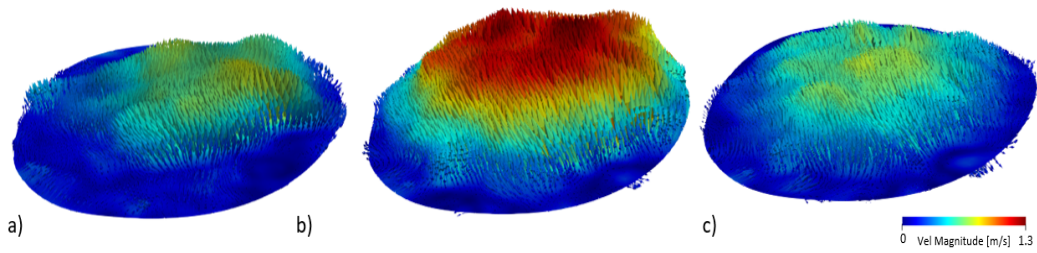
Figure 10: Representation of inlet velocity vectors extracted from 4D-Flow data at different cardiac cycle phases (a)early systole b)systolic peak c)late systole)
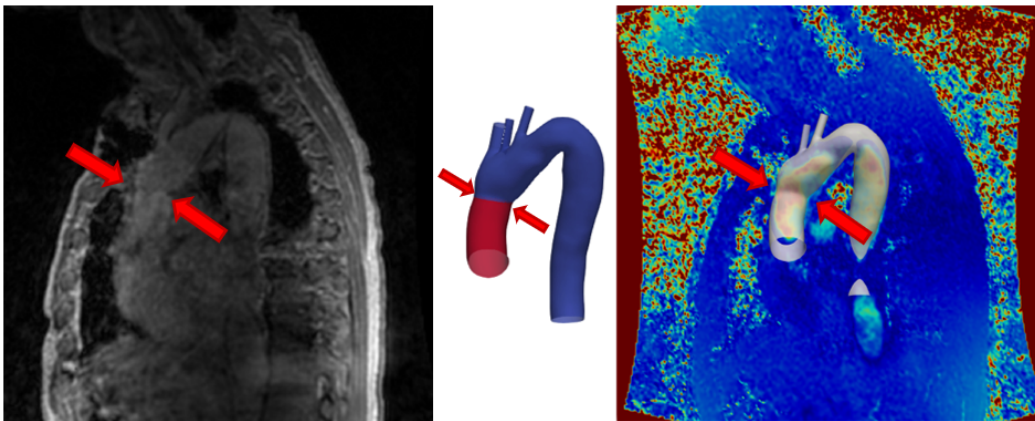

Figure 11: Location of the graft in the post-surgical situation

rate through each section [26]. Q_{DescAo} was calculated as the mean flow rate through five different descending aorta sections, while the flow rate through the aortic branches was calculated as the partition of $Q_{in} - Q_{DescAo}$ based on the area of each supra-aortic outlet section.

Material properties

SimVascular software did not allow to set different material properties to the wall domain. To account for the graft, a Python code was developed. This code allowed to change ModelFaceID property, which is a property automatically set by SimVascular solver to differentiate the various portions of the model, based on the angle between the surfaces. The region substituted by the graft was identified locating graft position on 4D-Flow images (Figure 11).

A constant thickness of 2 mm was set for the aortic wall [14, 15]. For the Young Modulus and density setting, the values reported by Khamdaeng *et al* [16] were adopted and set to respectively 1.5MPa and 0.00112 g/mm^3. For the graft properties, a thickness of 0.305 mm and a Young Modulus of 11.84MPa were imposed (Tasca *et al* [17]).

Solver Parameters

A time step of 1 ms was chosen for all the simulations and the results were saved every 10 ms. For the CFD simulation SimVascular's NL solver was adopted, while for the FSI analysis GMRES solver was used. For each time step, SimVascular solver performs a nonlinear iteration loop to obtain the solution at the current time to the non-linear system defining the problem, using a Newton Rapson strategy which linearizes the problem. The *residual criteria* and the *tolerances* are referred to the solution of respectively the non-linear and linearized system and were set respectively to 0.001 and 0.0001. The *step construction* imposes the maximum number of iterations performed for each time step. A value of 7 and 10 was chosen respectively for the rigid and the deformable wall simulation.

Post-processing

The post-processing was focused on two principal aspects: the comparison between 4D-Flow and FSI analysis velocities and the comparison between pre and post-surgical configuration.

Comparison between FSI and 4D-Flow. For each patient, four planes (one in the ascending aorta and three along the descending tract of the vessel) were considered. For each plane the RMSE and the RRMSE were computed to measure the difference between the velocities estimated by the simulation and the velocities extracted from the 4D-Flow. Moreover, streamlines and colormaps obtained with the two methodologies were compared.

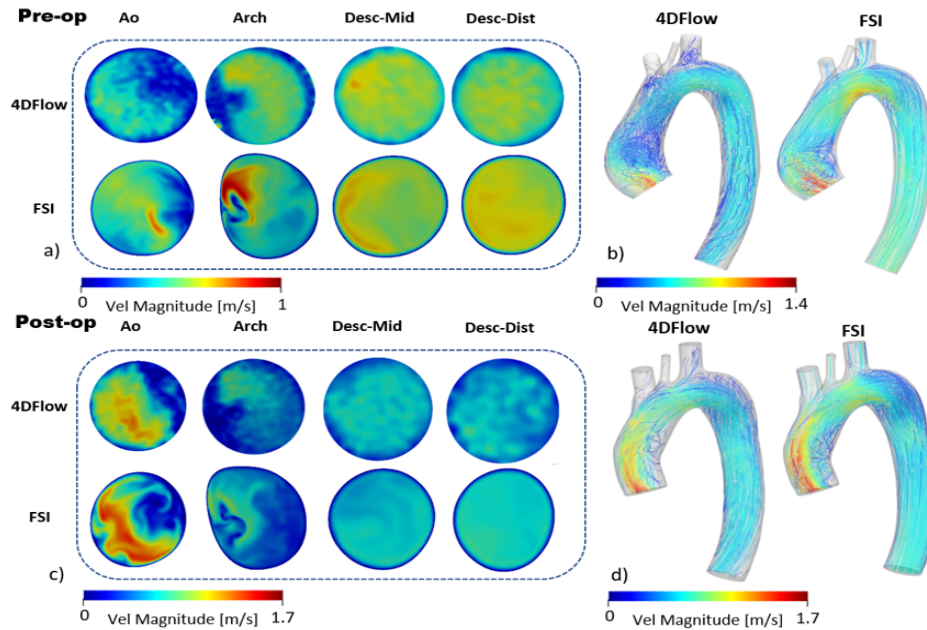*Pre vs post-surgical configuration.* To assess graft effects on descending

Figure 12: Streamlines and colormaps comparison between 4D-Flow data and FSI analysis

aorta hemodynamic, WSS and oscillatory shear index (OSI) between the pre and post-operative configuration were compared. Diverse studies report that alteration in WSS and OSI, inducing an intense mechanical stimulus on endothelial cells, may trigger atherogenic process and even aneurysms formation [18]. Clinical studies report that OSI values close to 0.5 and WSS outside the physiological range should be considered risky. [18–20]. Concerning the biomechanical quantities, the strain were analyzed. Since strains were not provided by SimVascular solver, an in-house Matlab code was developed to compute Green strain tensor, starting from the displacement obtained from simulation results.

Results

Comparison between FSI and 4D-Flow.

Comparing both the streamlines and the colormap along different aortic

sections (Figure 12), a good agreement was found between simulation results and 4D-Flow data. Both velocity distribution and vortical flow patterns were correctly estimated by the numerical model, assessing its capability to reproduce hemodynamic patterns. Concerning the quantitative comparison, the estimated mean RRMSE was 0.244 ± 0.059, comparable with values found in literature [21]. A velocity overestimation was observed along the ascending aorta, where higher RRMSE were observed (0.322 ± 0.043), while the best agreement was found in a section extracted in the middle-descending aorta (mean RRMSE= 0.194 ± 0.031). In the post-surgical configuration a better RRMSE was observed. (0.274 ± 0.029vs 0.213 ± 0.011 pre vs post-surgical RRMSE).

Pre-surgical vs post-surgical configuration

To assess the hemodynamic changes induced by the graft on the descending tract of the aorta, a *t-test* was performed on percentile population of OSI and systolic peak WSS and strain. The results of this analysis are reported in
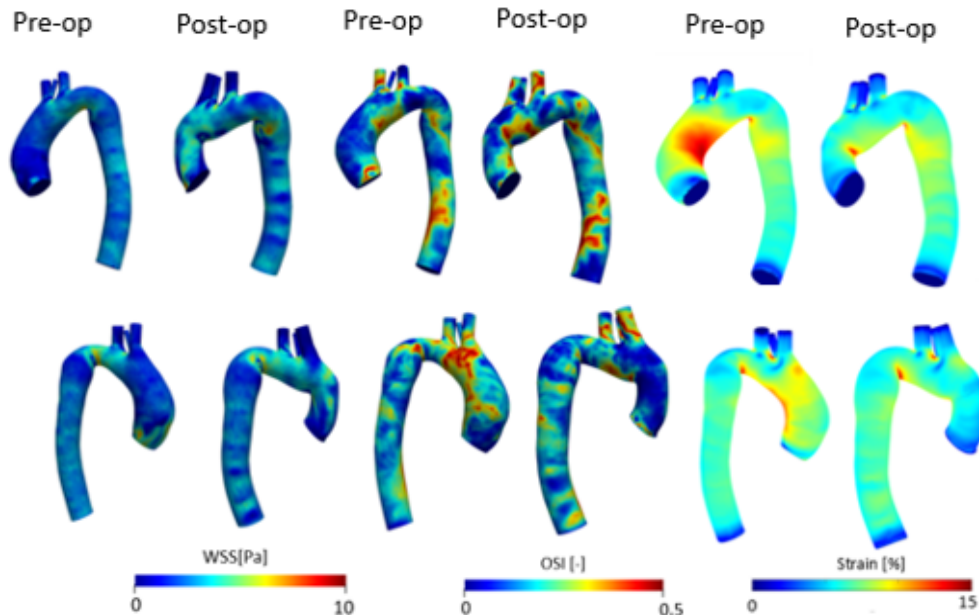

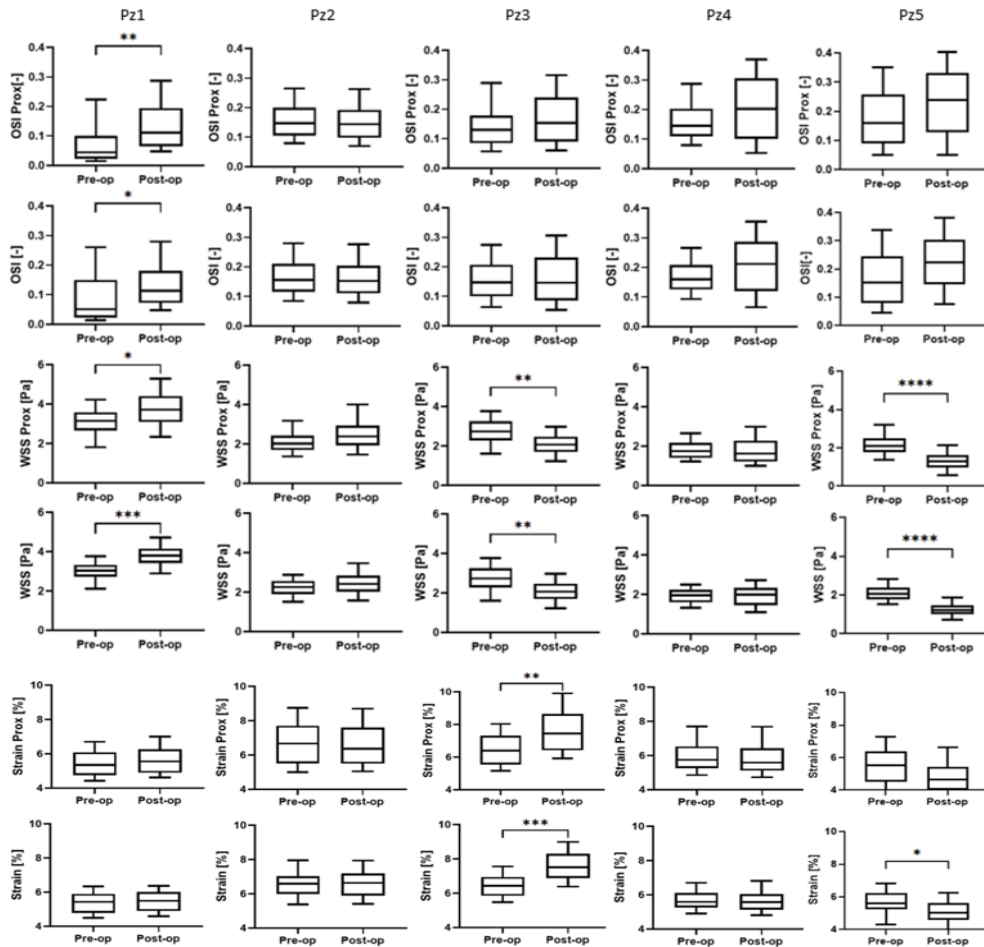Figure 13: WSS, OSI and Strain distribution

Figure 14: Comparison between percentiles population of WSS and strains at systolic peak and of OSI between pre and post-surgical configurations
*=p<0.05, **=p<0.01,***=p<0.001,****=p<0.0001

Figure 14, while in Figure 13 the distribution of the three quantities for one Patient are reported.

Focusing on OSI distribution, a statistical difference was detected only for Patient 1, but a general increment of post operative OSI was found for all the patient, as it can be assessed observing the value of the 90th percentile (Tables C.1-C.2). This general behavior may assess a relationship between graft implant and higher post-operative OSI values. The only exception to this trend was Patient 2, for whom no statistical difference was observed between

pre and post-surgical OSI percentile distribution, due maybe to the aortic section restriction at the isthmus.

No common trends were reported for post-operative WSS: an increment was observed for Patients 1, 2, a decrease was reported for Patients 3 and 5 and no difference was displayed by Patient 4. This behavior was explained by velocity variations between pre and post-operative situation: a higher post-operative velocity was observed for Patients 1 and 2, a small increment for Patient 4, while a velocity reduction was detected for Patients 3 and 5, probably due to the lower inlet flow rate. The graft has a higher stiffness with respect to the vessel wall, inducing lower energy loss than the natural vessel, and for this reason it usually induces a velocity increment in the post-operative situation, as reported also by previous studies [22]. Moreover, with the graft implant, the inlet section is reduced inducing further velocity enhancement. This velocity increment induced by the graft produces a WSS increase as a consequence.

Analyzing the strains behavior, no difference between the pre and post surgical configuration was observed in Patients 1, 2 and 4. A statistically relevant strain increase and decrease was observed for respectively Patient 3 and 5. This behavior was explained by the pressure differences between the pre and post-surgical configurations: while Patient 3 showed a pressure increment in the post-operative case, Patient 5 showed a decrease. Given these behaviors, no relationship was found between graft implant and strain variations between pre and post-surgical situations. Regarding the post-operative ascending aorta, a strain intensification was observed at the suture site in all the patients.

Final Considerations and conclusions

The comparison between 4D-Flow and numerical results, showed a good agreement between the two datasets, assessing a good capability of FSI analysis to reproduce patient specific fluid-dynamic.

The comparison of hemodynamic quantities between pre and post-surgical configurations showed a general increment of OSI and WSS in the post-operative configuration, suggesting fluid-dynamic disturbances induced by the graft. An increment in these two quantities constitutes a risk factor for atherogenic process triggering, indicating the post surgical descending aorta as a risky region.

Finally, another risk factor connected to VSRR technique is the strain intensification at the suture site, suggesting that also this region should be carefully checked.

In this study, an innovative FSI methodology to evaluate the hemodynamic changes induced by VSRR technique was developed. The adopted CMM-FSI formulation, which simplifies the process of FSI setting, permitted to investigate a numerous population. This allowed to observe general trends and thus to provide a deeper insight in post-operative hemodynamic modifications. Future development of this study may further enlarge the pool of patient to verify the outcome of this work and to evaluate whether aortic arch shape influences the graft effects on patient's hemodynamic. Another interesting development would be the assessment of the disturbances induced by different graft properties (e.g. stiffness, length, thickness, etc.).

Chapter 1

Introduction

In this chapter a general introduction to anatomy, physiology and pathology of the aorta is reported, beside the most common treatments adopted today. This study is focused on patients affected by ascending aortic aneurysm, but a general overview of the most common pathologies of the aorta is privided. The second part of the chapter is dedicated to the imaging techniques used today as diagnostic tools and exploited in this work as source of data.

1.1   The Cardiovascular System

The cardiovascular system has the basic role to transport oxygen and nutrients to the different districts of the body, while removing the catabolites and carbon dioxide produced by the cells. The associated diseases are various and can affect both the heart and the vessels. Indeed, as reported by the Task Force of the European Society of Cardiology [27], those pathologies are among the leading cause of death in the developed countries and, especially aortic diseases, contribute to the high overall cardiovascular mortality.

1.1.1   Anatomy

Aorta is the largest artery in the body. The roles of this vessel are mainly three: regulation, capacitance and pumping function. It regulates both systemic vascular resistance and heart rate thanks to the pressure-responsive receptors located in the ascending tract and in the aortic arch segments (*regulatory function*), it stores the blood during the systolic phase and releases it during the diastole (*capacitance function*) and it propagates the pulse wave generated by the blood pulsatile flow (*pumping function*).
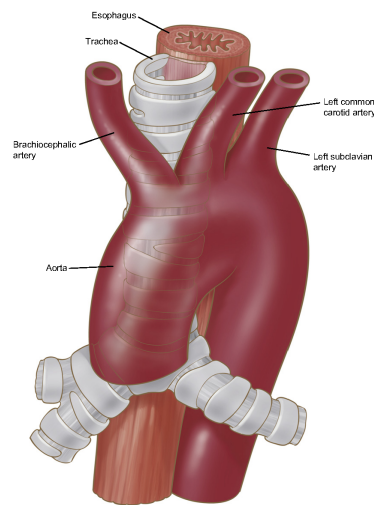
Figure 1.1: Aortic arch and great vessels [28]

The aorta arises from the aortic orifice located in the upper part of the left ventricle and extends down to the abdomen, ending at the level of the fourth lumbar vertebra, where it splits into the left and right common iliac arteries. It is composed of four sections - the ascending aorta, the aortic arch, the descending aorta and the abdominal aorta [29].

The ascending aorta begins at the sinotubular junction and consists of the aortic root and a tubular segment. At the origin of the ascending aorta, the sinuses of Valsalva are present, which give rise to the coronary arteries. The second section is constituted by the aortic arch. From this segment, three major branches take origin: the brachiocephalic trunk, the left common carotid artery and the left subclavian artery. This configuration is present in 75% of individuals, but several congenital variations exist. 20% of individuals presents bovine arch anatomy, indicated by common origin of the brachiocephalic and left common carotid arteries. Other variants include either the left vertebral artery or the right subclavian artery branched directly from the aorta [30]. The descending aorta begins at the lower border of the fourth thoracic vertebra and ends at the level of the 12$^{\text{th}}$ thoracic vertebra.

1.1.2 Histology

The aortic wall consists of three layers: the outer fibrous tunica adventitia, the thickest muscoloelastic tunica media and the thin inner intima.

The adventitia is a thin collagenous layer that contains the vasa vasorum (which vascularize the vessel wall) and the nerves. It is composed of collagen fibers, some elastic fibers, fibroblasts and mast cells. The rich collagen content gives this layer a tensile strength greater than the one of the other two components. The aortic media accounts for up to 80% of the aortic wall thickness and it is composed of elastic tissue intertwined with muscle fibers. The inner layer is the aortic intima, made by a basement membrane lined with
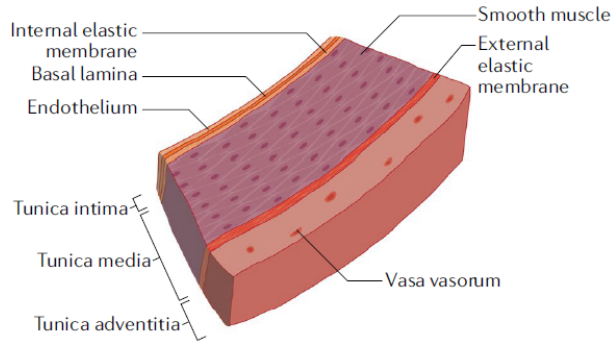
Figure 1.2: Representation of the three aortic layers [31]

endothelium, that is in direct contact with blood.

1.1.3 Pathologies and pathophysiology

In the last two decades, the global death rate from aortic diseases has increased from 2.49 to 2.78 per 100 000 person-years. The pathologies that affect the aorta can be both acute and chronic, congenital or acquired and can involve both the thoracic and the abdominal tract. The most common pathology involving the aorta is atherosclerosis [25]. Other diseases implying this vessel can be generally classified in aortic aneurysm and acute aortic syndromes [31], each comprising further pathologies, as shown in Figure 1.3.
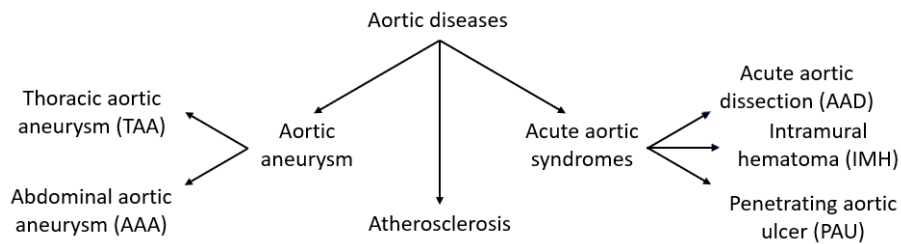

Figure 1.3: Classification of pathologies involving the aorta

This thesis gathers its attention on ascending aortic aneurysm treated with PET graft substitution and on the effect of this implant on blood fluid dynamic in the descending tract of this vessel. For this reason, an insight into aortic aneurysm etiology, risks factors and treatment is given, with a particular

focus on ascending aortic aneurysm. Since one of the main risks of an aortic aneurysm is dissection, a deeper insight in this pathology is given too.

Aortic aneurysm

Aortic aneurysm incidence ranges from 5 to 10 per 100 000 person-years, a trend that is increasing probably due to the population aging and to the improvement of diagnostic techniques that allows detecting a higher number of cases [1–3]. It represents also the nineteenth leading cause of death overall [4, 5].
An aneurysm is the dilatation of a blood vessel to more than 150% of its initial diameter, which can grow in size and eventually rupture, leading to severe complications and death. The aneurysm involves all the three layers of the aorta, while what is called *a false aneurysm* creates a periaortic hematoma between the media and adventitia tunica. There are two main types of aortic aneurysm, thoracic and abdominal. The first can be located both in the ascending and descending tract of the vessel. TAAs have a long-term, silent growing phase, with a growing rate of ~ 1.2 mm per year [31]. The diagnosis is usually made accidentally during medical investigations performed for other indications. The signs and symptoms can vary based on the involvement of adjacent organs and range from hoarseness, stridor, shortness of breath, dysphagia plethora and edema. Hypotension and shock are usually signs of hemorrhage into the pleural and/or pericardial space [31]. The most common imaging techniques used to assess the aneurysms are transthoracic echocardiography, computed tomography (CT) and magnetic resonance (MRI). The first one is useful especially for screening and monitoring, since it is a cheap, easy-to-use and minimally invasive technique, but, in most cases, only the aortic root and the ascending aorta can be assessed [32]. For this reason, when a dilated aorta is shown, further

investigations should be carried out using CT or MRI. CT offers different reconstructions options, but the cumulative radiation dose must be taken into account in younger patients. MRI, with its lack of ionizing radiation, is the technique of choice for all the patients, with the exception of subjects with ferromagnetic and/or magnetically activated devices or claustrophobia.

Ascending aortic aneurysm. About 60% of TAAs involves the aortic root or the ascending tract of the aorta [23].

Risk Factors. Among the leading causes of aortic aneurysm, atherosclerosis is the most common. The development of the pathology is related to hypertension, cigarette smoking, advanced age and chronic obstructive pulmonary disease.

Frequent causes are also connective tissue disorders, such as Marfan syndrome and Loeys-Dietz syndrome. The first one is caused by a mutation of the fibrillin-1 gene. The prevalence of this syndrome is 1:3000 [33] and almost the whole group develop an aortic disease (aortic aneurysm, dissection, rupture). This brings to a sharp reduction of the life expectancy (60 years with proper treatments, 32 years without treatments [24]). The aneurysm usually develops in the aortic root area (Figure 1.4). If the sinotubular junction is involved, in 15% to 44% of the cases also aortic valve regurgitation is present [34]. Loeys-Ditez syndrome is an autosomal dominant genetic aortic aneurysm syndrome. The life expectancy for these patients is quite low, around 37 years, because aortic dissection occurs at younger age and at smaller diameters.

Also the genetic heritage is important - familial aggregations of aortic aneurysms and dissections are observed, due to genetic mutation [33].

Another common cause of aortic aneurysm is the Erdheim-Gsell media degeneration, which undermines the vascular mechanic of the vessel, decreasing the distensibility and increasing wall shear stresses.

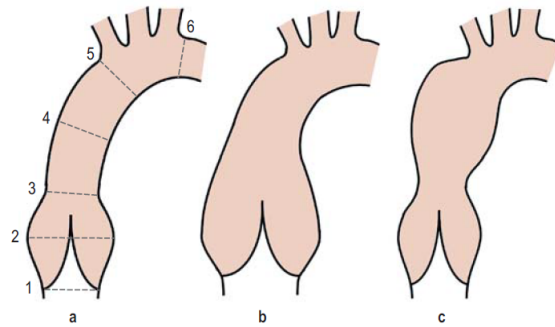Moreover, patients with bicuspid aortic valve (BAV) syndrome (Figure 1.5)

Figure 1.4: Configuration of aortic root and ascending aorta
a) Normal configuration; b) Aortic root dilatation in Marfan syndrome
patients; c) Aneurysm in the tubular part of the ascending aorta [33]

are prone to develop an aneurysm - almost 26% of them develop the pathology
[33]. If surgical aortic replacement is performed soon enough, the incidence of
aortic dissection is low (3.1% per 10 000 patients-years[35]), but subjects with
BAV have an altered hemodynamics, with turbulent eccentric flow acceleration
in the ascending aorta. Furthermore, 75% of patients with Turner syndrome
show cardiovascular anomalies (one in four patients has a dilated aorta and
has a higher risk of dissection [27]).

Finally, patients who were affected by aortitis, often develop postinflammatory
dilatation of the aortic root and aortic valve regurgitation.

In addition to the common symptoms, an aortic regurgitation murmur can be
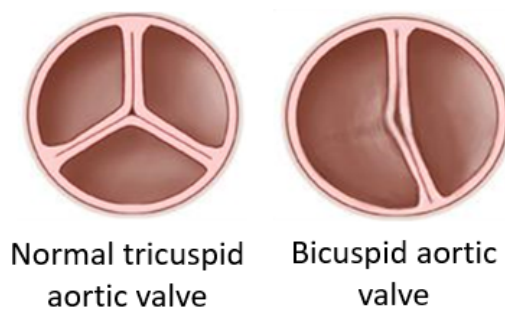

Figure 1.5: Representation of a normal tricuspid valve (on the left), with its
three leaflets and a biscuspid aortic valve (on the right), with its two leaflets.
Adapted from [36]

7

heard, due to the dysfunction of the aortic valve complex.

Treatments. In accordance with ACCF/AHA Guidelines [24], the patients should be divided into symptomatic and asymptomatic. The first class of patients should be evaluated for prompt surgical intervention, unless the quality of life is substantially impaired or the life expectancy is low, due to comorbid conditions. For asymptomatic patients, the first factor to be considered is the diameter: ascending aortic aneurysms are considered at risk of rupture if the diameter is ≥ 55 mm. When the aortic diameter is $> 60\ mm$, the risk of dissection or rupture increases sharply (Figure 1.6) [25]. Providing
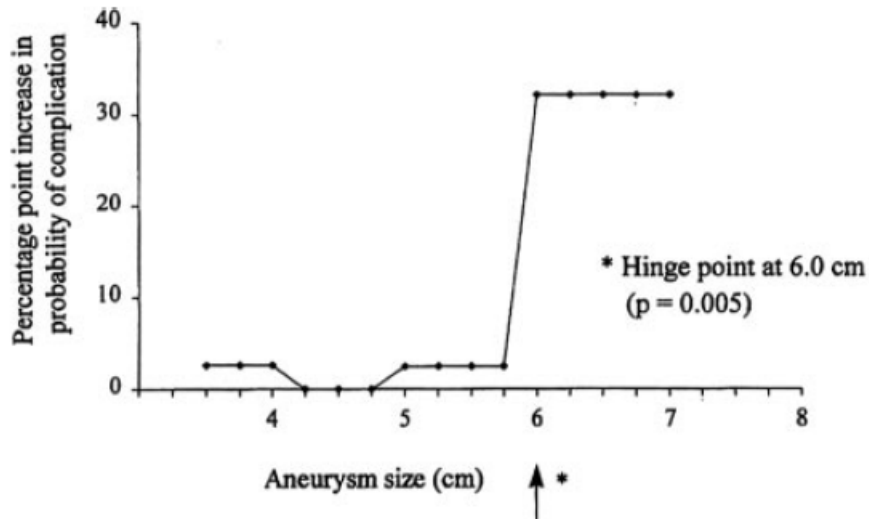

Figure 1.6: Effect of aortic aneurysms diameter on risk of complication. For thoracic aortic aneurysms of all etiologies. [24]

a generally valid value is difficult because aortic diameter increases with age, body weight, body height [37] and other factors associated with the specific characteristics of the patient. For example, in subjects with Turner syndrome, the aorta is dilated when the diameter is $\geq 2.0\ cm\backslash m^2$ while at $\geq 2.5\ cm\backslash m^2$ a high risk of dissection is present [38]. Patients affected by Marfan syndrome are considered at risk of dissection with a diameter $\geq 45\ mm$ [33]. Other factors to be considered are [32, 39]:

- A familial predisposition to aortic complications;

- Growth rate $(> 5\, mm \backslash y)$, even if the diameter is $< 55mm$;

- Aortic valve morphology. If a valve needs to be replaced or repaired or if the diameter of the aortic root or the ascending aorta is $\geq 45\ mm$, the concomitant repair of the aortic root or replacement of ascending aorta should be considered;

- Corrected or uncorrected aortic coarctation.

When the surgery is not required, the medical therapy aims at reducing wall shear stresses. First of all, it is important to minimize cardiovascular risk factors (hypertension, smoking, cholesterol) , to reduce the chance of atherosclerosis and to control blood pressure. Moderate physical activity can help prevent atherosclerosis-related aneurysms [40]. A continuous monitoring of the aneurysm is crucial to assess the evolution of the pathology.

Surgical treatment. Surgical treatment is based on aneurysm location: if it is distal to the sinotubular junction, the implantation of a tube graft is sufficient (Figure 1.7), but if the aneurysm involves also the aortic root, regurgitation is often present.

In the second case, the substitution of the valve is needed and either the valve and the aortic prostheses can be implanted sequentially or a composite graft (with a mechanical aortic valve integrated into the tube graft) can be used. In this case, the complication lies in the reimplantation of the coronary ostia and in the need for a lifelong anticoagulant therapy [33]. The substitution of aortic valve leads to different long-term complications, such as endocarditis, thromboembolism and bleeding [41]. In the case of a normal tricuspid valve, an aortic valve-preserving technique is performed. The classic technique is the David procedure, which involves the re-implantation of the aortic valve into a tubular graft or into a graft with sinus functionality.
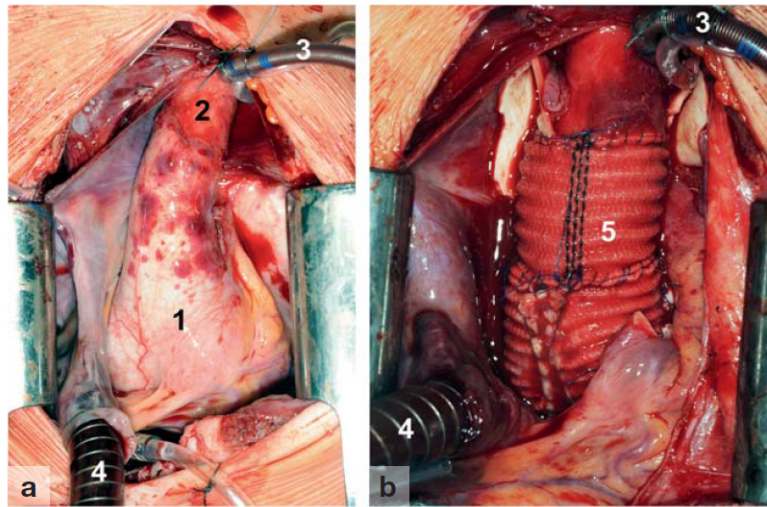
Figure 1.7: Operative site in a patient with an ascending aneurysmatic aorta a) Prepared aneurysm of the ascending aorta approached through a median sternotomy. b) After aneurysm resection and graft implantation 1.Aneurysm of the proximal ascending aorta 2.Non-aneurysmal distal ascending aorta 3. Arterial cannula 4.Venous cannula of the extracorporeal circulation 5. Implanted aortic graft after aneurysm resection [33]

If the aneurysm is proximally limited to the sinotubular junction and distally to the aortic arch, the aneurysm is resected and a supra-commissural graft is implanted under a short period of aortic clamping, with distal anastomosis just below the aortic arch [25]. The surgical mortality associated with aortic replacement goes from 1% for younger patients to > 5% for older ones, depending also on whether the aortic valve has been replaced, on co-morbidities and on the experience of the surgeon [6, 7].

Acute aortic dissection

Classic aortic dissection comprises 80-90% of all AAS [42] and it is one of the main complications of ascending aortic aneurysm. It starts as a tear in the intima, then the blood propagates into the media developing a true and a false lumen, separated by an intimal flap. It has an incidence of 2.6 to 3.5 cases per 100 000 person-years [43, 44]. The majority of patients are male ($\backsim$ 65%) and

the AAD mostly occurs in the seventh decade of life (mean age 63 years) [25]. This pathology, as reported in Figure 1.3, is one of the three AAS pathologies. These diseases are classified based either on the duration [24, 25] or on the anatomic location of the AAs. For what it concerns the duration, it is measured from initial onset of symptoms to hospital presentation. The two classification criteria are reported respectively in Table 1.1 and Table 1.2 and represented in Figure 1.8.

Class	Duration
Acute	< 14 days
Subacute	$15 - 90$ days
Chronic	> 90 days

Table 1.1: Classification of AASs base on duration

Class	Location
type I	Both ascending and descending aorta
type II	Ascending aorta
type III	Descending aorta

Class	Location
type A	Ascending aorta and arch
type B	Descending aorta

Table 1.2: DeBekey (left) and Stanford AASs classification (right)

IMHs involve 5-25% of AAS. This pathology primarily affects the media and may be caused by the rupture of the vasa vasorum within the medial layer of the aortic wall. It usually occurs in the descending tract of the aorta and appears in patients with significant atherosclerotic disease. One of the most common manifestations is abrupt chest and/or back pain. Only 10% of IMHs regress spontaneously and up to 47% progress to dissection [45]. The overall mortality is similar to the one of aortic dissection.

PAU is an outpouching of blood through the internal elastic lamina. It usually originates from an inflammatory erosion due to the atherosclerosis plaque. It composes 2-7% of all cases of AAS. It usually coexists with IMH and can progress to aortic dissection, pseudoaneurysm and frank rupture [45]. The
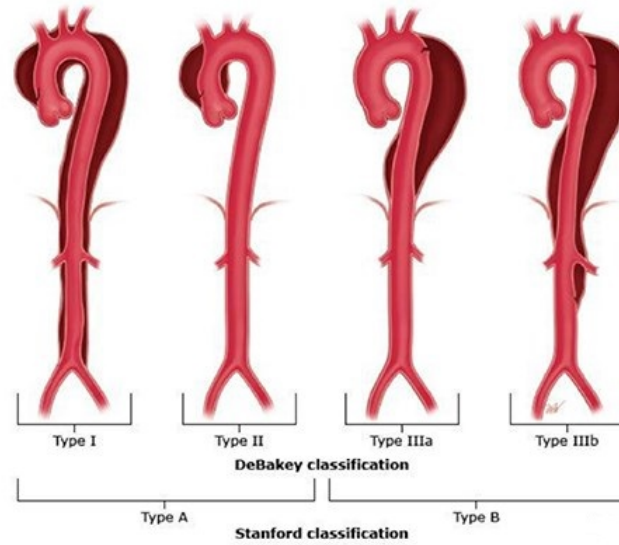
Figure 1.8: Classification of AAs - Visual representation [47]

patients are usually over 65, smokers and with multiple comorbidities, like hypertension and coronary disease. Most patients manifest acute chest or back pain, but 25% can be asymptomatic [46].

Dissection can also happen as a consequence of traumatic aortic injury (TAI). TAI consists of a partial or complete transection of the aorta and it is the second most common cause of death in patients with blunt thoracic trauma [46].

1.2   Imaging techniques

MRI is the preferred diagnostic technique to assess aneurysms. Thanks to technological progress, advanced methodologies have been developed in the last few years, allowing to obtain additional information besides the anatomy. It is the case of PC-MRI and 4D-Flow, which follows the same basic physical principles as MRI, but enables to obtain also quantitative information. Since these techniques were used as sources of data for this thesis work, they will be introduced in the following sections.

1.2.1 Magnetic Resonance Imaging

MRI exploits the abundant presence of ^{1}H proton in human tissues containing water. Each ^{1}H has its own spin and since these atoms are provided of a positive charge, they produce an angular moment and a magnetic moment. Normally the spins are randomly oriented, but when an external magnetic field $\vec{B}_0$ is applied, they can assume only two configurations: the spin-up one (lower energy), where they are oriented as the external magnetic field, and the spin-down one (higher energy), where the orientation is opposite (see Figure 1.9). At human body temperature, there is always a spin-up surplus of 3
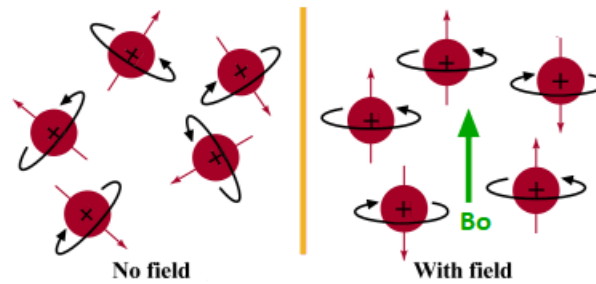
Figure 1.9: Spin orientation with (on the left) and without(on the right) magnetic field [48]

$ppm\backslash T$, that generates a net magnetization $\vec{M}_0$, oriented as $\vec{B}_0$. The spins are not static: they have a precession motion around $\vec{B}_0$ direction with a titling angle of 54°(Figure 1.10). The frequency of this motion is called Larmor frequency and it depends on the intensity of the magnetic field applied to the protons. A second magnetic field $\vec{B}_1$ with an angular velocity equal to the angular velocity of the precession motion of the spins can now be applied. Since the two angular velocities are the same, the spins will constantly be subjected to the action of $\vec{B}_1$. The net magnetization moment $\vec{M}$ will now assume a new direction, tilted of a certain angle with respect to $\vec{B}_0$ direction (Figure 1.11). This angle depends not only on the intensity of $\vec{B}_1$, but also on the duration of
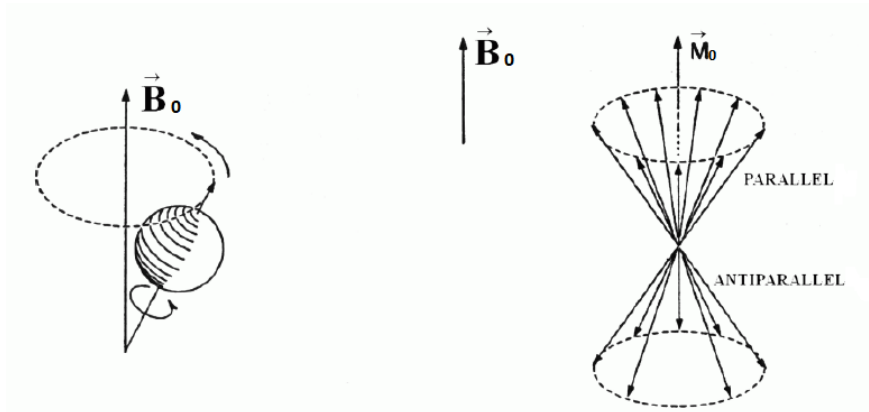
Figure 1.10: Precession motion [49]

application of this second magnetic field. This phenomenon is called resonance. When $\vec{B}_1$ is removed, $\vec{M}$ will tend to return to its initial configuration. Based on the time of application of $\vec{B}_1$, $\vec{M}$ can rotate on an orthogonal plane with respect to $\vec{B}_0$ (90° impulse) or can assume an anti-parallel configuration with respect to $\vec{B}_0$ (180° impulse).

The magnetic nuclear resonance phenomenon is exploited to excite the nuclei of the examinated sample. When they return to the equilibrium condition, they emit a signal that is harvested and studied to have information on the sample. But these signals are mediated on the whole volume. To study the sample in more detail, it is divided into small volumes (voxels) and the signal
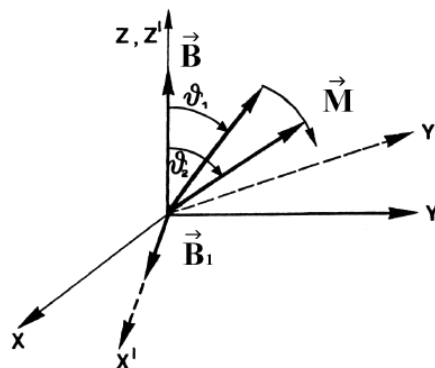

Figure 1.11: Variation of $\vec{M}$ when both the static magnetic field $\vec{B}_0$ and rotating magnetic field $\vec{B}_1$ are applied

coming from each portion is differentiated. In order to do that, the system for the magnetic resonance is composed of the following components:

- A magnet able to generate a static magnetic field at high intensity, usually between 1.5-3T;

- A radio frequency (RF) transmitter, that has the role to generate a field with the same frequency of the precession motion of the nuclei to produce the overturn;

- A system of gradients, able to produce variables magnetic fields in time and intensity;

- A computer system, to elaborate the images.

The system of gradients is used to code the different voxels of the sample. Usually, the three directions are defined to have the z-axis overlapping with the magnet axis and with the z-axis of the patient, the x-axis in horizontal direction, while the y-axis is vertical. A gradient along z ($\vec{G_z}$) is used to select a specific slice of the patient. After the application of $\vec{G_z}$, an RF impulse is applied to produce an overturning of 90° of the precession axes. The signal produced when this impulse ceases is not harvested. After a specified time,
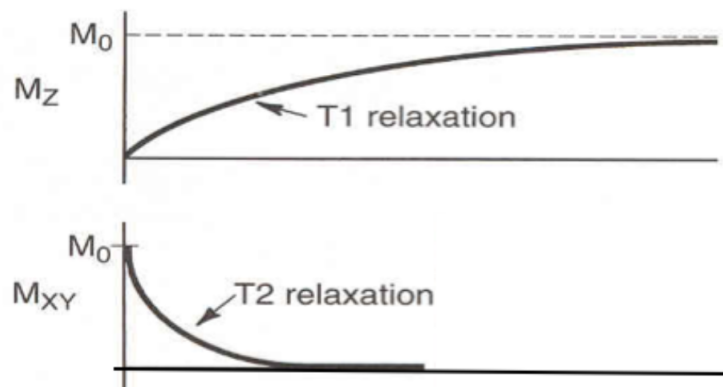

Figure 1.12: Reppresentation of T_1 ans T_2

a 180° impulse is applied. The RF impulse causes some low-energy protons to switch to a high-energy state, giving energy to the lattice. This is known as spin-lattice, (T_1 relaxation) and it is an expression of the thermodynamic connection between the spin and the lattice. Another phenomenon is the spin-spin or T_2 relaxation, which happens when atoms that were in phase start to get out of phase. This gives an indication of the local magnetic homogeneity (Figure 1.12). After the 180° impulse, relaxation occurs and the atoms return to their initial state in static magnetic field. Before applying 180° impulse, a gradient along y is produced ($\vec{G}_y$) for a certain time. This will produce a different precessing velocity of the atoms, based on their y coordinate. When the signal ceases, the atoms will all start again to precess at the same velocity but out of phase, with angles that reflect their position along the y-axis. After the 180° impulse, a gradient along x, $\vec{G}_x$, is applied and the atoms will assume different precession velocities based on the x coordinate, while maintaining the phase displacement due to $\vec{G}_y$. In conclusion, $\vec{G}_z$ is used to select a slice, $\vec{G}_y$ indicates the phase and $\vec{G}_x$ the frequency. These data are harvested and studied by the computer system to reconstruct the images, using Fourier transformation. MRIs can then be stored as DICOM images, which are the standard for the communication and management of medical imaging and are organized in matrices. These images contain also DICOM tags, able to provide information on the acquisition, on the images and on the patient.

1.2.2   PC-MRI

Since MRI technique has evolved considerably in the past few years, phase-contrast flow measurements are increasingly used as an additional source of quantitative functional information in cardiac MR imaging [50].
When a spin moves along a magnetic field gradient, it acquires a shift in his phase of rotation compared to stationary spins [51]. This phase shift ϕ is given

by equation 1.1.

$$\phi = \gamma \int_0^t B_0 + G(\tau) * r(\tau) d\tau, \tag{1.1}$$

where γ is the gyromagnetic ratio, $G(t)$ the gradient field and r the position of the spin. In stationary tissues, the phase shift is compensated with a bipolar gradient (i.e. opposite and equal in amplitude to the first gradient), while the phase shift induced by other sequence parameters is eliminated by repeating the measurement with an inverted bipolar gradient. These two data sequences are then subtracted and the obtained phase difference $\Delta\phi$ is used for a voxelwise calculation of the velocities (Equation 1.2).

$$\Delta\phi = \gamma * \Delta m * v, \tag{1.2}$$

where m is the difference between the first moment of the gradient-time curve and v the spin velocity. The phase shift is then measured and converted to a velocity, according to Equation 1.3.

$$v = \frac{VENC}{\pi} \Delta\phi, \tag{1.3}$$

where $VENC$ determines the highest and the lowest values of velocity detectable with a phase-contrast sequence. Since $VENC$ is inversely related to the area of the flow encoding gradients, to encode smaller velocities and maintain the imaging time, stronger amplitudes are needed. The correct $VENC$ choice is crucial: a too high $VENC$ leads to a decrease in the signal-to-noise ratio (SNR) and in the measurement sensitivity, while a too low one produce aliasing, easy to detect since in velocities images some voxels have an inverted signal intensity compared with that of surrounding voxels.

In conventional imaging sequence, the phase information is arbitrary, so it is not stored, while in phase-contrast MRI, the phase information is used to calculate the velocity of each voxel and to form the velocity image.
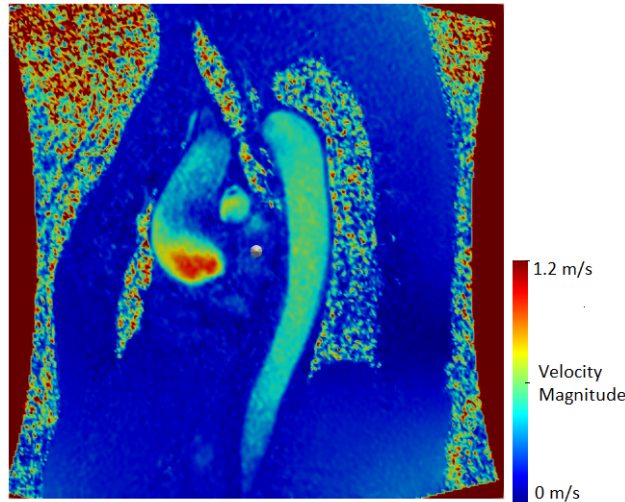
Figure 1.13: Example of a PC-MRI image

There are two possibilities to synchronize the measurements of MR imaging data with the cardiac cycle, the prospective and the retrospective gating technique. In the prospective one, data acquisition is triggered by a trigger signal and the duration of acquisition is fixed. This allows adjusting mild arrhythmia. The trade-off of this technique is that the flow of late diastole may not be measured correctly, since there is a window between the end of the acquisition and the next trigger signal, called arrhythmia rejection window, during which data are not sampled. Prospective gating is used in those sequences that can be performed in a breath-hold. In the retrospective gating technique, data acquisition is done continuously during the whole cardiac cycle. The trigger signal is then used during image reconstruction to assign data to the different phases of the cardiac cycle. Since each cardiac cycle is different, the data must be interpolated to represent a mean cardiac cycle and for this reason small inaccuracies are inherent with this technique. The greatest advantage is that the whole cardiac cycle can be acquired and most of the acquisitions made during normal breathing use this technique. The gating technique can not be assessed from the PC-MRI sequence, this information is

usually given in the manual of the MR imaging system.

1.2.3 4D-FLOW

Thanks to the development of PC-MRI techniques, it was possible to acquire a time-resolved (CINE) three-dimensional (3D) PC-MRI with three directional velocity encoding, also known as 4D-Flow [52]. The same technique adopted to encode the velocity along one direction in PC-MRI is used along the three spatial dimensions, so gradients along three perpendicular directions are used. To encode the velocity in each direction, three different magnetic field combinations are generated and in some cases it is possible to set a different VENC value for each direction (multi-VENC acquisition). The measurements of the 3D velocity are possible thanks to the interleaved four-point velocity encoding: four images are acquired, one as a reference and the others to encode the velocity along three orthogonal directions (x,y,z) [53–55]. Also in this case multiple cardiac cycles are collected and then the data are distributed using the "k-space segmentation": the data are collected over multiple RR-intervals and during each cardiac cycle only a fraction of the entire 4D-Flow data is measured. The cardiac cycle is divided into intervals, whose duration depends on the subject's cardiac cycle length and each interval corresponds to a frame. When all the data are acquired four datasets are created, one containing the anatomy (called "magnitude") and three containing the velocities ("Vx","Vy" and "Vz") (Figure 1.14). Due to the great amount of data, the scanning time is quite long, it ranges from 5 to 20 minutes for typical cardiovascular applications and this constitues the great limitation of this methodology.

The sources of inaccuracies can be various, but the most common are eddy currents, Maxwell terms and gradient field nonlinearity [52]: if needed it is important to correct such inaccuracies before the post-processing.

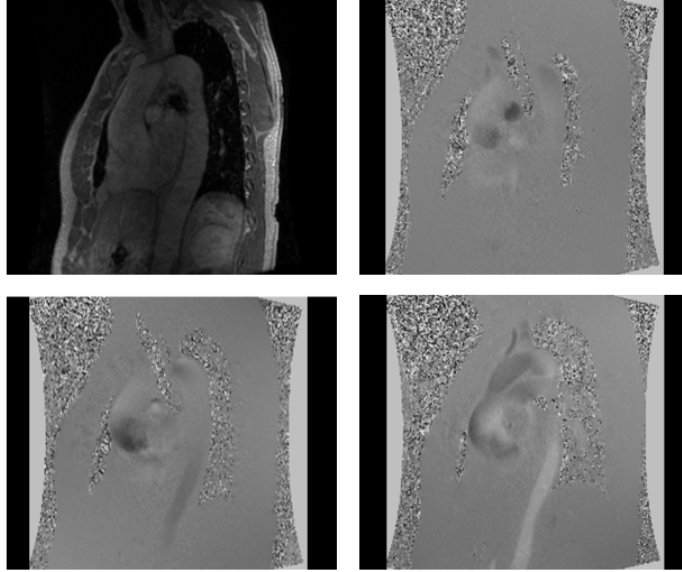The great advantage of this technique is that it can provide information

Figure 1.14: 4D-Flow images. The top left figure represents the magnitude dataset, while the other the three velocities

on the temporal and spatial evolution of 3D blood flow of any cardiac or vascular region of interest. This allows to better inspect the consequences of cardiovascular diseases and hemodynamic changes. Besides the velocity along the three spatial dimensions that can be directly calculated using 1.3 and used to impose boundary conditions, the information that can be extracted are various:

- *Anatomy.* It is possible to approximate the vascular geometry generating a non-contrast 3D PC-MRA, without the need for further MRA acquisitions [52]. This allows measuring quantities such as the diameter of the vessel;

- *Velocity-related variables.* Since velocity data are available, quantities as flow rate (Q) and wall shear stresses (WSS) can be computed. Other parameters that can be assessed are peak pressure gradient, pressure difference [56], pulse wave velocity [57] and turbulent kinetic energy [58]. It is also possible to visualize blood flow patterns through the streamlines.
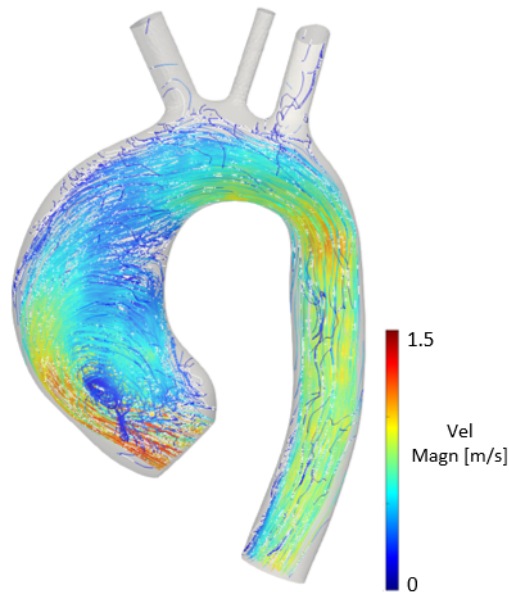
Figure 1.15: Streamlines of an aneurysmatic aorta obtained from 4D Flow images

An example of streamlines is reported in Figure 1.15.

All these quantities are useful to better characterize cardiovascular diseases. 4D Flow is mainly used as an acquisition research protocol and has some limitation. The main limitation has already been highlighted and it is the long acquisition time. Other limitation are here reported:

- The spatial and temporal resolutions are low. This may negatively affect the collection of quantitative data, not allowing to obtain accurate measurements, and the anatomic reconstruction, not allowing to visualize some districts;

- Motion artifacts cannot be avoided, since the acquisition cannot be performed in apnea and since the heart keeps beating . This is partially solved using prospective and retrospective cardiac gating;

- In case of detailed turbulent flow, the fine flow structures at the sub-voxel scale may not be acquired if temporal and spatial resolution

are inadequate [59];

- When a voxel is located at the boundary between the static and the dynamic domain, the phase shift measured by PC-MRI is the average of both stationary and flowing spins. This leads to unreliable velocity measurements and partial volume effects [60].

Chapter 2

State of art

In the first part of this chapter a brief introduction to Computational Fluid Dynamic (CFD) and Fluid Structure Interaction (FSI) modeling is reported, pointing out the advantages and disadvantages of these methodologies. After an introduction to the Finite Element Method, the subsequent paragraph present the Coupled Momentum Method for Fluid-Solid Interaction formulation, which allows solving FSI problems with lower computational costs.
The second part of this chapter offers an insight into current FSI studies that focus their attention on ascending aneurysmatic aorta hemodynamic and on fluid dynamic changes induced by the reconstruction of the aorta by means of a PET graft.

2.1 Introduction

Computational fluid dynamics (CFD) is used in many engineering fields and recently is assuming increasing importance also in medical applications, in particular in cardiovascular medicine ([61, 62]). Used in combination with cardiovascular imaging, it allows to characterize complex physiological pressure and flow fields at a temporal and spatial resolution unachievable by a clinical methodology and to compute quantities that cannot be directly measured (e.g. WSS, oscillatory shear index, etc.). Providing an insight into pathologies development and mechanisms, it allows to predict individual risks and to develop a patient-tailored strategy, representing a powerful tool for the clinicians. The development of a patient-specific CFD model starts with the segmentation of clinical images, which consists of the reconstruction of patient's anatomy. The clinical images, of which the most common are MR images and CT scans, must provide sufficient anatomical and physiological detail. The obtained geometry is then divided into a number of discrete elements (volumes or cells), while the dynamic evolution is divided into discrete time steps (temporal discretization). Boundary conditions (BCs) are then applied at the inlet, outlet and wall of the model. BCs are a set of applied, patient-specific and physiological parameters that define the physical conditions at the boundaries of the geometry. Their detail and completeness will determine the simulation capability to mimic reality. A set of equations will define the physical problem that needs to be solved and, to compute the solution, a solver is exploited. Today, various software packages are available for the resolution of computational fluid dynamic problems (e.g. Abaqus, Ansys Fluent, SimVascualar, etc.). Finally, the developed model is validated against acceptable standards, to ensure the possibility to extract reliable quantities.

To describe fluid dynamic motion, two approaches are possible:

- Lagrangian Approach: the motion of particles through time is followed, labeling them by some vector field x_0. The flow is represented by a function $X(x_0, t)$;

- Eulerian approach: the fluid motion is observed in specific locations in the space as time passes. The field is represented as a function of position x and time t. For example, the flow velocity v is described by $v(x, t)$.

The great limitation of CFD technique lies in the rigid wall assumption, which precludes the observation of many important phenomena in the cardiovascular system. Indeed, blood vessels are deformable tubes that change their size when blood pressure and velocity change, storing blood during systole and releasing it during diastole. Neglecting vessel wall deformation implies different inaccuracies, such as the overestimation of WSS and the impossibility to detect any wave propagation phenomena. To take into account for wall deformability and for the interaction between solid and fluid domain, fluid-structure interaction (FSI) approach must be exploited. Also in this case some assumptions are made, regarding for example the properties of the wall which are difficult to be obtained experimentally and often unknown [63]. Two different approaches may be used in FSI models:

- Monolithic approach: flow and structure displacements governing equations are solved simultaneously, with a single solver;

- Partitioned approach: flow and structure displacements governing equations are solved separately, with two distinct solvers coupled with staggered iteration process. In this case, the solution of one solver is used to impose the boundary condition for the other at the fluid-structure interface.

The fluid-solid coupling can be modelled through two different methodologies: a weak and a strong coupling algorithm. On the one hand, 1-way FSI, is based

on the assumption that the deformation on the solid domain only slightly affects the fluid dynamic of the system, so the coupling occurs only between fluid and solid and not vice versa. Accordingly, a convergent solution is computed for the fluid domain and an external load is applied to the solid domain to account for the effect of the fluid domain. On the other hand, the strong coupling 2-way FSI algorithm considers that the fluid domain causes deformation on the solid domain, which in turn alters the fluid dynamic. Given the complexity of this approach, the FSI algorithm is more time consuming than CFD simulation. To overcome the problem of high computational costs but still considering wall deformation, a new formulation called Coupled Momentum Method for Fluid-Solid Interaction (CMM-FSI) was developed by C.A. Figueroa [12]. The formulation starts from a conventional stabilized finite element formulation for the Navier-Stokes equation in a rigid domain and modifies it in order to account for the effect of the deformability of the wall on the fluid domain [12].

A deeper insight into the CMM-FSI will be given in the following paragraphs. Since this methodology starts from a finite element formulation (FEM), also a brief introduction to this technique will be provided.

2.1.1 Finite Element Method

The Finite element Method (FEM) allows to find an approximate numerical solution to the mathematical model of a physical problem, at any point of the domain. The key aspect is the discretization of a continuum system, which allows to obtain the solution at a finite number of points solving algebraic equations, instead of solving differential equations in the continuum domain. The basic steps are the following:

- System simplification and discretization into elements;

- Computation of elemental stiffness matrices;

- Assembly of global stiffness matrix and load vectors;

- Imposition of boundary conditions;

- Resolution of the system of equations, leading to displacements computation;

- Determination of stresses and deformations.

First of all, the strong formulation of the mathematical model used to represent the physical system (Figure 2.1) is written. Generally, the strong formulation can be described as:

$$Au = -b \qquad \forall x \in \Omega, \qquad \begin{cases} u_i = \bar{u}_i & \forall x \in \Gamma^u \\ \sigma_{ij} n_j = \bar{t}_i & \forall x \in \Gamma^t \end{cases} \qquad (2.1)$$
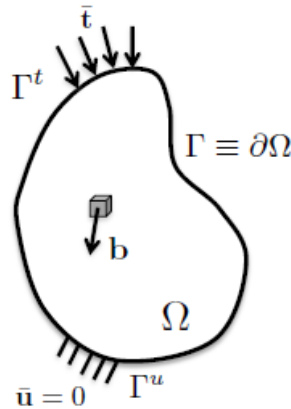
Figure 2.1: General representation of a physical system

Then, in order to use FEM, the Integral form (or weak form) needs to be obtained, using either the Potential Energy (only for conservative systems) or the Galerkin's Method. This latter uses a set of governing equations and it

is presented as one of the weighted residual methods. The exact solution of the problem solves the equation 2.1 at every point x, while in an approximate domain, the solution $\bar{u}$ introduces an error $e(x)$, called the residual:

$$e(x) = A\bar{u} + b \tag{2.2}$$

The weighted residual method sets the resisual relative to a weighting function ϕ_i to zero:

$$\int_\Omega \phi_i(A\bar{u} + b)dV = 0, \qquad i = 1...n \tag{2.3}$$

$$\bar{u} = \sum_{i=1}^n Q_i G_i \qquad \phi = \sum_{i=1}^n \phi_i G_i \tag{2.4}$$

In the Galerkin method the weighting functions ϕ_i are chosen from the basis function used to construct $\bar{u}$.

According to the Galerkin method, the choice of G_i (Equation 2.4) is arbitrary and the coefficients Q_i need to be determined satisfying Equation 2.3 for every
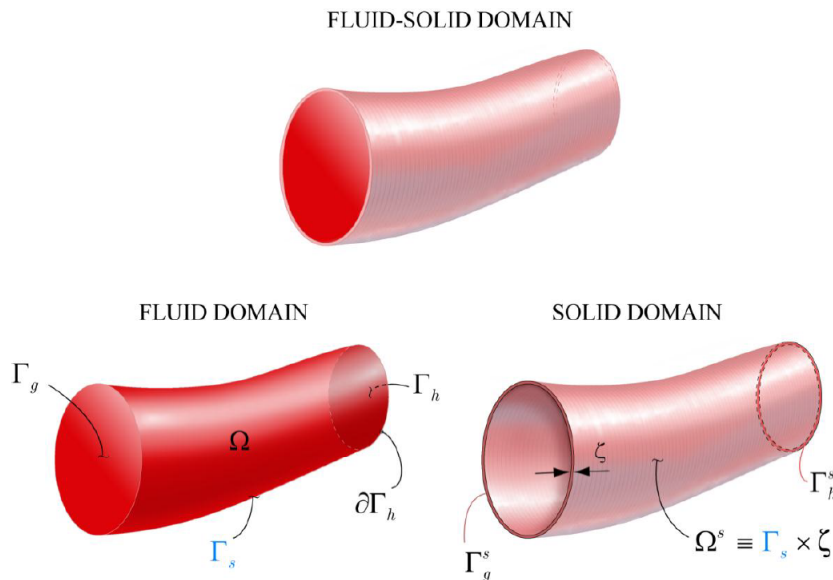
Figure 2.2: Schematic representation of the Fluid and Solid Domains and their boundaries

function ϕ (Equation 2.4), where ϕ_i are arbitrary except for requiring that ϕ satisfies homogeneous boundary conditions where $\bar{u}$ is prescribed. The solution of Equation 2.3 for Q_i yields the approximate solution $\bar{u}$.

The deformable continuum can now be divided into a set of subdomains, i.e. the finite elements, generating the mesh of the system. The weak form of the problem can now be written as the sum of the term related to each element. The blood flowing in a vessel can be modelled as the flow of an incompressible Newtonian fluid in a domain $\Omega \in R^3$. The boundaries of the domain can be denoted by $\Gamma = \Gamma_g \cup \Gamma_h \cup \Gamma_s$ (see Figure 2.2). The incompressible Navier-Stokes equation can be used and its strong formulation takes the form expressed in Equation 2.5.

$$\rho\vec{v}_{,t} + \rho\vec{v}\cdot\nabla\vec{v} = \nabla p + \nabla\cdot\tau + \vec{f}, \qquad (\vec{x},t) \in \Omega \times (0,T)$$
$$\nabla\cdot\vec{v} = 0, \qquad (\vec{x},t) \in \Omega \times (0,T) \tag{2.5}$$

where ρ is the blood density, $\vec{v}$ is the fluid velocity, p is the pressure, $\vec{f}$ is the prescribed body force per unit volume and τ is the viscous stress tensor [12]. The domain Ω can be discretized by n linear element, Ω_e. The weak form becomes:

$$B_G(\vec{w},q,\vec{v},p) = \underbrace{\int_\Omega \{\vec{w}\cdot(\rho\vec{v}_{,t} + \rho\vec{v}\cdot\nabla\vec{v} - \vec{f}) + \nabla\vec{w}:(-pI+\tau) - \nabla q\cdot\vec{v}\}d\vec{x}}_{\text{Navier-Stokes equation}} +$$
$$+ \underbrace{\int_{\Gamma_h}\{-\vec{w}\cdot\vec{h} + qv_n\}ds}_{\text{Inlet BCs}} + \underbrace{\int_{\Gamma_s}\{-\vec{w}\cdot\vec{t}^f + qv_n\}ds}_{\text{Wall BCs}} + \underbrace{\int_{\Gamma_g} qv_n ds}_{\text{Outlet BCs}} = 0$$

$$\tag{2.6}$$

where $w \in W_h^k$ and $q \in P_h^k$ (W_h^k and P_h^k are the weight function spaces) [12]. $\vec{t}_f$ represent the effect of the wall on the fluid domain that will be better specified in the following section.

Since the standard Galerkin method is unstable for advection-dominated flows and in the diffusion dominated limit for equal-order interpolation of velocity and pressure, a stabilized method is utilized, adding stabilization terms in Equation 2.6 [12].

2.1.2 Coupled Momentum Method for Fluid-Solid Interaction

A novel method was designed to couple fluid and solid domain: the CMM-FSI formulation. The main features of this formulation are the following [12]:

- The zero-velocity condition (Dirichlet) on the lateral surface of the fluid domain is substituted with traction condition (Neumann), which is determined using elastodynamic equations that describe the motion of the vessel;

- The thin wall approximation is used for the vessel wall. The traction force is related to a body force for the vessel wall, which is related through the elastodynamic equations with mass and stiffness of the vessel wall;

- The mass and stiffness of the vessel wall are described using a membrane approximation. This approximation is acceptable because the cardiac pulse has a long wavelength (meters) compared to the diameter of the artery (centimeters). The advantage is that no additional degrees of freedom besides the membrane wall velocity are needed. Furthermore plain strains are assumed thank to the this approximation;

- A strong coupling approach is used, so the vessel wall and the boundary of the fluid domain have the same degrees of freedom. The fluid

velocities and accelerations are time integrated to obtain the membrane displacements;

- For the coupled problem a linearized kinematic approach is adopted. As a consequence, the same Eulerian frame can be used for both the solid and the fluid equations. The fluid mesh and the fluid-solid interface are kept fixed, but the fluid-solid interface nodes will have a non-zero velocity. This allows having a reduced computational time compared to Arbitrary Lagrangian Eulerian (ALE), where the fluid domain is not constant and an Eulerian formulation is not appropriate. In this case, a mixed Lagrangian-Eulerian formulation is used, introducing the concept of grid velocity. This grid velocity is defined in such a way that it matches the physical velocity of the fluid-solid interface, while the rest of the domain varies according to a mapping between the current and the reference configuration. This concept of grid velocity and the fluid equation written in the Lagrangian-Eulerian frame are the two key concepts of the ALE formulation;

- A linear membrane under transverse loading is inherently unstable. To overcome this problem, a linear membrane enhanced with shear modes is used, to add stresses that provide stiffness to the structure, without using additional degrees of freedom.

This allows to take into account the motion of the wall and the blood flow in a single weak form of the problem: to incorporate the wall motion, only minimal changes in the stiffness matrices and residuals of the rigid wall finite element model are required. For this reason, the computational effort is comparable to that of the rigid wall formulation, but this approach enables to respect the patient-specific anatomy, to simulate the wave-propagation phenomena and to observe a linearized description of wall deformation.

This approach will not produce results comparable to the ones of the ALE formulation when the deformation is too large, but will produce reliable results for larger cardiovascular models in a clinically-relevant time frame [12].

Wall deformation is incorporated in equation 2.6. Given the thin wall approximation, the solid domain Ω_s can be topologically related to the surface defined by the lateral boundary of the fluid domain Γ_s. The solid's weak form defined in Ω_s will be related to the traction integral on the lateral boundary of Γ_s. This allows having a strong coupling between the degrees-of-freedom of fluid and solid domains and provides an expression for the traction force $\vec{t}_f$ in equation 2.6. The strong formulation of the vessel wall problem can be described by the equation:

$$\rho^s \vec{u}_{,tt} = \nabla \cdot \vec{\sigma}^s + \vec{b}^s, \qquad (\vec{x}, t) \in \Omega^s \times (0, T) \tag{2.7}$$

where $\vec{u}$ is the displacement field, ρ^s is the density of the vessel wall, $\vec{b}^s$ is the prescribed body force per unit volume and σ^s is the vessel wall stress tensor. To relate the solid problem with the lateral boundary of the fluid domain, it is necessary to map Ω_s in Γ_s. Then the surface traction $\vec{t}^f$, acting on the fluid lateral boundary, can be related to $\vec{t}^s$, the surface traction acting on the vessel wall, through the equation 2.8.

$$\vec{t}^f = -\vec{t}^s \tag{2.8}$$

Since in a thin membrane the internal surface traction $\vec{t}^s$ will be felt uniformly through the wall thickness and thanks to the thin membrane approximation, the body force $\vec{b}^s$ can be related to $\vec{t}^f$ through the Equation 2.9.

$$\vec{b}^s = -\frac{\vec{t}^f}{\zeta} \tag{2.9}$$

where ζ is the thickness of the membrane. Given the strong coupling of the degrees-of-freedom of the fluid and solid domain, the displacement, velocity and acceleration fields on the fluid solid interface are identical. So the semi-discrete Galerkin finite element formulation has the following weak expression:

$$\int_{\Omega_s} \rho^s \vec{w} \cdot \vec{v}_{,t} d\vec{x} + \int_{\Omega_s} \nabla \vec{w} : \sigma^s d\vec{x} = \int_{\Omega_s} \vec{w} \cdot \vec{b}^s d\vec{x} + \int_{\Gamma_h^s} \vec{w} \cdot \vec{h}^s ds \qquad (2.10)$$

This equation can then be mapped into the lateral boundary of the fluid domain Γ_s, finding the expression for the traction term of equation 2.6:

$$-\int_{\Gamma_s} \vec{w} \cdot \vec{t}^f ds = \zeta \int_{\Gamma_s} \rho^s \vec{w} \cdot \vec{v}_{,t} ds + \zeta \int_{\Gamma_s} \nabla \vec{w} : \sigma^s ds - \zeta \int_{\partial \Gamma_h} \vec{w} \cdot \vec{h}^s dl \quad (2.11)$$

Equation 2.6 becomes:

$$B_G(\vec{w}, q, \vec{v}, p) = \int_{\Omega} \{\vec{w} \cdot (\rho \vec{v}_{,t} + \rho \vec{v} \cdot \nabla \vec{v} - \vec{f}) + \nabla \vec{w} : (-pI + \tau) - \nabla q \cdot \vec{v}\} d\vec{x} +$$

$$+ \int_{\Gamma_h} \{-\vec{w} \cdot \vec{h} + q v_n\} ds + \int_{\Gamma_g} q v_n ds +$$

$$\underbrace{\zeta \int_{\Gamma_s} \{\vec{w} \cdot \rho^s \vec{v}_{,t} + \nabla \vec{w} : \sigma^s(\vec{u})\} ds - \zeta \int_{\partial \Gamma_h} \vec{w} \cdot \vec{h}^s dl + \int_{\Gamma_s} q v_n ds}_{\text{Term accounting the wall deformation}} = 0$$

$$(2.12)$$

Equation 2.12 defines the weak form of the CMM-FSI formulation [12].

2.2 Numerical studies from literature

Modeling methodologies are acquiring a growing interest in the medical field. Today CFD is a well-establish methodology to study the hemodynamic and pathophysiology of aneurysmatic aorta, while the interest in FSI modeling is widely increasing. To the best of the author's knowledge, there is a lack of
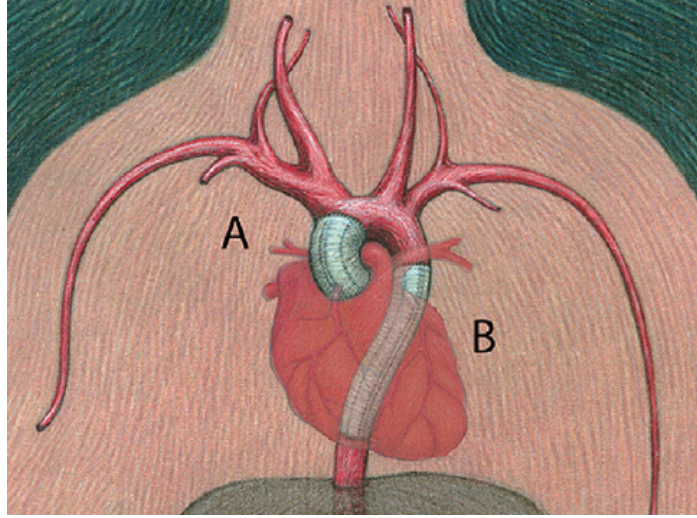
Figure 2.3: Graft position in ascending (a) and descending aorta (b). Adapted from [8]

FSI studies comparing the pre and post-operative hemodynamics of patients who underwent ascending aortic aneurysm graft replacement.The graft is usually made of PET fibers (Dacron). It presents a hyperelastic behavior and its mechanical properties are rather different from those of the human aorta, inducing important hemodynamic changes. Those changes were evaluated in a study carried out in 2011 by Vardoulis *et al* [8]. Proximal aortic compliance and dimensions define the characteristic impedance of arterial tree, while ascending aortic compliance constitutes about half of the total compliance [64]. Some *in vivo* studies demonstrated that the introduction of aortic graft augments systolic and pulse pressure (PP), alters pressure waveforms and increases ventricular afterloads [64–66]. The model proposed by Verdoulis group was a 1D cardiovascular tree model. The arteries were modeled as straight, long, tapered cylindrical segments and the 1D formulation of the Navier-Stokes equation was adopted. In the model, all the systemic arteries greater than 2 mm in diameter were incoporated. The wall material was considered to be nonlinear and viscoelastic. The function of the left ventricle was simulated adopting a varying elastance model described by Sagawa [9]. The distal vessels
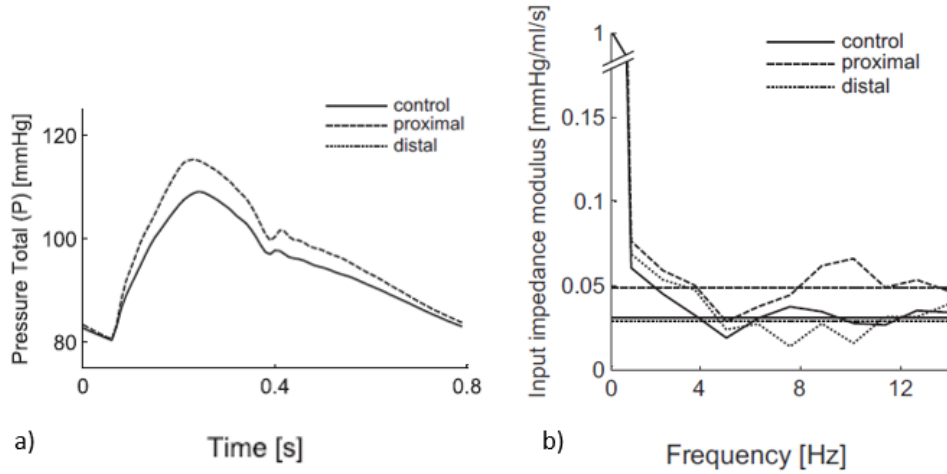
Figure 2.4: a) Pressure wave comparison and b) input impedence module for the proximal (dashed lines) and distal aortic replacement (dotted lines) and for the control case (solid lines). Adapted from [8]

terminated with a three-element Winkessel model. This model was then modified to take into account for the graft placed in two different locations (ascending and descending aorta, see Figure 2.3). The properties of the graft were set based on experimental results. The outcomes showed that the closer the graft was placed to the heart, the greater its impact on systolic arterial pressure (Figure 2.4a) and PP was. This happened because PP is inversely proportional to the total systemic compliance and since ascending aorta is the major contributor to the total compliance, the substitution of this tract with PET graft leads to an augmented PP. Another important result was the increment in proximal aortic characteristic impedance by 58% when the graft was placed in ascending aorta (Figure 2.4b). This led to an amplification of the forward pressure wave. Despite the important simplifications, this study offers a first insight into hemodynamic changes caused by graft implantation. One interesting study regarding aortic graft substitution was led by Jayendiran *et al* [67] in 2018. This study evaluated the radial displacements, von Mises stresses and WSS of a descending aneurysmatic aorta treated with Dacron graft implantation through an FSI approach. A three-dimensional geometry was
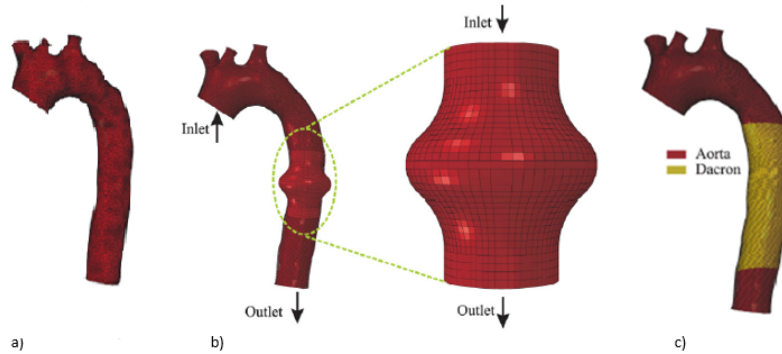
Figure 2.5: Models used for the three simulations. a) Healthy aorta, b) Aneurysmatic descending aorta, c) Aorta treated with Dacron graft. Adapted from [67]

reconstructed starting from two-dimensional scan images of a healthy patient, using Mimic Innovation Suite. The images were segmented with a threshold technique and then a smoothing technique was applied to reduce undesired features. A mesh sensitivity analysis was conducted to choose the proper dimension of the mesh. In the model a small portion of the ascending aorta, the aortic arch and the descending aorta were included and three configurations were simulated, the healthy, the aneurysmatic and the one treated with graft replacement. All the three geometries were reconstructed from the images of a healthy patient (Figure 2.5a): for the aneurysmatic configuration the volume of a tract of the descending aorta was increased by 170% and the thickness was varied along the length (Figure 2.5b), while to include the graft a portion of the healthy aorta was removed and replaced with a Dacron implant (Figure 2.5c), modeled as a single layer cylindrical shell, with the properties of a linear hyperelastic material (neo-Hookean model). The walls of the vessel were also discretized with shell elements, since the thickness is significantly smaller than other dimensions. In this case, the Holzapfel-Gasser-Ogden model was adopted, considering the wall as hyperelastic and isotropic. The blood was considered a Newtonian incompressible fluid and the fluid flow was considered pulsatile, fully developed and turbulent. At the inlet and at the outlet a
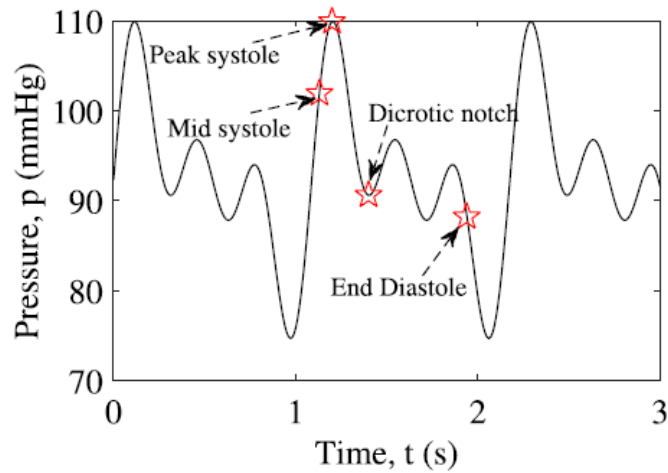
Figure 2.6: Blood flow pressure profile at the inlet [67]

time-dependent pressure condition was applied, imposing a Δp between inlet and outlet. The blood flowed out through the three upper aortic branches and the descending aorta. The pressure wave imposed as inlet BC is represented in Figure 2.6. For the outlet, the pressure magnitude was multiplied by a certain coefficient, to obtain a pressure gradient producing a blood flow velocity of 0.42 m/s. To couple the fluid and solid domain, stress and displacement continuity was imposed at the interface between the two domains. The results showed a pressure drop in the aneurysmatic area and the formation of vortexes. Considering the WSS (Figure 2.7), a decrease was observed in aneurysmatic case, which indicated that the aneurysm could further grow, while the presence of Dacron did not greatly affected the values of WSS. Lastly, the distribution of radial displacements was different in the three cases: the healthy aorta presented maximum displacements at the arch, the aneurysmatic configuration at the bulge, while in the treated configuration the Dacron experienced the maximum value (Figure 2.8). The most interesting characteristic of this study is the application of FSI analysis to assess the effect of surgical graft replacement of descending aneurysmatic aorta. However, the employment of
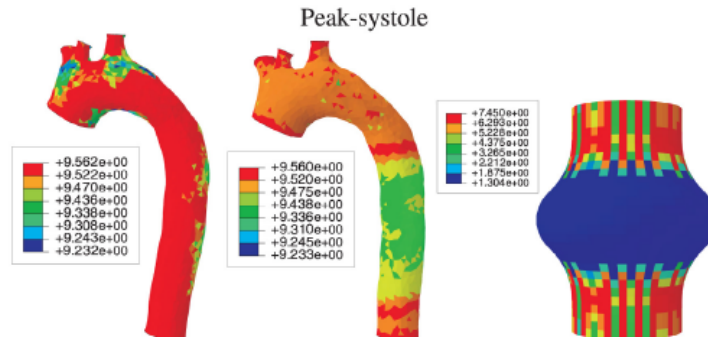
Figure 2.7: Wall shear stress contours during cardiac cycle on patient-specific aortic anatomy (left), Dacron graft (middle) and aortic aneurysm (right) [Pa] [67]
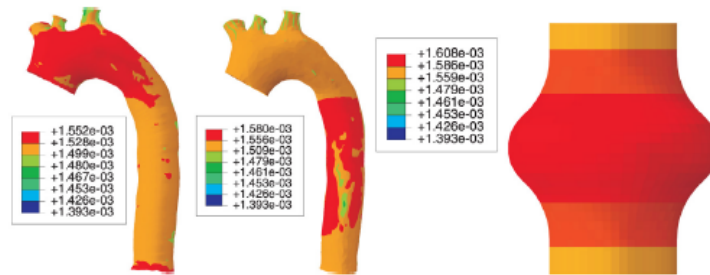
Figure 2.8: Radial displacement contours on patient-specific aortic anatomy (left), Dacron graft (middle) and aortic aneurysm (right) [m] [67]

general pressure wave as boundary conditions and the use of the geometry of a healthy patient, then modified to reproduce the pathological and treated case, constitute a great limitation. Indeed, to properly assess the consequences of this surgery, real clinical cases and a large pool of patients would be needed.

This thesis project was focused on the comparison of the pre and post-intervention hemodynamic of patients treated with graft replacement to correct ascending aortic aneurysms. To do that, SimVascular software [68] was used. This software was specifically developed to perform patient specific blood flow simulations and analysis. In 2020, De Nisco *et al* [10] used SimVascular to perform an interesting CFD analysis of hemodynamic changes due to ascending thoracic aortic aneurysm (ATAA), with particular

focus on WSSs. Two cases were considered, a healthy 36 years old subject with no history of cardiovascular disease and a 59 years old patient with BAV, moderate valve insufficiency and ATAA. The geometry of the patients was reconstructed starting from 4D flow MRI images. The final model included the ascending thoracic aorta, the aortic arch, the descending thoracic aorta and the supra-aortic vessels. Using SimVascular software, the geometry was discretized using linear tetrahedral elements. For the BCs, 4D-Flow MRI measurements were exploited. At the ascending aortic inlet section, 3D velocity data extracted along the cardiac cycle were imposed as Dirichlet inflow BCs. At the three supra-aortic branches 4D-Flow MRI measured flow rates were prescribed as outlet BCs, while at the descending aorta outlet section a three elements Windkessel model was used to model the downstream vessels. The vessel wall was considered rigid. The results of this study showed that ATAA and healthy hemodynamic were remarkably different. In particular, peculiar WSS features on the ATAA outer wall were observed, which were not or poorly present in the healthy subject. One of these features was the presence of localized marked WSS contraction regions. The role of WSSs in the mechanical and rupture properties of the ATAA is still unclear and widely debated. Some studies reported that low WSS will result in a reduction of elastic properties [69], while others associate low WSS to a decreased risk of ATAA rupture [70]. This work has two main limitations. On the one hand there is the the lack of a large pool of patients: to have reliable results, the conclusion of this study should be confirmed on a greater population. On the other there is the setting of this work, which considers the wall of the vessel as rigid.

This master thesis project takes its origin from a previous master thesis work developed by Nannini [11] in the biomechanic group at Politecnico di Milano. In this research, a comparison between the pre and post-operative fluid dynamic of a 48-year-old male patient affected by ascending aortic

aneurysm and treated with graft replacement is designed. To the best of the author's knowledge, this work constitutes the first research where this kind of comparison is realized. FSI and CFD models were developed for both pre and post-operative anatomy, starting from patient-specific geometry segmented from patient's MR angiography images. These models were co-registered to the patient's PC-MRI images, and then exported in Autodesk MeshMixer where they were smoothed and adjusted. The solid domain was obtained by extruding the wall by 2 mm in normal direction. The post-operative configuration was cut along the suture site to obtain the PET graft in the ascending segment. For the fluid mesh, a dynamic meshing was exploited. At each extremity, no displacement was allowed and a fluid-solid interface was applied as load condition at the inner surface of the solid domain. Patient-specific velocity was imposed as inlet boundary condition, while three-element Windkessel model was exploited as outlet boundary condition both at the three supra aortic branches and at the descending aorta. FSI analysis was run in ANSYS v.17.2(ANSYS Mechanical), coupling the structural solver and fluid solver (ANSYS Fluent) and ALE kinematic description was exploited. For each configuration two cardiac cycles were run on 24 cores (Intel ® Xeon ® CPU X5670 at 2.93 GHz processor for a total of 192 Gb RAM), taking $\sim$ 10 days. To compare pre and post-operative fluid dynamic, WSS, oscillatory shear index (OSI), time average wall shear stress (TAWSS) and intramural
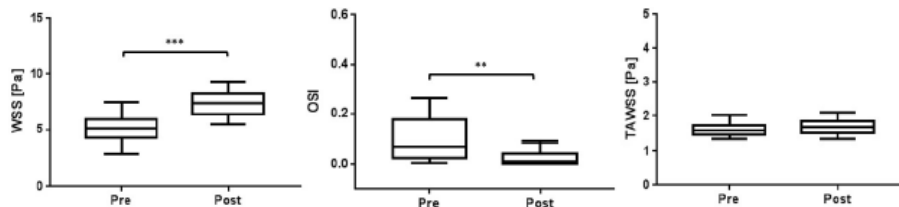
Figure 2.9: Results of t-test of WSS, OSI and TAWSS in the descending aorta obtained from FSI analysis. Asterisks indicate the p-value: * = p<0.05, ** = p<0.01, *** = p<0.001 and **** = p<0.0001 [11]
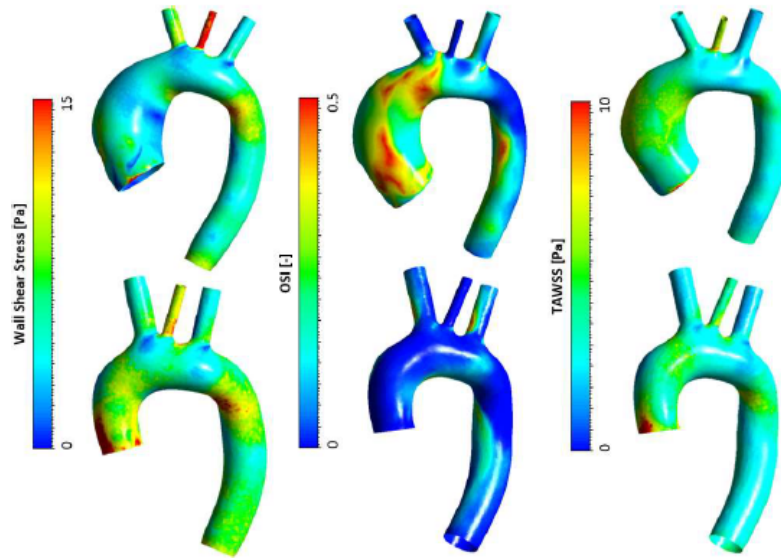
Figure 2.10: WSS, OSI and TAWSS distributions obtained from FSI analysis. Presurgical (top row) and postsurgical (bottom row) configurations. [11]

stresses were compared. Systolic peak WSS showed the maximum value in the descending aorta and in the post-intervention model they were 28% greater than in the pre-operative configuration. OSI distribution took higher values in the pre-surgical model, reaching values close to the critical threshold (0.5) in ascending aorta and in the intrados of descending aorta. Leading a t-test on WSS, OSI and TAWSS distribution in the descending aorta, significantly higher WSS and lower OSI were found in the post-operative case, while TAWSS presented no statistical difference (Figure 2.9). Important differences were found in intramural stresses: the post-surgical model presented intensification of stresses with values of ~500kPa along the suture site, due to compliance mismatch (Figure 2.10).

2.3 Aim of the thesis

FSI simulations have the great advantage to deep insight into the hemodynamic with accurate temporal and spatial resolution. To date, the

literature assessing the effect of surgical graft replacement on ascending aneurysmatic aorta with numerical approach is poor. To the best of the author's knowledge, only Nannini's work [11] is present. From this study emerges that important hemodynamic modifications are induced by graft aortic reconstruction, particularly in the descending aorta, which may lead to atherogenic process and, as a consequence, to possible dissections. Among the main limitations of this work, long computational times and a small population (only one subject) were reported.

From these considerations takes its origin this work that has as main objective the enlargement of patients pool, to have a more complete insight into fluid dynamic modification induced by surgical graft replacement, with particular focus on the descending aorta. Patients who underwent ascending aortic reconstruction with PET graft are considered, studying and comparing for each of them the pre and post-operative configuration. At this purpose, a new methodology is used to solve the FSI problem, exploiting the CMM-FSI formulation presented in Section 2.1.2, which allows to reduce the computational time. This is fundamental in clinical applications, that need accurate results in the shortest time possible.

Chapter 3

Materials and Methods

In this chapter the workflow adopted for the setting of the FSI simulations is reported. This workflow was exploited for both the pre and the post-surgical configuration of each patient. First of all, the description of patient-specific geometry reconstruction and meshing is reported, followed by the description of the process adopted to impose boundary conditions and material properties. Finally, the operation performed to compare simulation results with 4D-Flow data and the description of the quantities extracted from results dataset are illustrated.

3.1   Introduction

To analyze the effect of surgical PET (i.e. Dacron) graft replacement, five non-BAV patients were studied. This allowed having a good insight into the effect of this treatment on a wide range of subjects, all suffering from ascending aortic aneurysm, with no other comorbidities.

		Cardiac Cycle Period [s]	Pressure [mmHg] Systole	Diastole	Age	Genre
Patient1	Pre-op	0.948	132	85	48	M
	Post-op	0.828	127	82		
Patient2	Pre-op	0.839	158	96	61	M
	Post-op	0.838	140	89		
Patient3	Pre-op	0.750	153	78	71	M
	Post-op	0.900	176	108		
Patient4	Pre-op	0.952	109	77	53	M
	Post-op	0.720	113	72		
Patient5	Pre-op	0.901	141	79	72	M
	Post-op	1.148	126	65		

Table 3.1: Patients characteristics

The absence of other pathologies allowed to perform a valve-sparing reconstruction (VSR) operation. All the patients were treated at New York-Presbyterian Hospital (New York, NY). Analyzing patients with the same pathology allows to better compare the outcomes of the treatment. Furthermore, the VSR technique enables to study the hemodynamic alterations caused only by the graft, not taking into account other factors like prosthetic valves effects, present if the valve replacement had also taken place. The post-intervention images were acquired 6 months after the surgery. For each pre and post-operative configuration, five cardiac cycles were simulated, three with the rigid wall condition (CFD) and two with the deformable wall condition (FSI). In Figure 3.1, the workflow that has been followed for each patient is reported and will be better specified in the following sections.
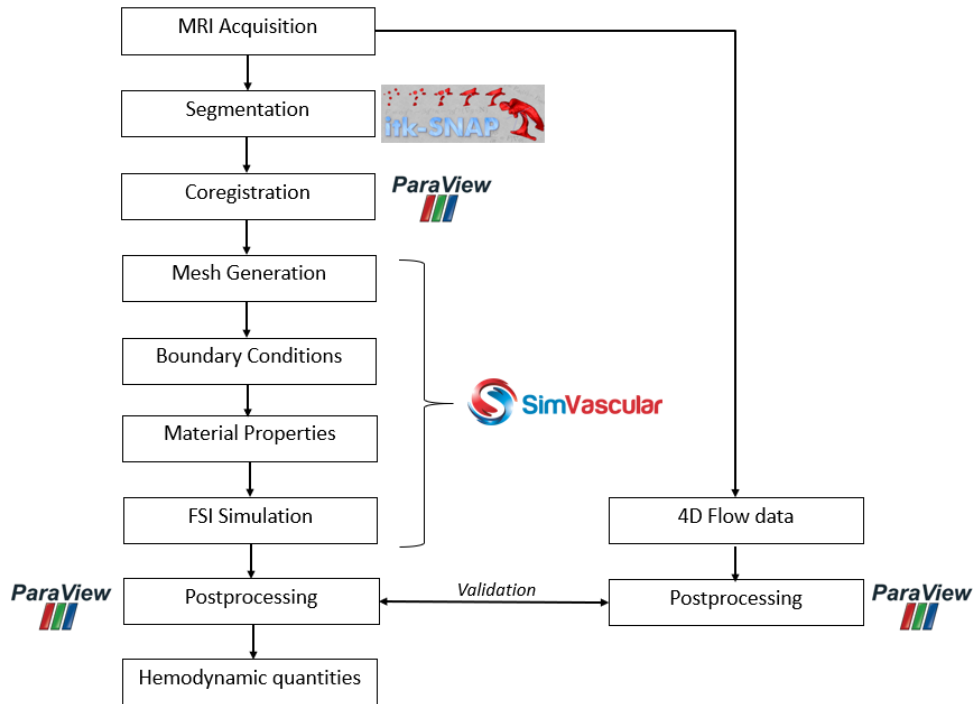
Figure 3.1: Workflow followed for each patient

3.2 Model reconstruction

The pre and post-intervention anatomy of each patient were reconstructed using the software ITK-SNAP 3.8 [13], starting from MRA images. MR images were prospectively acquired pre and post-operatively on a 3T GE SIGNA ™ scanner (General Electric Co., Boston, MA,USA). The protocol was the same for both acquisitions. To better assess the anatomy of the vessel, a contrast-enhanced MR angiography was performed. Patient's MRA images were segmented using the Active Contour Segmentation Mode tool provided by the ITK SNAP software. The automatic segmentation was then manually adjusted to be sure to capture the correct geometry of the vessel, being careful to not underestimate the aortic lumen. In this phase the whole aortic root and the whole descending tract were reconstructed. The outcomes of this operation for a generic patient are reported in Figure 3.2. The rough
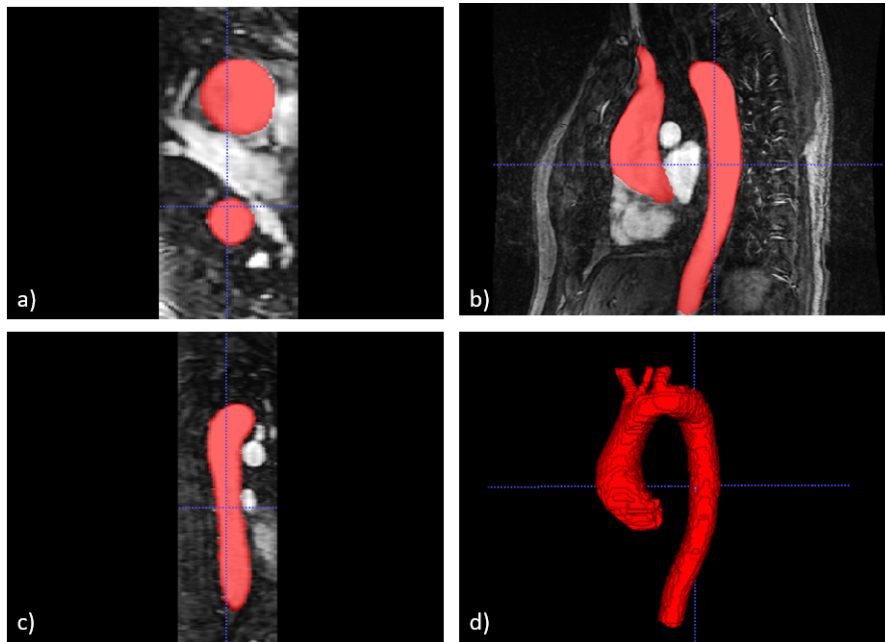
Figure 3.2: Aorta segmentation a) Transverse plane b) Sagittal plane plane c) Coronal plane d) Reconstructed geometry

model obtained (Figure 3.2 d) was then saved as an STL file and exported in Meshmixer (Autodesk Inc., San Rafael, CA, USA), where a shape-preserving smoothing filter was applied, regulating the smoothing scale and constraint rings parameters in order to obtain a more regular outer surface. After remeshing the model, the three supra-aortic vessels were cut at the basis and extruded by 20 mm in the normal direction, to reduce the effect of outlet boundary conditions on the fluid dynamic of the vessel. Then the model was cut at the level of the sinotubular junction (STJ), isolating the inlet. Finally, a distal portion of the descending aorta was removed to obtain a plane outlet surface. In Figure 3.3 the results of the operations performed on the reconstructed model are reported.

For the post-operative configuration, the properties of the model were modified to impose different material characteristics to the portion of the vessel wall substituted by the graft. To do that, an in-house Python code developed
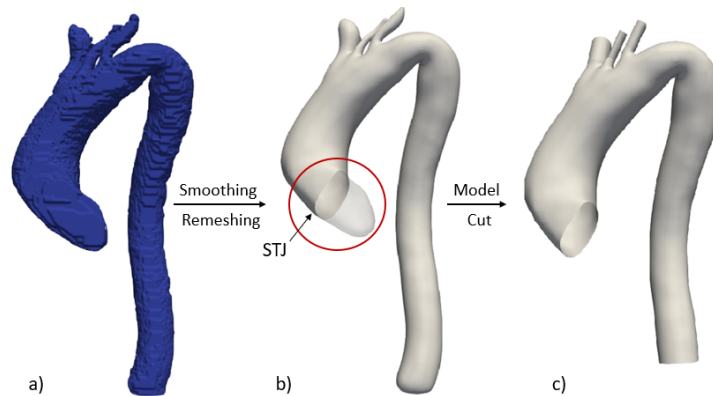
Figure 3.3: a) Segmented model b) Smoothed model cut at the sinotubular junction c) Final geometry

during this master thesis work was exploited, which modified the ModelFaceID property of the vtp files created by SimVascular. ModelFaceID is the property used by the software to differentiate the various portions of the model, allowing to assign boundary conditions and variable material characteristics. *Vtp* files instead are defined as Unstructured Polydata. PolyData files are files containing a set of points and cells. In this case they are unstructured, i.e. they form a topologically irregular set of points and cells. To each of them different properties can be associated (e.g. velocity, pressure, displacements, etc.). Using Paraview, a clip of the model was created to isolate the region in
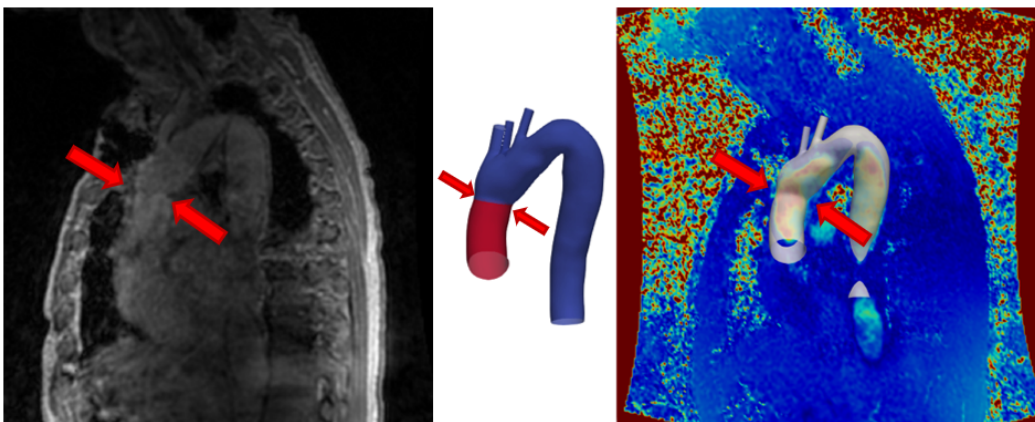
Figure 3.4: Representation of the graft in the post-surgical model

47

which the ModelFaceID needed to be modified. Giving as input to the Python code both the clipped region and the whole model, a new vtp file containing the whole model was created, with differentiated ModelFaceID property in the clipped region. To identify the region to be clipped, the post-intervention patient's images were observed to identify the region of the vessel substituted by the graft, as showed in Figure 3.4. In the center of this image the model with the modified ModelFaceID is reported.

3.3 Simulation Setting

The model of the whole aorta was then imported in SimVascular, where all the simulation parameters were set. The basic parameters are reported in Table 3.2.

Basic Parameters	
Fluid density $[g * mm^{-3}]$	0.00106
Fluid viscosity $[g * mm^{-1} * s^{-1}]$	0.004

Table 3.2: Blood properties

SimVascular solver is dimensionless. For this reason, it was fundamental to set coherent units of measurement for all the parameters. Since all the models were in mm, the units of measurement were set in MGS system. The initial pressure of the fluid domain was set for each patient based on clinical data. It was measured $\sim$ 30 minutes prior to each MRI acquisition using SphygmoCor CP system (AtCor Medial, Sydney, Australia) in a non-invasive way. This system is based on radial applanation tonometry and it is the most common device used for non-invasive central blood pressure measurements.

In the following sections all the parameters set for the simulation will be discussed in detail (i.e. mesh generation, BCs, wall properties and solver parameters).

3.3.1 Mesh Generation

The mesh has been created using the mesh generator available in SimVascular. The fluid domain was discretized with tetrahedral elements and the characteristic dimension was chosen according the results of a mesh sensitivity analysis.

Mesh sensitivity analysis

This analysis was led based on Roache's study [71]. According to this work, three meshes were considered, a fine ($N_1 \sim 6.9mln$ of elements, characteristic dimension $0.87mm$), a medium ($N_2 \sim 4.9mln$ of elements, characteristic dimension $1mm$) and a coarse one ($N_3 \sim 3.4mln$ of elements,characteristic dimension $1.1mm$) (Figure 3.5). For each mesh, a simulation with the
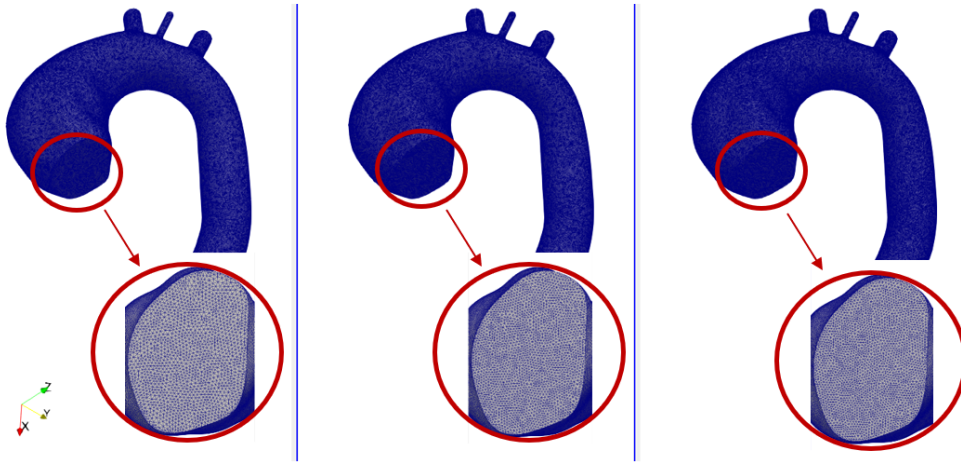
Figure 3.5: Meshes used for the mesh sensitivity analysis. Starting from the left, the coarse, the medium and the fine meshes are reported sequentially.

boundary conditions reported in the following sections was led and the 95th percentile of the velocity on a transverse plane of the descending aorta was taken as parameter of grid convergence (f_i). The grid convergence index (GCI), as defined by Roache [71], was calculated for the fine-to-medium and medium-to-coarse mesh. This parameter is a measure of the fractional error,

so it gives a quantitative estimation of how f_i would change with a finer mesh. The number of elements for each mesh was chosen according to the following condition:

$$r \approx \left(\frac{N_1}{N_2}\right)^{\frac{1}{3}} \approx \left(\frac{N_2}{N_3}\right)^{\frac{1}{3}} \tag{3.1}$$

According to Roach [72], the minimum acceptable value for this parameter is 1.1. The $GCIs$ were calculated as:

$$p = \frac{ln\left(\frac{f_3 - f_2}{f_2 - f_1}\right)}{ln(r)} \tag{3.2}$$

$$E_1 = \frac{f_2 - f_1}{f_1(r^p - 1)}, \qquad E_2 = \frac{f_2 - f_2}{f_2(r^p - 1)} \tag{3.3}$$

$$GCI_{1,2} = F_s \cdot |E_1|, \qquad GCI_{2,3} = F_s \cdot |E_2| \tag{3.4}$$

According to Roache's suggestion [72] and to Craven's work [71], a factor of safety F_s of 1.25 was applied. Finally, the parameter k was computed. This parameter is defined as:

$$k = \frac{1}{r^p} \cdot \frac{GCI_{2,3}}{GCI_{1,2}} \tag{3.5}$$

To ensure that the meshes are in the asymptotic range of convergence, k must be close to 1 [73].

Mesh Quality

Besides choosing the correct characteristic dimension of the mesh, it is also fundamental to have a good mesh quality to obtain stable and reliable results. Using Mesh Quality filter available in Paraview, the meshes generated by SimVascular were checked evaluating the *edge ratio* and the *radius ratio*. These quantities, as calculated by Paraview's filter, are defined in *The Verdict Library Reference Manual* [74].

For tetrahedral elements, the *edge ratio* can be calculated as:

$$edge\ ratio = \frac{L_{max}}{L_{min}} \tag{3.6}$$

where L_{max} and L_{min} are respectively the largest and the smallest edge length of each element. The ideal range is between 1 and 3.

The *radius ratio q* is the normalized ratio of the radius of the inscribed sphere to the radius of the circumsphere:

$$q = \frac{R}{3r} \tag{3.7}$$

Also for this parameter the ideal range lies between 1 and 3.

3.3.2 Boundary conditions

Once the mesh was generated, inlet and outlet boundary conditions (Figure 3.6) were imposed.
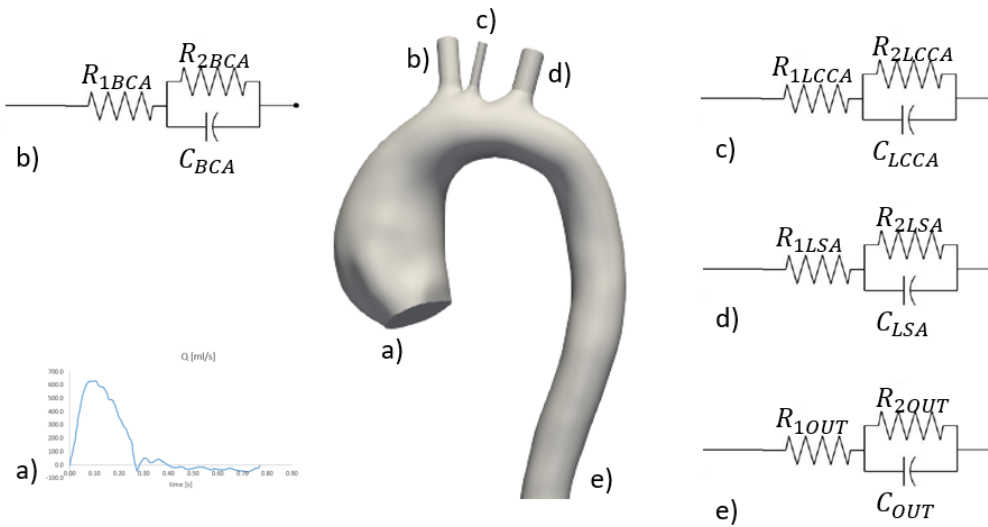
Figure 3.6: Inlet and outlet BCs of the model

Outlet Boundary conditions

The outlet boundary conditions were set exploiting three-element Windkessel model , which represents the vessels downstream to the outlets as a proximal resistance R_1, a compliance C and a distal resistance R_2 (Figure 3.6 b-e). To calculate RCR values at each outlet, the works provided by Pirola [26] were exploited. According to these studies, the total resistance R_t, given by $R_t = R_1 + R_2$, was calculated as:

$$R_t = \frac{\bar{P}}{\bar{Q}} \qquad (3.8)$$

where $\bar{P}$ was the mean pressure and $\bar{Q}$ was the mean flow rate through each outlet. $\bar{P}$ data were available for each subject, while $\bar{Q}$ values were calculated exploiting patient-specific 4D-Flow data for each outlet. However, it was not possible to obtain reliable results calculating $\bar{Q}$ through the 4D-Flow section of these vessel, because flow rate measurement varied a lot based on the section considered, especially at the supra-aortic branches. To overcome this issue, the mean flow rate overtime at the inlet and at the outlet was calculated using Paraview and the difference between these two flows was divided based on the area of the three supra-aortic branches, finding $\bar{Q}$ through each vessel. Since also along the descending aorta 4D-Flow data can be affected by noise, the
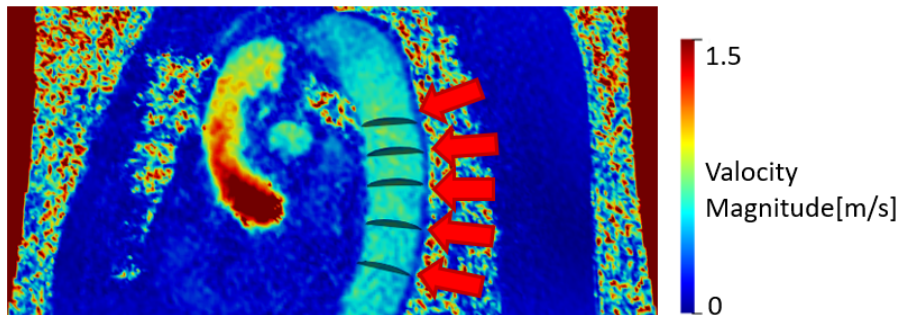
Figure 3.7: Descending aorta planes for outlet flow calculation

outlet flow rate was computed as the mean of the flow rate calculated on five different planes along the descending aorta (Figure 3.7).

To calculate $\bar{Q}$ from 4D-Flow data, the following expression was used:

$$\bar{Q} = \iint_{Area} v \cdot dA \tag{3.9}$$

where v and A were respectively the blood velocity and area of the considered 4D-Flow section. R_1 was then obtained as:

$$R_1 = \frac{\rho c}{A} \tag{3.10}$$

where ρ was the blood density, A the area of the vessel and c the pulse wave velocity calculated as:

$$c = \frac{a_2}{2r^{b_2}} \tag{3.11}$$

where $a_2 = 13.3$, $b_2 = 0.3$ and r was the radius of the considered vessel, expressed in mm. R_2 was calculated as the difference between R_t and R_1. Finally the compliance was determined as:

$$C = \frac{\tau}{R_t} \tag{3.12}$$

where τ was the time-constant of the exponential pressure-fall during diastole, usually set to be equal to 1.79 s.

Since for each outlet both the flow rate and the mean pressure were available, this procedure was applied to all the outlets. The values found for all the patients are reported in Tables A.1-A.5 in Appendix A.

Inlet boundary condition

At the inlet, patient-specific flow rate was used as boundary condition, imposing patient's specific velocities extracted from 4D-Flow data. Using
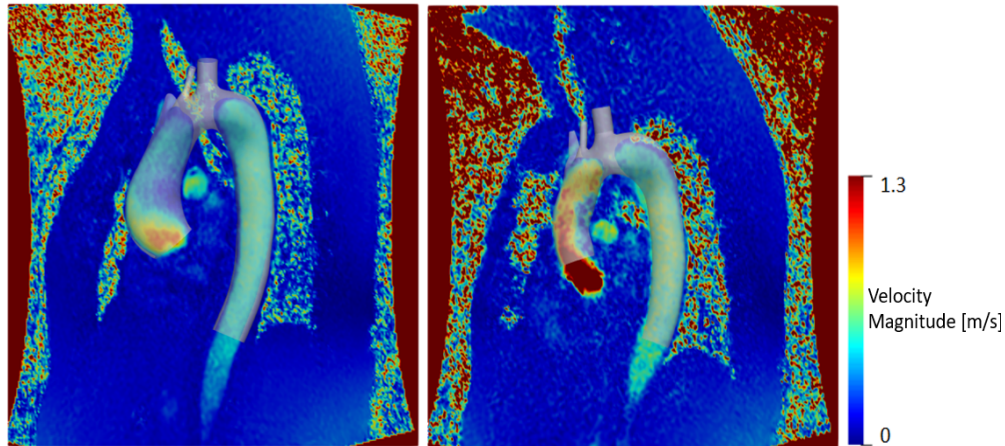
Figure 3.8: Pre (left) and post-operative (right) geometry co-registration on PC-MRA data

a sagittal-oblique orientation, a respiratory compensated 4D-Flow phase contrast acquisition was performed for each patient, with VENC=200cm/s. These images were elaborated with an in-house Python code developed by our research group, to extract from the 4D-Flow data set a PC-MRA. The smoothed model obtained in MeshMixer was exported as an STL file and imported in Paraview, where a manual co-registration was performed: using Paraview's Transform tool, the model was positioned on PC-MRA image, carefully overlapping the model with the representation of the aorta on PC-MRA data (Figure 3.8). By means of another Python software developed by our research group, exploiting the inlet model co-registered on PC-MRA images and the PC-MRA images themselves, the velocities at the inlet were extracted from 4D-Flow data as comma-separated-values (csv) files, one for each frame of the 4D-Flow data set. Each .csv file contained the three components of the velocity for each point of the model's mesh (Figure 3.10). For the success of this operation, the key aspect was the precise co-registration. These velocity data were then mapped on the inlet mesh generated by SimVascular. To do that, the coordinates and the node ID assigned by the software to each point of the mesh were necessary. All this information was
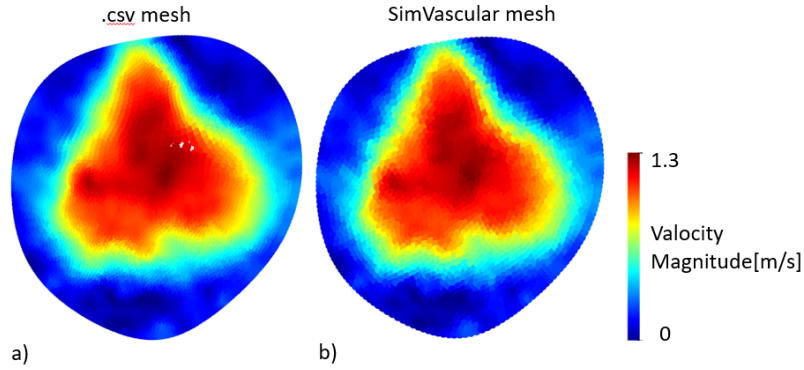
Figure 3.9: Velocity profile contour at systolic peak extracted from .csv files (a) and reported on SimVascular mesh (b)
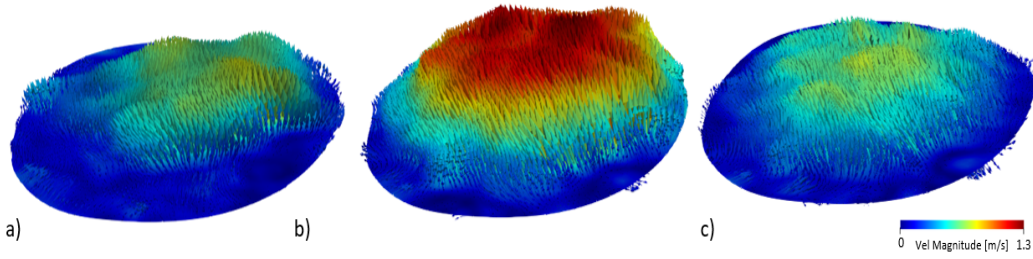
Figure 3.10: Representation of inlet velocity vectors extracted from 4D-Flow data at different cardiac cycle phases (a)early systole b)systolic peak c)late systole)

found in the *bct.dat* file, which is a file automatically generated by SimVascular. Besides the coordinates and the node IDs, this file contains for each point of the mesh and for each time instant the three velocity components. Through an in house Matlab software developed during this master thesis work, to each point of SimVascular mesh the three velocity components of the closest point of the mesh defined in the .csv files were assigned (Figure 3.9) Then, based on the simulation time interval and on the patient's cardiac cycle period, the number of time steps was decided. A 6th order Fourier fitting was performed to obtain the set of velocities for each point of the mesh and for each time step (Figure 3.11). In the end, a new *bct.dat* file was written and imported in SimVascular, to impose patient's velocities at the inlet. In this phase, the
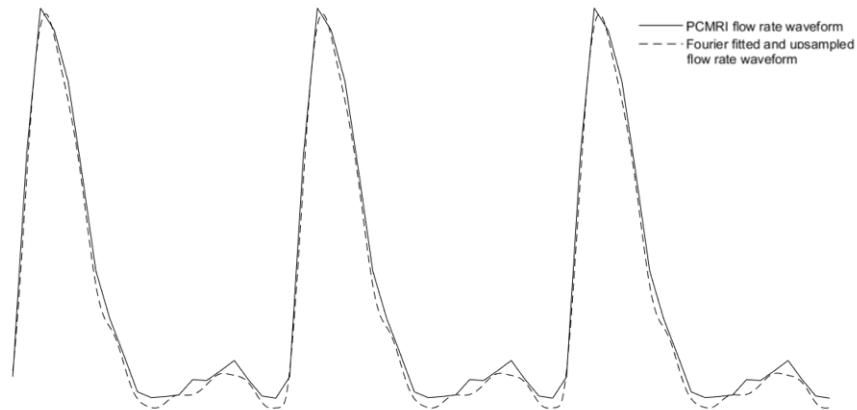
Figure 3.11: Flow rate inlet waveform for three cardiac cycles before and after Fourier fitting

zero velocity condition was enforced to the nodes on the edge of the inlet: this condition was required to perform deformable walls simulations and was applied recognizing the nodes on the edge through their global node ID.

3.3.3 Wall properties

Of the total five cardiac cycles simulated for each patient's pre and post-surgical configuration, three were performed with rigid wall condition. This was fundamental to set the initial condition for the deformable wall simulations. Indeed, SimVascular software guidelines report that the most robust way to lead an FSI analysis is to first simulate a rigid wall case with the same BCs. The results of the final step of this CFD simulation were imposed as initial condition of the respective deformable wall case. Wall properties for both the pre and post-operative case are reported in Table 3.3.

The value of the thickness of the aorta was chosen based on literature [14, 15]: since the thickness of the aorta is not constant and especially in aTAAs can vary up to 0.7 mm, a medium value of 2 mm was adopted. The Young Modulus of the aorta and the density were set based on Khamdaeng *et al* work [16], while for the graft properties Tasca *et al* work was exploited [17].

	Vessel wall	Graft
Thickness $[mm]$	$2^{[14, 15]}$	$0.305^{[17]}$
Elastic Modulus $[MPa]$	$1.5^{[16]}$	$11.84^{[17]}$
Poisson ratio	$0.5^{[12]}$	$0.5^{[12]}$
Shear constant	$0.83^{[12]}$	$0.83^{[12]}$
Density $[g * mm^{-3}]$	$0.00112^{[16]}$	$0.00112^{[16]}$

Table 3.3: Deformable wall properties

The Poisson ratio and the shear constant were chosen to respect the thin wall membrane assumption made by Simvascular software to model the vessel wall [12].

3.3.4 Solver Parameters

Figueroa in his work [12] summarizes the steps involved in the time integration/linearization algorithm used by SimVascular solver, which are reported in Figure 3.12. Here, n represent the number of time steps, (i) the nonlinear iteration counter, a, b the local node numbers and i, j the spatial dimensions. In each time step, a nonlinear iteration loop is performed to obtain the solution at time t_n to the non-linear system defining the problem,
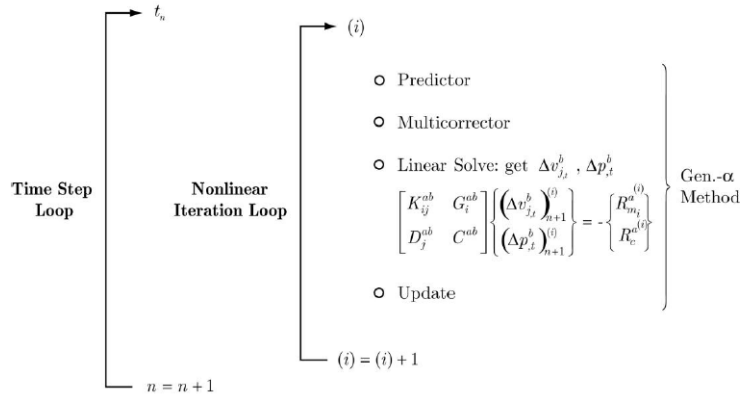
Figure 3.12: Time stepping and nonlinear iteration loops in the solution strategy

using a Newton Rapson strategy. The linearization produces a linear system like the one showed in Figure 3.12, where two variables are present: one vector (v) and one scalar (p). Thanks to this theoretical background, it was possible to understand the role of the different parameters requested by SimVascular solver.

The time step for both the rigid and deformable wall case was 1 ms and the results were saved every 10 ms. The step construction parameter controls the non-linear iteration loop within each time step. SimVascular guidelines reports a minimum value of 3 and 10 for respectively rigid and deformable wall pulsatile problems. With this value, the convergence of the solution was not reached for the rigid wall case and for this reason a value of 7 was chosen, which provided a good convergence. The solver type and maximum number of iterations for svLS (the solver implemented in SimVascular) were set based on the guidelines established by the software developers. Finally the residual criteria and the tolerances had to be imposed. The former refer to the solution of the non-linear system, while the latter to the solution of the linearized system. Values of respectively 0.001 and 0.0001 were chosen for these two parameters. All these parameters are summarized in Table 3.4.

	Rigid Wall	Deformable Wall
Time Step [s]	0.001	0.001
Step Contrsuction	7	10
Solver Type	NS	GMRES
Residual Criteria	0.001	0.001
Tolerance on Momentum Equations	0.0001	0.0001
Tolerance on ontinuity Equations	0.0001	0.0001
Tolerance on svLS NS Solver	0.0001	0.0001
Max nr Iterations for svLS NS Solver	1	10
Max nr Iterations for svLS Momentum	2	20
Max nr Iterations for svLS NS Continuity	400	400

Table 3.4: Solver parameters

3.4 Post-processing

The post-processing was focused on two principal aspects: the comparison of velocity-related quantities with 4D-Flow data and the computation of some significant parameters. The former ensure to have reliable results, while the latter provide useful quantitiess to assess fluid dynamic changes induced by graft implantation.

3.4.1 Evaluation of the model

For each patient and for each pre and post-surgical configuration, four planes of interest were considered, one in the ascending aorta (AO), one in the arch (ARCH), one in the central part of the descending aorta (Desc-Mid) and one in the final part of the vessel (Desc-Dist). The comparison was both qualitative and quantitative and the considered planes, besides the inlet plane, are shown in Figure 3.13.

To visualize the differences and the similarities between simulation results and 4D-Flow data, streamlines and velocity magnitude contours were created.
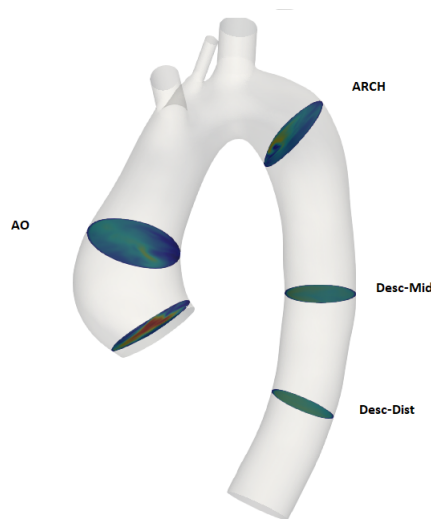
Figure 3.13: Planes considered for the validation

4D-Flow streamlines were extracted applying the Streamtracer filter available in Paraview to the velocity values inside the model domain. This set of velocities was created using an in-house Python software. Then, for each plane represented in Figure 3.13, a velocity magnitude contour was displayed for both the FSI and the 4D-Flow data sets, to visually compare the two different methodologies. Finally, the blood flow rate at the outlet of the model was compared with the outlet flow rate extracted from a corresponding plane of 4D Flow images.

Regarding the quantitative comparison, the relative root mean square error (RRMSE) was computed [75]. The RMSE was obtained as:

$$RMSE = \sqrt{\frac{\sum_{i=1}^{n}(v\_mag_{4DF_i} - v\_mag_{FSI_i})^2}{n}} \qquad (3.13)$$

where $v\_mag_{4DF_i}$ and $v\_mag_{FSI_i}$ represent the velocity magnitude of the ith point of the 4D-Flow and FSI data respectively. Since the simulation mesh was finer than the 4D-Flow data mesh, the simulation mesh was downsampled and the simulation's velocity data were probed with an in-house Matlab code. RRMSE was computed normalizing the value of the RMSE (Equation 3.13) with the maximum velocity computed from the 4D-Flow data ($v_{max_{4DF}}$):

$$RRMSE = \frac{RMSE}{v_{max_{4DF}}} \qquad (3.14)$$

3.4.2 Parameters of interest

As already pointed out, the great advantage of FSI modeling is the possibility to extract quantities which cannot be assessed *in vivo*.

One of the most interesting parameters are the *wall shear stresses (WSSs)*. WSSs are defined as the stresses tangent to the walls, due to the blood flowing

in the aorta. They are calculated as:

$$\tau = \mu \frac{\partial \vec{v}}{\partial \vec{n}}\bigg|_{wall} \tag{3.15}$$

Too low WSSs (<0.4 MPa) lead to aneurysm growth and to the consequent weakening of the wall, which may result in rupture [76].

Another interesting parameter is the *oscillatory shear index (OSI)*. This is a measure of the influence of the oscillatory component of WSSs. It is defined as:

$$OSI = \frac{1}{2}\left(1 - \frac{|\int_0^T W\vec{S}Sdt|}{\int_0^T |W\vec{S}S|dt}\right) \tag{3.16}$$

This index is $0 \leq OSI \leq 0.5$. Values close to 0.5 enhance atherogenic process [19].

Finally, the *strains* can be assessed. This quantity is not automatically computed by SimVascular, but can provide important information on how the wall deformation changes between pre and post-intervention configurations. An in house Matlab code, able to calculate the strain starting from the displacements provided as output variable by the solver, was therefore developed. The walls of the vessel, given the thin membrane assumption, were meshed using triangular elements. The strains were calculated element-wise and for each element a local reference system was defined. The direction of the centerline was exploited to define consistent reference systems between the elements: for each element a right-handed reference system was build, with a normal vector pointing toward the inner part of the model, an axial vector directed as the centerline and a circumferential vector calculated according to right-handed reference system (Figure 3.14). The displacements in the global reference system were projected in the local reference system (e.g. on the element plane). After calculating element's Jacobian matrix, the displacement gradient (∇u) was calculated. The deformable gradient tensor

61
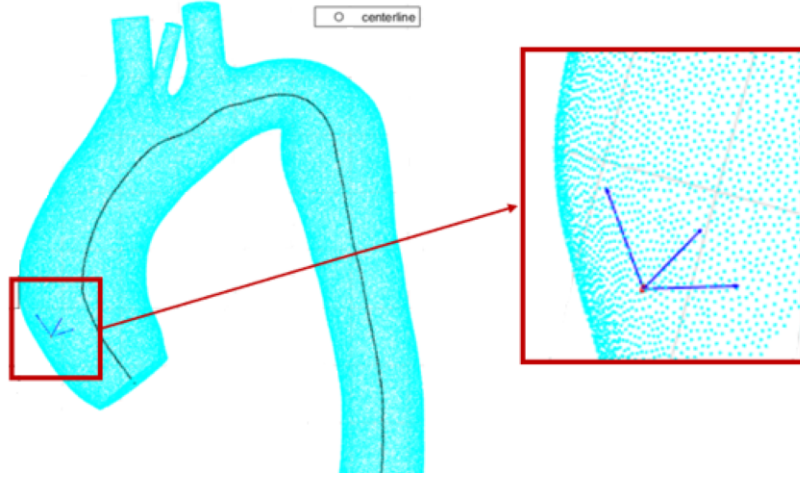
Figure 3.14: Representation of the local reference system for a specific element

(F) was obtained as:

$$F = \nabla u + I \tag{3.17}$$

where I is the identity matrix. The Green strain tensor (E) was calculated for each element and for each time instant, with the following formula:

$$E = \frac{1}{2}(F^T * F - I) \tag{3.18}$$

The maximum principal strain was used in this work, which was calculated as the maximum eigenvalue of E tensor.

The code was validated using Abaqus suite. The surface mesh generated in SimVascular was imported in the software, considering the cells as membrane elements. To each node of the non-deformed configuration, the corresponding systolic displacement calculated by SimVascular solver was applied.

Abaqus strains presented a mean and a median value of respectively 0.06282 and 0.06325, while the Matlab code of 0.06345 and 0.06369, resulting in differences of respectively the 1% and 0.37%.

Two statistical analysis were performed to compare Abaqus strains (ε_{Abaqus})

with the ones obtained through the Matlab code (ε_{Matlab}): Bland Altamann and linear regression methods.

Figure 3.15 reports the results of Bland Atlmann analysis. The x axis represents the average of the two measurements, while the y axis the percentage difference, calculated as:

$$\%Difference = 100 * \frac{\varepsilon_{Abaqus} - \varepsilon_{Matlab}}{\frac{\varepsilon_{Abaqus} + \varepsilon_{Matlab}}{2}} \tag{3.19}$$

The central dotted line shows the average bias (i.e. the average of the differences), which in this case assume a value of -0.71905%. The superior and inferior red lines display the 95% limits of agreement (respectively 3.988% and -5.426%), which are computed as the bias plus or minus 1.96 times its standard deviation. The low bias and the narrow limits of agreement assess a really good accordance between the two dataset.

The results of the linear regression analysis are reported in Figure 3.16. Linear regression finds the best line that predicts y values (in this case Matlab strains) from x ones (Abaqus strains). As it can observed in Figure 3.16, the data can
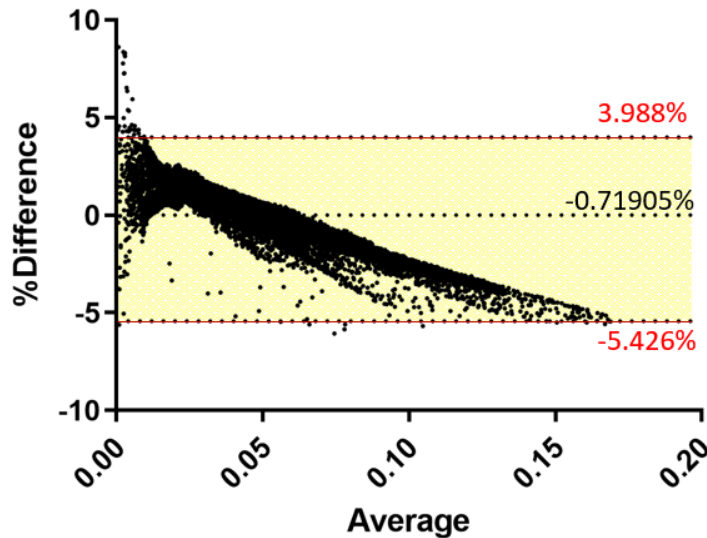
Figure 3.15: Bland Altmann analysis
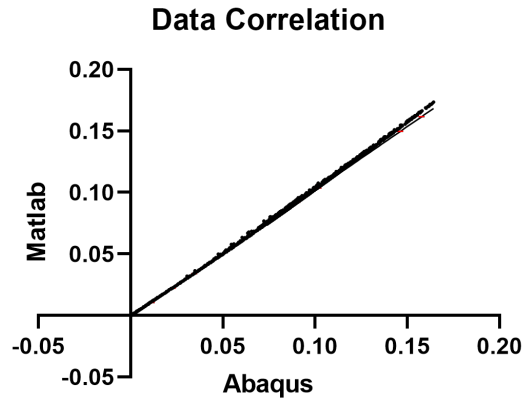
Figure 3.16: Linear Regression Analysis

be almost perfectly fitted by a line. Indeed, the slope is 1.033 and the coefficient of determination R^2 assume a value of 0.9994. R^2 is a measure of the goodness of the fit and when it is equal to 1 it indicates a perfect fit.

Since both the methodologies show a really good agreement between the two dataset, the Matlab code developed in this thesis work can be considered validated against Abaqus data and will be therefore used to extract the strains, starting from nodal displacements. The differences observed between the two dataset are due to the centerline adopted for the local reference system definition in Matlab subroutine. Indeed the centerline does not account for the supra-aortic branches, which were not the focus of this study. This approximation leads to small variation in strain calculation for the elements located at the supra-aortic branches.

All the quantities reported in this section will be computed for each patient's pre and post-operative case. The comparison of these measurements between the two configurations will be reported in Chapter 4 and, thanks to the various patients considered, will provide an usefull insight into fluid dynamic changes induced by surgical graft replacement of ascending aneurysmatic aorta.

Chapter 4

Results

In this chapter the results of the patient-specific FSI simulations developed in this master thesis work will be reported. In the first part, the outcomes of mesh sensitivity analysis are displayed. Then, the results obtained from the FSI simulation will be compared with 4D-Flow data set to evaluate the accuracy of the model. Simulation's results will be then compared with the outcomes obtained in a previous work. In the last part of this chapter the hemodynamic and biomechanical parameters extracted from the simulation results will be discussed.

4.1 Mesh sensitivity

The mesh sensitivity analysis was performed according to the criteria reported in Section 3.3.1. The values of the parameter of grid convergence f_i (95th percentile of the velocity) are displayed in Table 4.1 for each mesh.

	Fine Mesh	Medium Mesh	Coarse Mesh
95th velocity percentile	677.78	681.23	691.012

Table 4.1: Parameter of grid convergence

In Figure 4.1 the transverse planes used to calculate f_i are represented (one for each mesh), with the corresponding velocity contour. According to the figure, the velocity distribution was the same for all the three cases. This was confirmed also by the variation of f_i, which was 1.4% and 0.5% for respectively the coarse-to-medium and medium-to-fine meshes. In Table 4.2 the results of the mesh sensitivity analysis are reported.

	r	GCI[%]	k
Fine-to-Medium	1.123	0.348	0.995
Medium-to-Coarse	1.125	0.980	

Table 4.2: Mesh sensitivity analysis results
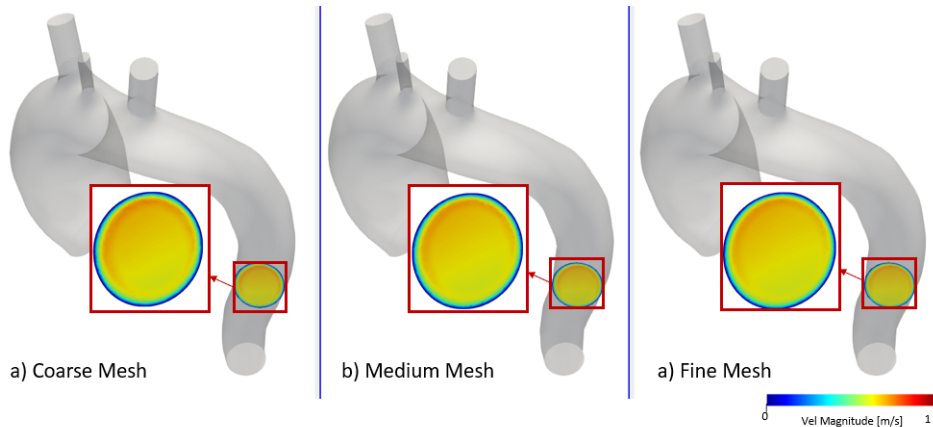
Figure 4.1: Transverse section used for mesh sensitivity analysis

66

Mesh		No. of elements	No. of nodes	Characteristic Dimension [mm]	Type
Patient1	Pre-op	7155019	1157264	1	Tet
	Post-op	5394501	878768		
Patient2	Pre-op	5155976	839333	1	Tet
	Post-op	5528997	901227		
Patient3	Pre-op	5170483	842669	1	Tet
	Post-op	4745582	774359		
Patient4	Pre-op	6247623	1018982	1	Tet
	Post-op	4152126	680575		
Patient5	Pre-op	6146626	1003980	1	Tet
	Post-op	3807829	622997		

Table 4.3: Mesh characteristics

GCI values $< 1\%$ [71], and k values close to 1 [72] ensured that the meshes were in the asymptotic range of convergence. Since the lowest GCI value was found in the fine-to-medium analysis and since for the medium-to-coarse mesh the GCI was close to the critical value, the medium mesh was adopted for the simulations and the characteristic dimension of 1mm was chosen to discretize the pre and post-operative geometries of all the patients. The characteristics of the pre and post-intervention meshes of each patient are reported in Table 4.3.

Regarding the quality of the mesh, the distribution of edge length and radius
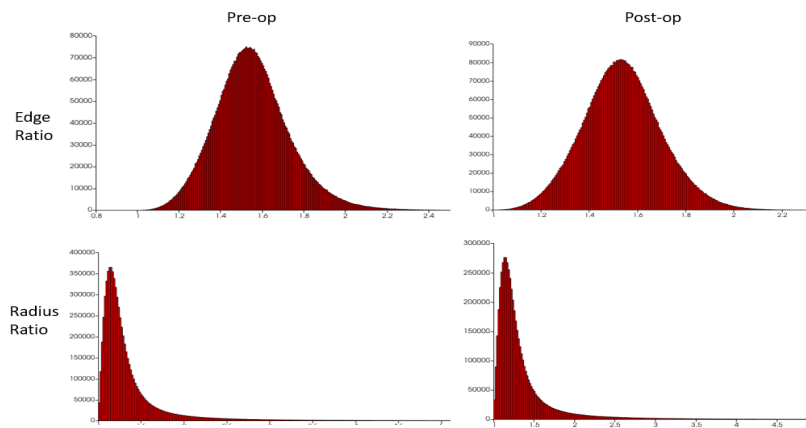
Figure 4.2: Distribution of mesh quality metrics

67

ratio is reported in Figure 4.2 for the first patient as an exemplary case. This distribution was the same for all the geometries, as it can be observed from Figures B.1 reported in Appendix B.

4.2 Comparison with 4D-Flow data

All the pre and post-surgical models have been compared with 4D Flow data, as reported in Section 3.4.1. The results of the qualitative evaluation are represented in Figure 4.4-4.7, where both the pre and post-surgical colormaps, streamlines and outlet flow rates are reported. The velocity distribution between simulation results and 4D-Flow data were comparable. The colormaps showed that the location of the velocity peak was usually well estimated in both the pre and post-intervention configuration. In general, a velocity overestimation was found in the ascending aortic plane (Ao): as reported in Table 4.4, velocity values estimated by the FSI analysis were always higher than the 4D-Flow ones. However, as confirmed by RRMSE analysis reported later in this section, these overestimations were not significant.

	FSI Median $[10^{th} \div 90^{th}]$[mm/s]	4D-Flow Median$[10^{th} \div 90^{th}]$[mm/s]
Patient 1	296.0[204.7 ÷ 386.2]	289.4 [126.9 ÷ 444.0]
Patient 2	428.6 [326.2 ÷ 476.2]	279.3 [116.9 ÷ 397.1]
Patient 3	529.9 [202.6 ÷ 1356.3]	455.7 [173.8 ÷ 924.6]
Patient 4	405.3 [171.6 ÷ 529.3]	251.6[92.9 ÷ 404.3]
Patient 5	263.2 93.8 ÷ 320.6]	164.7 [76.0 ÷ 273.6]

Table 4.4: Median and 95th percentile of the velocity in the descending aorta

Observing the pre-surgical streamlines, at the intrados of ascending aorta a vortical velocity pattern was observed in all the analyzed cases, while in the descending aorta the blood flow was less disturbed, as demonstrated by the straight streamlines trend. The same neat pattern was observed in both ascending and descending aorta of the post-intervention configuration.
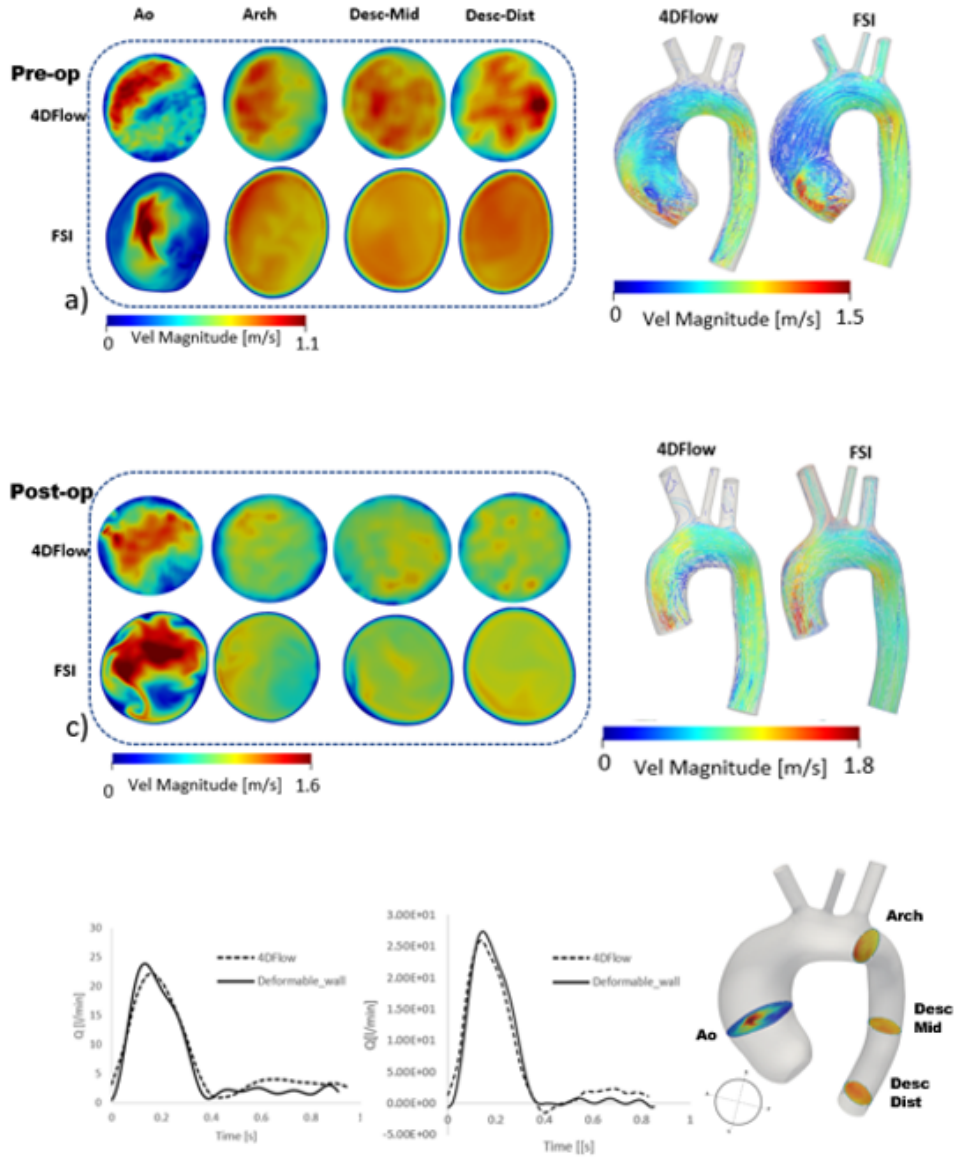
Figure 4.3: **Patient 1.** a) Pre-surgical 4D-flow and FSI colormaps b)Pre-surgical 4D-flow and FSI streamlines c)Post-surgical 4D-flow and FSI colormaps b)Post-surgical 4D-flow and FSI streamlines e) Pre (left) and post-surgical(right) comparison between 4D Flow and FSI flow rate at the end of the descending aorta f) Representation of the plane considered for this analysis
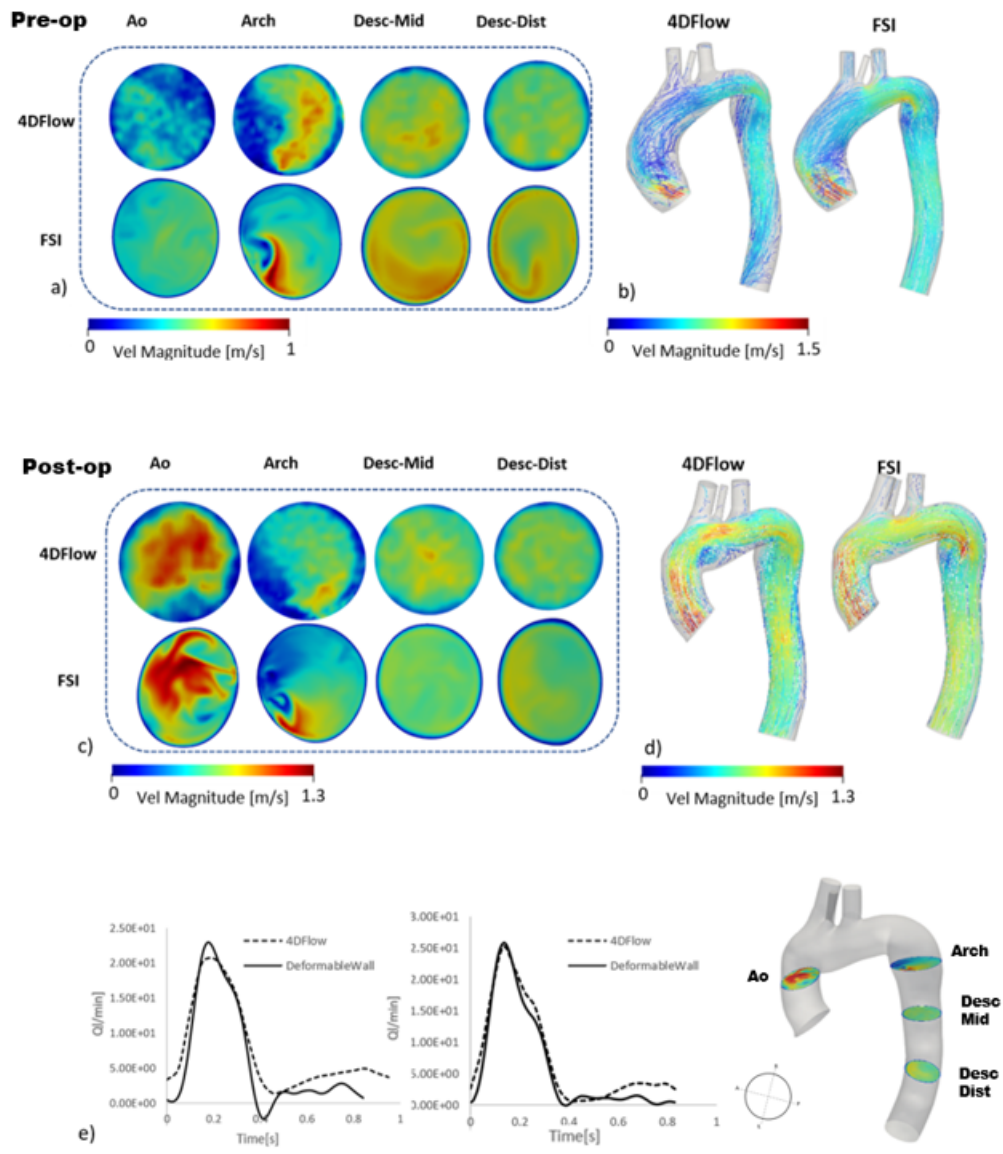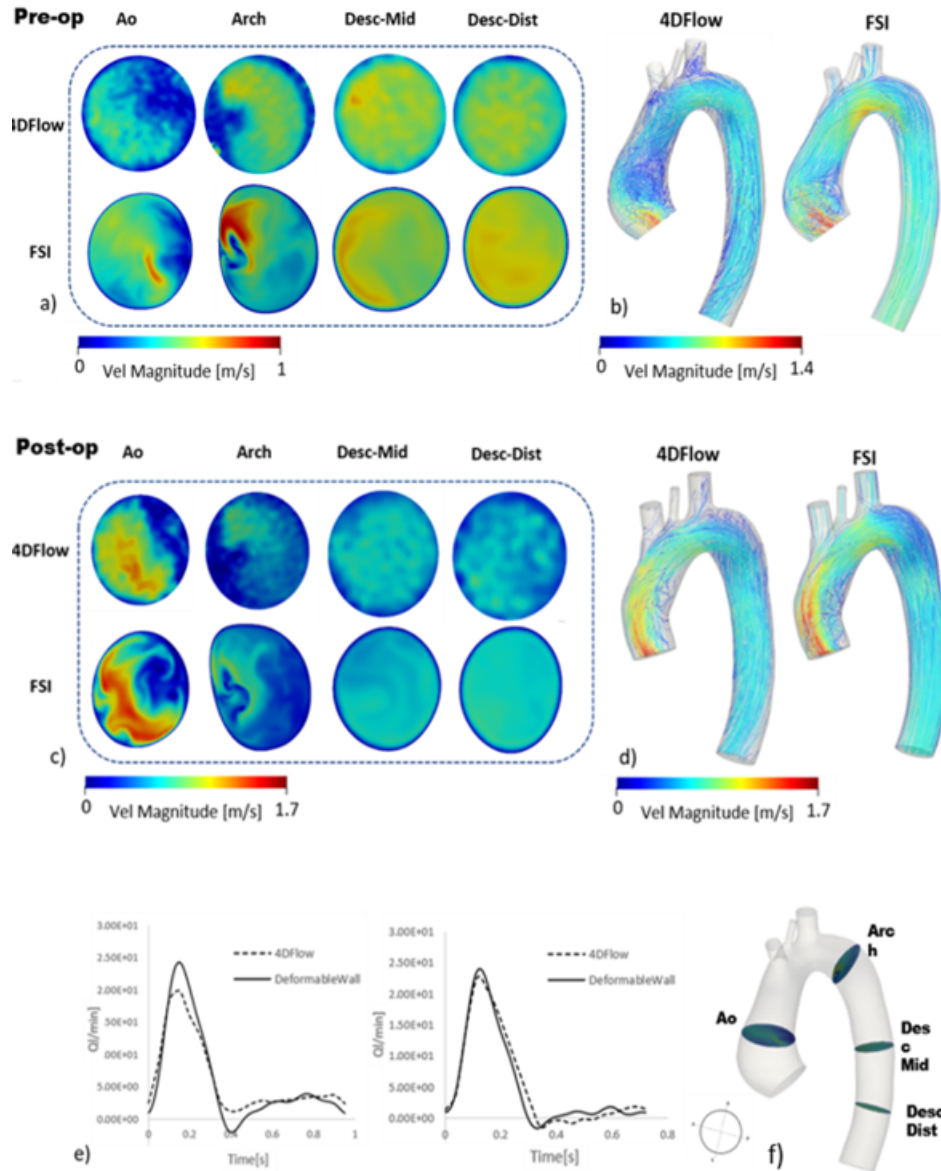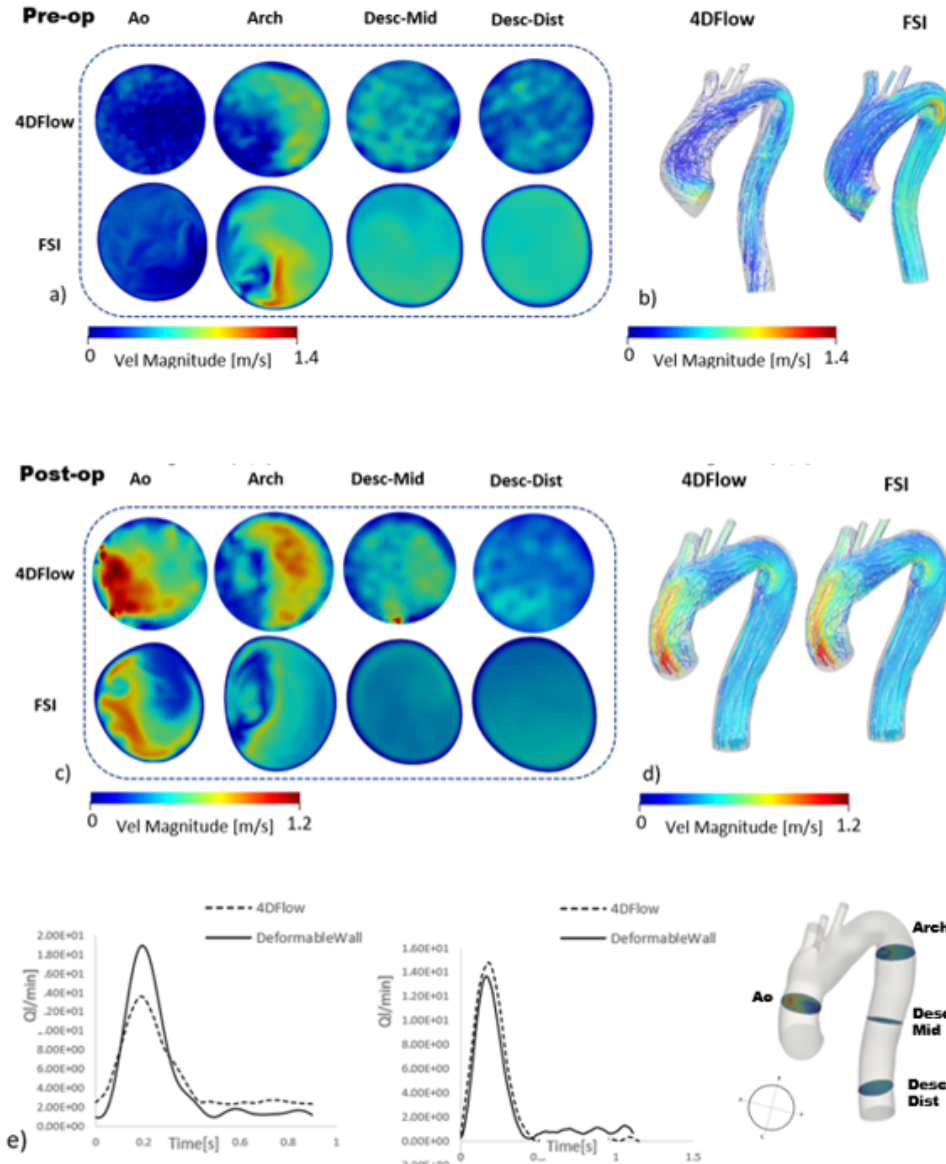
Figure 4.4: **Patient 2.** a) Pre-surgical 4D-flow and FSI colormaps b)Pre-surgical 4D-flow and FSI streamlines c)Post-surgical 4D-flow and FSI colormaps b)Post-surgical 4D-flow and FSI streamlines e) Pre (left) and post-surgical(right) comparison between 4D Flow and FSI flow rate at the end of the descending aorta f) Representation of the plane considered for this analysis
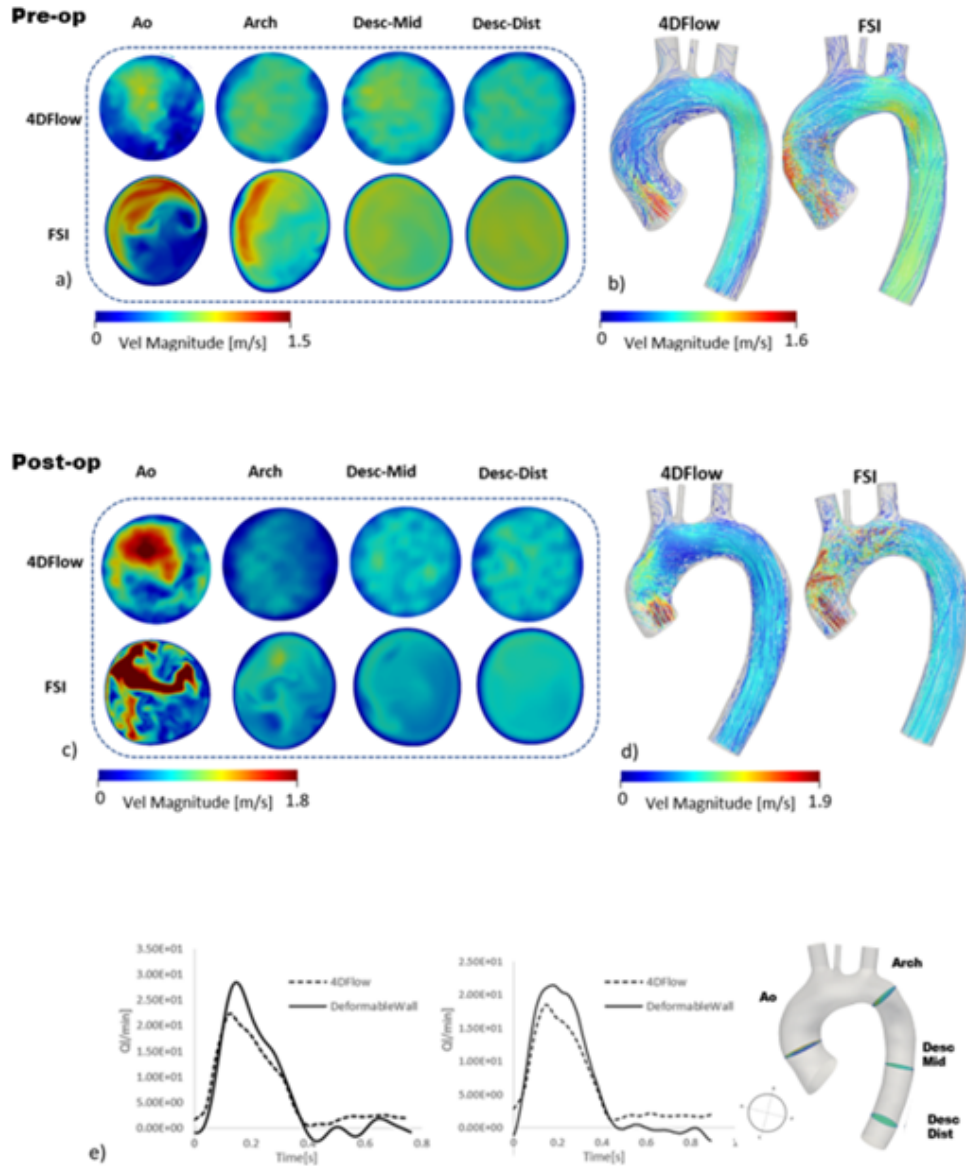
Figure 4.5: **Patient 3.** a) Pre-surgical 4D-flow and FSI colormaps
b)Pre-surgical 4D-flow and FSI streamlines c)Post-surgical 4D-flow and FSI
colormaps b)Post-surgical 4D-flow and FSI streamlines e) Pre (left) and
post-surgical(right) comparison between 4D Flow and FSI flow rate at the
end of the descending aorta f) Representation of the plane considered for this
analysis

Figure 4.6: **Patient 4.**a) Pre-surgical 4D-flow and FSI colormaps b)Pre-surgical 4D-flow and FSI streamlines c)Post-surgical 4D-flow and FSI colormaps b)Post-surgical 4D-flow and FSI streamlines e) Pre (left) and post-surgical(right) comparison between 4D Flow and FSI flow rate at the end of the descending aorta f) Representation of the plane considered for this analysis

Figure 4.7: **Patient 5.**a) Pre-surgical 4D-flow and FSI colormaps
b)Pre-surgical 4D-flow and FSI streamlines c)Post-surgical 4D-flow and FSI
colormaps b)Post-surgical 4D-flow and FSI streamlines e) Pre (left) and
post-surgical(right) comparison between 4D Flow and FSI flow rate at the
end of the descending aorta f) Representation of the plane considered for this
analysis

The disappearance of the vortical flows in the post-surgical ascending aorta suggested that the surgery was successful in restoring the physiological hemodynamic. Simulations and 4D Flow streamlines presented similar trends for all the patients, as displayed in Figure 4.3-4.7 b and d. The only visible difference between the two methodologies was found in the pre-operative configuration of the third subject, where velocities and vortical patterns were overestimated by the FSI analysis. This particular subject was affected by an extremely proximal ascending aortic aneurysm and, as assessed by the streamlines, the blood flow was particularly disturbed in the aneurysmatic region. At last, the simulation and 4D-Flow flow rates at the end of the descending aorta were compared, showing also in this case a good agreement. Concerning the quantitative comparison, the RMSE and the RRMSE at the systolic peak are reported in Table 4.5 for all the patients. From this analysis emerged that the RRMSE between the velocities obtained from 4D Flow and FSI analysis assumed an average value of 0.244±0.059, comparable with values found in published work [21]. *Desc-Mid* sections showed the lowest RRMSE for both the pre and post-surgical configurations (mean RMSE 0.194±0.031) , while the highest values were found in the *Ao* section of the pre-operative case (mean RMSE 0.322 ± 0.043), confirming the aforementioned velocity overestimation along this section. This showed that in the aneurysmatic region the FSI model was less capable to reproduce the in-vivo hemodynamic. Comparing pre and post-intervention cases, for all the patients the lowest average RRMSE was achieved by the post-intervention configuration (mean RMSE 0.274±0.029 vs 0.213±0.011 for respectively the pre and post-surgical case). The lowest and the highest average RRMSE were displayed respectively by Patient 1-post and Patient 3-pre-operative analysis (0.197 and 0.324 respectively).

The low errors and the good qualitative comparisons proved the capability

		Pre-intervention		Post-intervention	
		RMSE [m/s]	RRMSE	RMSE [m/s]	RRMSE
Patient 1	Ao	0.339	0.317	0.355	0.219
	Arch	0.175	0.181	0.176	0.161
	Desc-Mid	0.222	0.222	0.201	0.182
	Desc-Dist	0.242	0.206	0.20	0.227
	Mean	0.244	0.231	0.245	0.197
Patient 2	Ao	0.152	0.302	0.276	0.234
	Arch	0.228	0.297	0.213	0.233
	Desc-Mid	0.145	0.212	0.161	0.180
	Desc-Dist	0.197	0.316	0.167	0.217
	Mean	0.181	0.281	0.204	0.216
Patient 3	Ao	0.467	0.395	0.589	0.289
	Arch	0.212	0.269	0.176	0.263
	Desc-Mid	0.207	0.239	0.159	0.186
	Desc-Dist	0.286	0.395	0.170	0.194
	Mean	0.228	0.324	0.273	0.233
Patient 4	Ao	0.170	0.316	0.275	0.215
	Arch	0.178	0.254	0.212	0.252
	Desc-Mid	0.134	0.193	0.132	0.183
	Desc-Dist	0.188	0.312	0.156	0.198
	Mean	0.167	0.269	0.193	0.212
Patient 5	Ao	0.121	0.282	0.301	0.199
	Arch	0.231	0.277	0.254	0.259
	Desc-Mid	0.142	0.215	0.166	0.127
	Desc-Dist	0.183	0.293	0.115	0.254
	Mean	0.169	0.266	0.209	0.210

Table 4.5: Pre and post-operative RMSE and RRMSE between 4D-Flow and FSI

of this FSI analysis to reproduce patients' hemodynamic. These models were therefore used to assess fluid dynamic and biomechanical quantities.

4.3 Pre vs post-surgical comparison

To study and compare the pre and post-intervention hemodynamic, the quantities reported in Section 3.4.2 (e.g. OSI,WSS and Strain) were analyzed, with a particular focus on the descending tract of the aorta, which is more

prone to develop pathologies due to hemodynamic modifications caused by the surgery.

Firts of all, the pre and post-operative velocities were compared. In Figure 4.8 the velocity contours along a sagittal plane are displayed, overlapped with the projection of the tangential component of the local velocity. In the descending aorta, the neat velocity pattern already evinced from the streamlines was displayed for both the pre and post-intervention situations. Focusing on the post-surgical configuration of Patient 2, a vortical pattern was observed at the aortic arch intrados, which was less pronounced in the pre-intervention case.

In Table 4.6 the median, the 10th and the 90th percentiles of the velocity in the descending aorta are reported. From this analysis emerged that higher velocities were developed in the post-intervention configuration, with the exception of Patients 3 and 5.
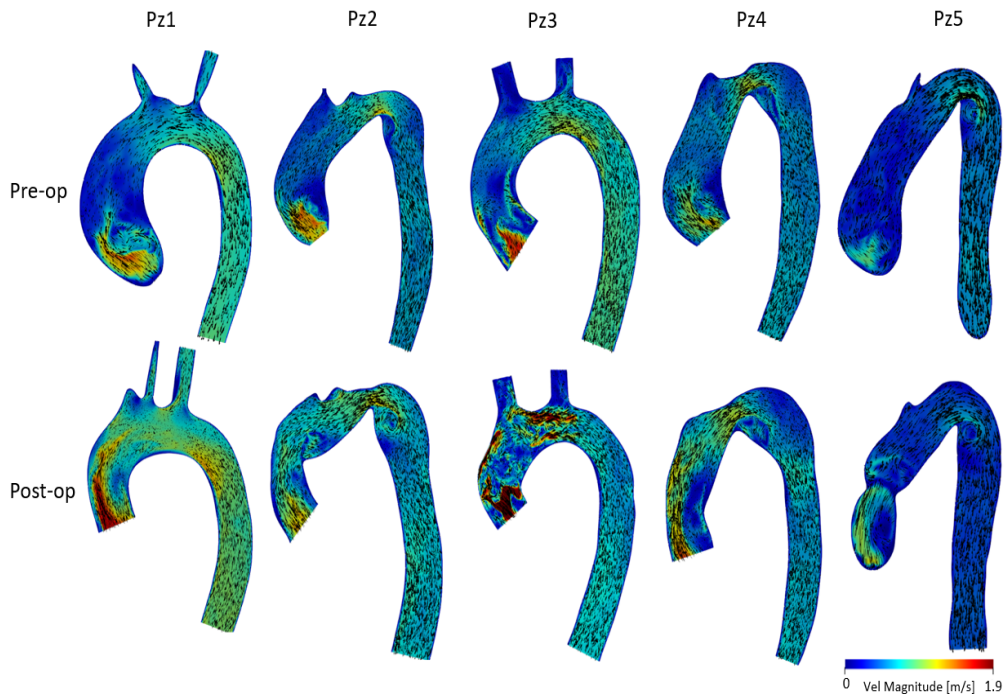
Figure 4.8: Comparions of pre and post-intervention velocity along the sagittal plane

	Pre-intervention Median $[10^{th} \div 90^{th}]$[mm/s]	Post-intervention Median$[10^{th} \div 90^{th}]$[mm/s]
Patient 1	761.0 [487.3 ÷ 822.6]	873.3 [532.6 ÷ 979.0]
Patient 2	514.9 [360.8 ÷ 645.3]	578.7 [314.8 ÷ 731.8]
Patient 3	739.0 [368.8 ÷ 862.2]	596.3 [320.1 ÷ 703.7]
Patient 4	506.4 [326.2 ÷ 635.9]	534.4 [326.7 ÷ 662.4]
Patient 5	545.7 [298.7 ÷ 661.1]	382.8 [199.8 ÷ 462.6]

Table 4.6: Median and 95th percentile of the velocity in the descending aorta

4.3.1 Hemodynamic quantities - OSI and WSS

The OSI and WSS distribution is reported in Figure 4.9 as an exemplary case, while in Figure C.1 and Figure C.2 (Appendix C) the distribution of OSI and WSS for all the patients is represented.

Regarding the OSI, a visual comparison allowed observing that pre-intervention peaks were intensified in the post-intervention descending aorta. Furthermore, the posterior region immediately downstream the LSA
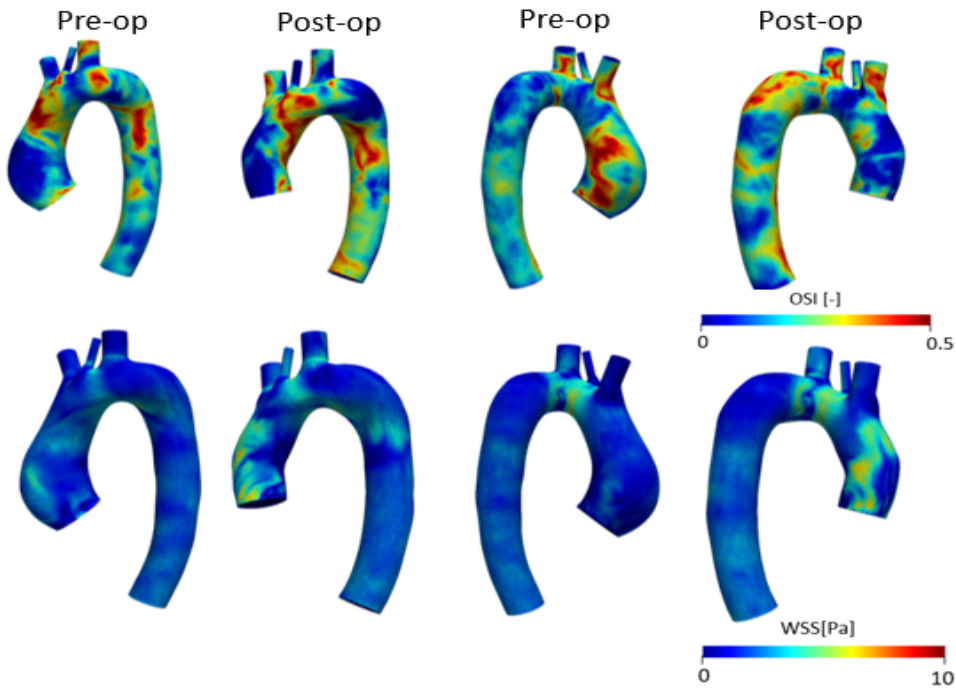
Figure 4.9: OSI (top) and peak WSS (bottom) distribution

branch showed a remarked OSI intensification, with the only exception of Patient 2, which displayed the opposite trend.

Observing the WSS distribution at systolic peak(Figure C.2.), a visible intensification on the whole aorta was reported for the first patient. An evident increase was observed also in the posterior region of Patient 3 ascending aorta, while in the descending tract the same subject displayed a WSS decrease. It is worth noticing that this patient was highly hypertensive (176-108 mmHg, see Table 3.3) and showed high blood flow velocity at the inlet of ascending aorta.

Observing the posterior region downstream the LSA branch, Patients 1 and 2 showed a WSS intensification, while in Patients 3 and 5 the opposite trend was observed. In Patient 4 no significant variations were displayed.

To assess the possible hemodynamic changes induced by the graft in the descending aorta, a deeper analysis was performed on this region, with particular focus on the proximal portion downstream the LSA branch, which displayed important variations for both OSI and WSS. The two regions of
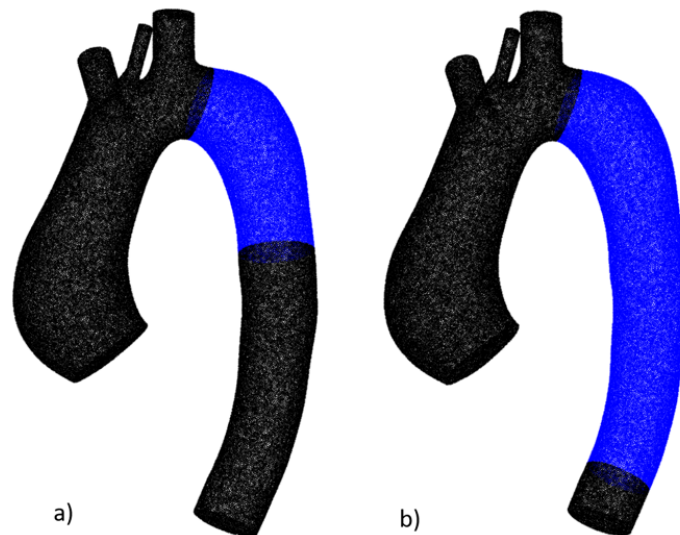
Figure 4.10: Region considered for further hemodynamic analysis a) Proximal descending aorta b) Whole descending aorta
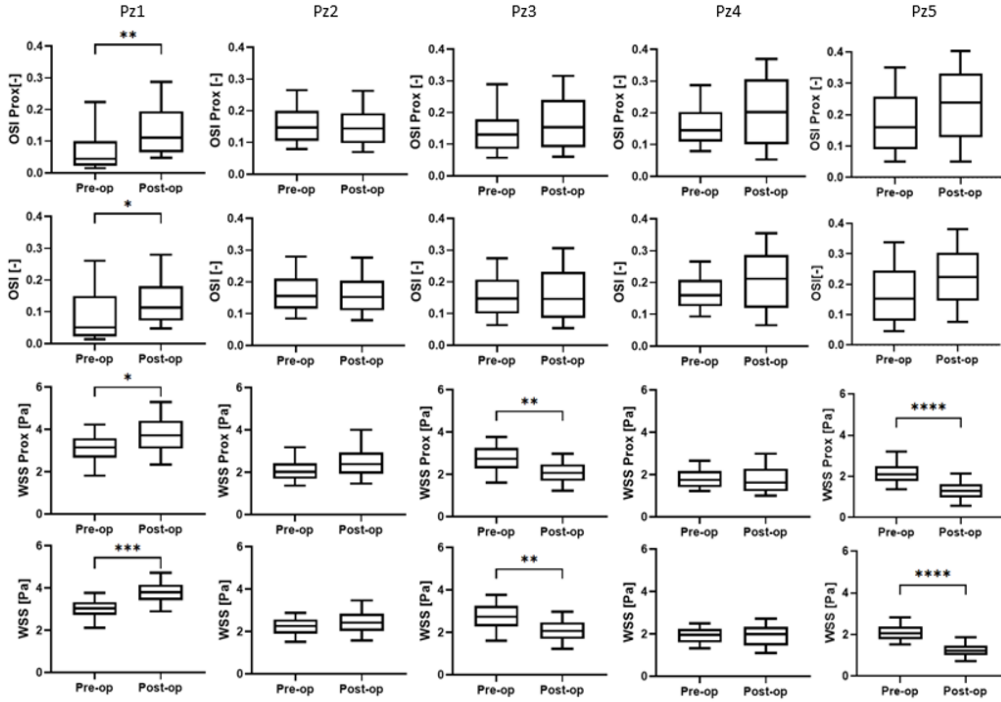
Figure 4.11: Comparison between percentiles population of OSI (top two rows) and WSS (bottom two rows) at systolic peak between pre and post-surgical configurations *=p<0.05, **=p<0.01,***=p<0.001,****=p<0.0001

interest are displayed in Figure 4.10.

A *t-test* was performed between percentile population (from 5th to 95th percentile) of OSI and systolic peak WSS. This analysis was executed using GraphPad Software (San Diego, California USA). For all the analyzed populations, a normality test was performed to check whether the dataset were well modeled by a normal distribution. If the two populations passed the normality test, an unpaired t-test was performed, assuming that both population had the same standard deviation. Otherwise Mann-Whitney test was executed, comparing the ranks. In both cases, an unpaired experimental design was chosen, since the two percentile populations were extracted from two different meshes (the pre and post-intervention ones). The boxplots obtained from this analysis are reported in Figure 4.11 for both the regions

considered. In Appendix C the tables reporting the 10th and the 90th percentile and the median of each quantity (e.g. OSI and WSS in the whole aorta and in the proximal region) are represented (Tables C.1-C.4).

From this analysis emerged that despite the significant spatial distribution alterations above described, few statistical differences between the pre and post-surgical population were present. Important differences were observed for the first patient. In the post-operative configuration, he displayed a visible increase of both WSS and OSI along the whole descending aorta. Other statistically significant discrepancies were visible in Patinets 3 and 5, which displayed significantly lower WSS in the post-operative case.

4.3.2 Biomechanical quantities: the strains

Analyzing now the strain distribution at systolic peak (Figure 4.12 as an exemplary case, in Figure C.3 all the subjects are represented), the maximum value was reported at the intrados of the ascending aneurysmatic aorta for all the patients. In the region substituted by the graft, low strain values were always calculated, but downstream the implant an intensification was
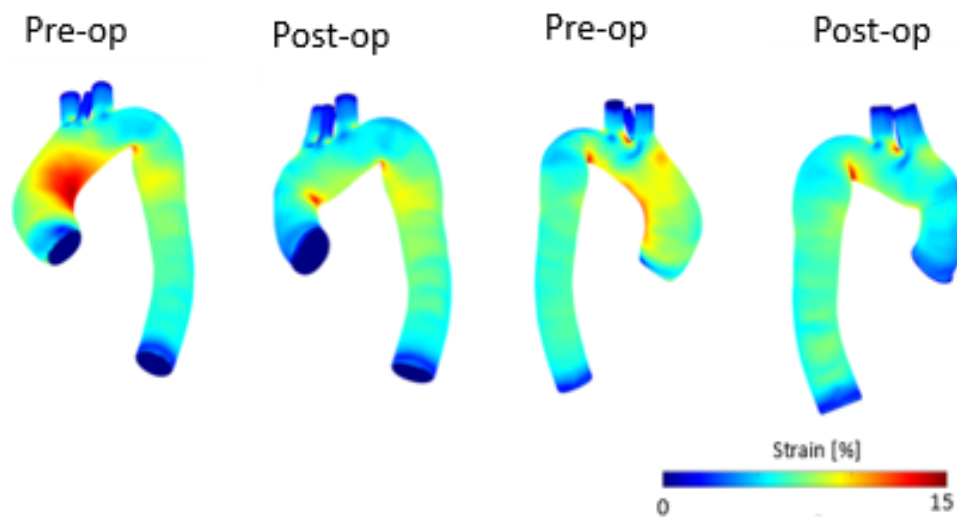
Figure 4.12: Strain distribution
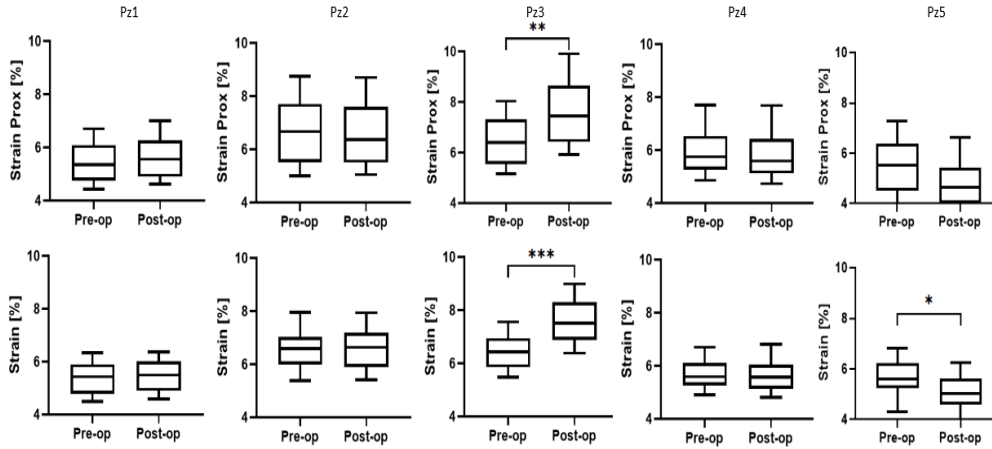
Figure 4.13: Comparison between percentiles population of strain at systolic
peak between pre and post-surgical configurations
*=p<0.05,**=p<0.01,***=p<0.001

registered in all the subjects. This behaviour was particularly visible in
Patient 3, confirming the disturbed hemodynamic assessed also by WSS. All
the patients showed a peak at the intrados of the proximal aorta: as for
the other two quantities considered, the region downstream the LSA branch
resulted particularly critical. Also for the strains, a *t-test* between percentile
populations was performed, following the same procedure reported for OSI and
WSS and considering the strain at systolic peak. The boxplots representing
the results of this analysis are reported in Figure 4.13. In this case, no
remarkable differences were detected between the pre and post-operative case
in Patients 1,2 and 4. Patient 3 and 5, reported a significant variation of
post-operative strains, but with opposite trend: while an increase was observed
for for Patient3, a decrease was displayed for Patient 5.

4.3.3 Conclusions

From the statistical analysis performed on descending aortic OSI, WSS
and strains, some common trends were observed.
As far as the OSI was concerned, no significant difference was found in the

median value between the pre and post operative configuration as assessed by the *t-test*, which reported statistically relevant difference only for the first Patient. But as displayed by the trend showed by the boxplot in Figure 4.11, a general increase of the 90th percentile was reported, assessing an intensification of post-operative OSI peaks. This increment was particularly evident in the proximal region of the descending aorta. The value of the median and 90th percentile of the OSI in the proximal portion of the vessel are reported in the following table, while all the other values can be found in Table C.1 and C.2.

ProxOSI[-]	Pre-intervention		Post-intervention	
	Median	90^{th}perc	Median	90^{th}perc
Patient 1	0.044	0.223	0.111	0.287
Patient 2	0.146	0.265	0.144	0.262
Patient 3	0.131	0.230	0.153	0.316
Patient 4	0.146	0.2867	0.206	0.370
Patient 5	0.1159	0.352	0.293	0.406

Table 4.7: Median and 90th percentile of pre and post intervention OSI in proximal portion of descending aorta

This common behavior may be consequence of disturbed hemodynamic induced by graft implant. The only exception to this trend was Patent 2, which showed no difference between the pre and post-operative configuration (Table 4.7), maybe due to the section decrease at the isthmus of the proximal descending aorta, which may reduce the hemodynamic changes induced by the graft.

No common trend was observed concerning the WSS, which showed an increment in Patients 1 and 2, a decrease in Patients 3 and 5 and almost no change in Patient 4. Since WSS are proportional to the derivative of the velocity (Equation 3.15), an important dependency was observed between the pre and post operative velocity changes and the WSS. Patient 1 showed an important increment in post operative velocity (from 761 to 873 mm/s as median value, Table 4.6) and therefore showed a WSS increase, while Patient

3 and 5 displayed a velocity reduction (from 739 to 596 mm/s and from 545 to 382 mm/s respectively) and as a consequence decreased WSS. Concerning Patient 2, he reported a small velocity increase (from 514 to 578 mm/s), which was reflected is small WSS increments. In Patient 4 no WSS variations were visible, due to the small velocities changes (from 506 to 534 mm/s).

Usually, graft implant, with his higher stiffness, does not accomplish the compliant effect of the native vessels, dissipating less energy than the natural vessel and producing a higher velocity in the downstream region. Furthermore, the graft reduces the inlet section, producing velocity increment. The diverse behavior of Patient 3 and 5 was explained by the the lower post-operative inlet flow rate with respect to the pre-operative one (from 6.9 to 6 l/min and from 4.8 to 2.9 l/min for respectively Patient 3 and 5).

Considering the strains, the only statistical difference was observed in Patients 3 and 5, while for the other three subjects pre and post-operative strains were absolutely comparable, as it can be observed from Figure 4.13 and from the values reported in Tables C.5 and C.6. Given these results, graft implant seems to have no effect on descending aorta strains. This is proven also by the the trend observed in Patients 3 and 5: while in the first subject post-operative strains were higher than the pre-operative ones, in the other the opposite trend was displayed. This behaviour may be explained by pressure changes between the two configurations: while in Patient 3 a higher pressure was found for the post operative case (153-78 vs 176-198 mmHg systolic vs diastolic pressure for respectively the pre and the post-operative case), Patient 3 displayed the opposite situation (141-79 vs 126-65 mmHg).

4.4 Computational times

One important aspect to be considered is the computational time. The CMM-FSI formulation allows to significantly reduce the computational cost of FSI simulations with respect to the classical analysis. The limitation of this approach lies in the need to run a preliminary CFD simulation in order to correctly set the initial condition for the FSI analysis. In Table 4.8 the mean computational times employed to run a complete simulation exploiting the CMM-FSI are reported and compared with the one obtained running a classical FSI analysis [11].

	Nr. CPU	Nr. Cardiac Cycles	Computational Time
Rigid Wall	40	3	~ 2 days
Deformable Wall	40	2	~ 5 days
Classical FSI	24	2	~ 10 days

Table 4.8: Computational cost

The simulations were run on DELL R410 with Intel® Xeon® CPU E5670 @ 2.93GHz processors.

It is worth noticing that these computational time were achieved with a mesh of $\sim 5mln$ elements, while in the classical FSI a mesh with $\sim 2.7mln$ element was adopted [11].

Chapter 5

Discussion and Conclusions

In this chapter, the results obtained with the present thesis work will be discussed. Firstly, the workflow and the achieved results will be summarized. Then, general conclusion will be drawn, highlighting the innovative aspects of this projects. Finally, limitations and possible future development will be outlined.

5.1 Discussion

In literature, there is a lack of studies assessing hemodynamic changes induced by surgical graft replacement of ascending aneurysmatic aorta.

To the best of this author's knowledge, the only computational study which focused its attention on the comparison between the pre and post-operative hemodynamic was a pilot study developed by our research group, where only one patient was analyzed.

In this master thesis work an innovative analysis to assess hemodynamic changes due to surgical graft replacement of native aneurysmatic aorta was developed, exploiting the Coupled Momentum Method for FSI. This formulation starts from a conventional stabilized finite element formulation for the Navier-Stokes equation in a rigid domain and modifies it in order to account for the effect of wall deformation on the fluid domain.

Five patients affected by ascending aortic aneurysm were considered in the present work. All the subjects presented a normal tricuspid aortic valve and were treated with the valve-sparing technique. For each pre and post-intervention configuration of each patient, a patient-specific fluid-solid interaction analysis was performed. The focus was mainly on the descending tract of the aorta, which is more prone to develop pathologies due to ascending aortic graft implant.

5.1.1 Simulation setting

Through the development of the workflow presented in this thesis work, diverse aspects showed critical importance. The step of MRA segmentation was fundamental for the good outcome of the FSI analysis. MRA images had a low spatial resolution and the automatic segmentation tool provided by ITK-SNAP was not able to capture accurately the geometry with the needed

level of accuracy. To overcome this issue, manual adjustments were needed. One of the most crucial aspects was the manual co-registration. A good co-registration of the model in both the ascending and the descending tract of the aorta was needed to obtain a model able to accurately reproduce patient's hemodynamic. The obtained geometry reproduced patient's aorta from the sino-tubular junction to the distal descending aorta. The plane at the level of the sino-tubular junction constituted the inlet of the model, while the three supra-aortic branches and the distal descending aorta formed the outlets. Once the model was correctly co-registered, the inlet was extracted and used to obtain patient's velocity vectors from 4D-Flow data. These vectors were then used to impose patient-specific inlet boundary conditions. At the outlets, a three-element Windkessel model was used to account for the downstream vessels. RCR values were computed exploiting Pirola's work [26], which required the mean flow rate through each outlet section. To compute these values, 4D-Flow dataset was once again exploited. The noise affecting 4D-Flow data did not allow to measure quantities directly at the aortic arch. For this reason, the flow rate through the aortic branches was calculated as the partition of $Q_{in} - Q_{DescAo}$ based on the area of each supra-aortic outlet section. Q_{DescAo} (the flow rate through the descending aorta) was calculated as the mean flow rate through five different descending aorta sections.

Another important aspect regarded the wall parameters setting. SimVascular software did not provide the possibility to set diverse wall properties to different portions of the wall domain, not allowing to account for the different mechanical characteristics of the graft implant. To overcome this issue, a Python code was developed. This code permitted to change ModelFaceID property of the model, which was exploited by SimVascular to set boundary conditions and material characteristics. The Python code was able to modify this property in a specific portion chosen by the user, allowing to set different

material properties in that specific region. This constituted an important addition to SimVascular capabilities.

A total of five patients was considered in this work and for each of them, both pre and post-surgical configurations were analyzed.

5.1.2   Model evaluation

The main parameter considered to evaluate the capability of the model to reproduce the in vivo hemodynamic was the RRMSE calculated between model and 4D-Flow velocities. To reliably perform this calculation, the velocity data obtained from the simulation were down-sampled to match 4D-Flow data mesh. RRMSE calculation was performed on four different aortic sections, one in the ascending portion and three along the descending tract of the vessel. The RRMSE values were comparable with the ones found in literature [21], with a total mean RMSE of 0.244 ± 0.059. The lowest RRMSE was observed along planes in the middle of the descending aorta (mean RRMSE 0.194 ± 0.031), while the highest errors were found along the ascending aorta in the aneurysmatic region: here a mean RRMSE of 0.322 ± 0.043 was obtained. Beside this quantitative evaluation, the model was also qualitatively compared with 4D-Flow data, creating colormaps and streamlines. For each considered section (e.g., the one along the ascending aorta and the three along the descending tract of the vessels), a contour was created for both FSI and 4D-Flow data. Through the comparison of these colormaps, a good agreement was found between the two methodologies, assessing the FSI analysis capability to reproduce 4D-Flow velocity distribution. A good accordance was observed comparing the streamlines too: with both the methodologies a straight blood flow was noticed in both pre and post-intervention descending aorta and ascending pre-surgical aorta, while in the aneurismatic pre-operative region vortical patterns were found.

Given the good accordance found between FSI and 4D-Flow data with both the qualitative and quantitative evaluation, the capability of this FSI analysis to reproduce patient's hemodynamic was assessed. Stated this important result, this FSI model was used to accurately assess hemodynamic parameters, like WSS. This quantity can be calculated also by means of 4D-Flow data, but since WSS are calculated as velocity spatial gradient and since 4D-Flow data does not provide a good spatial and temporal resolution, these measures may be inaccurate.

5.1.3 Hemodynamic quantities assessment

For each subject analysed in this study, the pre and post-operative descending aorta fluid dynamic was compared through four quantities: velocity, WSS, OSI and strains. For these last three entities a *t-test* between percentile population was performed to assess statistically significant hemodynamic changes. Since the two sets of data (pre and post-operative) were extracted from two different meshes, an unpaired experimental design was chosen. Based on whether the dataset was well modeled by a normal distribution, either a t-test (normal-distribution) or a Mann-Whitney test (non-normal distribution) was performed. The data were compared in both a proximal region of the descending aorta and in the whole descending tract of the vessel.

Velocity comparison. A common trend of higher post-operative velocities was observed in Patient 1 (from 761 to 873 mm/s), Patient 2 (from 514 to 534 mm/s) and Patient 4 (from 506 to 514 mm/s). Indeed, as the graft shows higher stiffness than the aorta, it does not accomplish the compliant effect of the native vessel. This brings to lower energy losses in the graft-substituted region and therefore higher velocities are experienced by the downstream vessels [22]. In addition, the graft reduces the section of the ascending aortic

tract, further increasing the velocity. This trend was confirmed by previous 4D-Flow analysis [77]. Patient 3 and 5 did not respect this trend, reporting a significantly lower velocity in the post-intervention configuration (from 739 to 596 and from 545 to 382 mm/s respectively). This was explained by the decreased post-operative inlet flow rate, which lowered from 6.9 l/min to 6.1 l/min for Patient 3 and from 4.8 to 2.9 l/min for Patient 5.

In all pre-operative configurations, a disturbed hemodynamic with vortical flows was displayed at the extrados of the ascending aorta, where the dilatation due to aneurysm was present. A neater flow was observed in the same region of the post-operative configuration, witnessing good surgical outcomes. In both pre and post-operative cases, no disturbed hemodynamic was displayed by descending aortic streamlines, showing a straight common behavior for all the analyzed cases. At the intrados of the proximal part of the descending aorta, the streamlines highlighted an increased velocity in all the pre and post-surgical situations, revealing a possible critical region.

OSI. In the post-operative configuration, a general increment of OSI was visually assessed observing the distribution reported in Figure C.1. The peaks shown in the pre-intervention descending aorta were intensified in the post-surgical case.

Despite these visible distribution alterations, in the descending aorta statistically relevant changes were revealed by *t-test* analysis only for one patient, assessing that the OSI median value was the same for both the pre and post-operative situation. The only important alterations were reported by Patient 1, where significantly higher OSI was experienced in the post-operative configuration, in particular in the proximal part of the descending aorta.

But observing the boxplot in Figure 4.11 and comparing the 90th percentiles (Table 4.7), significantly higher values were found for this quantity in the post-operative configuration: in the proximal region, a 6.4% difference was

found for Patient 1, 37.4% for Patient 3, 29.4% for Patient 4 and 15.3% for Patient 5, while along the whole vessel 7% difference was displayed for Patient 1, 11.6% for Patient 3, 33.4% for Patient 4 and 12% for Patient 5.

These data suggests that an OSI increment is induced by the graft on the whole descending aorta, with an intensification in the proximal tract. The only non-significant variation was observed in Patient 2, where the difference was 1.1% in both regions. This behavior may be explained by the isthmus in the proximal tract of the descending aorta, which may reduce the hemodynamic changes induced by the graft.

WSS. All the patients showed a visible WSS increment in the ascending aorta after the surgery but, focusing on the descending aorta, no common behavior was found. Observing the proximal tract, Patients 1 and 2 displayed a WSS intensification, Patients 3 and 5 a decrement, while Patient 4 reported no variations. This can be explained considering the dependency of WSS on velocity derivative. As reported above, Patient 1 and 2 showed a velocity increment between the pre and post-surgical configuration, particularly evident in Patient 1, which indeed reported statistically higher post-operative WSS in the *t-test*. Given the low velocity increment displayed by Patient 4, almost no variations were observed in WSS stress values, while a marked velocity decrement was reported by Patients 3 and 5, which indeed displayed statistically significant lower WSS in the post-operative configuration.

Since the graft usually produces a velocity increment, it can be assessed that graft implant generally raises WSS values, with the exception of subjects with particular hemodynamic conditions (e.g. a lower post-operative inlet flow rate).

Strains Among the output variables obtained from the adopted solver, the strains were not provided. For this reason, an in-house Matlab code was developed to calculate the strains given the displacements as input variables.

91

Local consistent reference systems were reconstructed for each element exploiting the centerline direction, and the Green Lagrange formulation was adopted to calculate the strains. The variables obtained from this code were then evaluated against the strains calculated by Abaqus software in the same configuration. These two sets of data were studied through a linear regression analysis and a Bland-Altmann plot. The first analysis showed an $R^2 =0.994$, demonstrating that the two sets of data were almost perfectly fitted by a line, while the Bland-Altmann plot reported a bias of -0.72%, with 3.98% and -5.42% as limits of agreement. Both the analysis showed good accordance between the two datasets and therefore the code was considered a valid routine for strain calculation.

Analyzing the strain distribution (Figure C.3), a peak was always present at the intrados of the descending aorta, in accordance with the results found in literature [78]. In the pre-operative configuration, a region of high strain was found at the intrados of the ascending aorta, while lower values were found in the same post-surgical region, thanks to the high mechanical properties of the graft. As expected, downstream the graft a strain increase was observed in all the patients, showing peak values at the suture site. This behavior was particularly remarked in Patient 3.

Focusing on the descending aorta, no significant differences were assessed with the *t-test*. Patient 3 and Patient 5 were an exception to this tendency, but the two patients showed an opposite trend: while Patient 3 displayed a strain increment in the post-operative configuration, Patient 5 reported a decrease. This behavior was explained considering the pressure difference between the pre and post-surgical situation: while Patient 3 registered a higher post-operative pressure (153-78 vs 176-198 mmHg), Patient 2 displayed a lower post-intervention pressure (141-79 vs 126-65 mmHg).

Conclusions. From this analysis a relationship between graft implant and

hemodynamic quantities (i.e. WSS and and OSI) variation has emerged. In particular, the graft implanted in the ascending tract of the aorta seemed to produce an increment in both quantities. Diverse studies report that alteration in these two entities may enhance the atherogenic process. Indeed, when endothelial cells are subjected to intense mechanical stimuli, they tend to trigger atherogenic process and even aneurysms formation [18]. It has been reported that OSI close to 0.5 is critical for the atherogenic process enhance [19]. Concerning WSS, values <0.4 Pa and significantly higher (i.e.>10 Pa [20]) than the physiological value (1.79 ± 0.71 [18]) may induce an adverse cell response. In this study, OSI and WSS distribution were always below these thresholds, but peaks were observed. The highest WSSs were displayed by Patient 1 (7.7 Pa), while region with OSI close to 0.5 were present in all the considered cases (Figure C.1). The proximal tract of the descensing aorta showed the most critical behaviuor, displaying generally higher OSI values. Concerning the strains, no significant connection was observed between strain changes in the descending aorta and graft implant, in disagreement with what was observed in previous studies. In these works a circumferential strain increase in the descending aortic tract was observed by means of transthoracic and transesophageal echocardiography [79–81]. An important strain increment was observed along the graft suture site in the ascending aortic tract: given graft's higher stiffness, a compliance mismatch is present between the graft and the vessel, producing higher strains at the interface between the two regions. These conclusions were assessed based on a 5-patients pool, which constitutes a various population, but to verify these results, the current study should be enlarged involving a higher number of subjects.

5.2 Limitations and future work

The FSI model developed in this work shows some limitations and approximations, which may set the basis for future developments.

5.2.1 Limitations

In this work, all the parameters used to set the simulation were extracted from patient's data, with the only exception of wall thickness and Young Modulus, which were adopted based on values found in literature. The model evaluation showed good accordance with 4D-Flow data but developing a methodology to measure patient-specific wall properties would constitute an interesting development.

One intrinsic solver limitation is the need to run a rigid wall simulation to set the initial conditions for the deformable wall case. The computational cost of these simulations is lower than the one obtained with the classical FSI, but the need to run a preliminary simulation significantly elongates the computational time.

Another aspect that should be considered is the low spatial and temporal resolution of 4D-Flow data, which may bring to an error in the estimation of inlet and outlet boundary conditions. This issue was solved in this work by computing the outlet flow rate as the mean flow rate of different descending aorta sections and partitioning the flow rate through the aortic branches according to their area, but other solutions may simplify the process.

5.2.2 Future work

Beside the adoption of patient specific wall properties, which may be computed from CINE-MR data, the ability of the model to reproduce the in vivo hemodynamic may be enhanced by differentiating the wall properties

in the aneurysmatic region, which usually show a lower thickness with respect to the other vessel's regions.

Another interesting development would be the enlargement of the pool of patients, to better assess the hemodynamic changes induced by graft implantation. In this context, the patients could be grouped in categories based on arch shape, trying to understand whether this aspect influences the surgical outcomes.

To simplify the simulation setting, an automatic co-registration algorithm may be developed, to avoid the manual co-registration. To do that, either MRA or 4D-Flow data should be roto-translated in the reference system of the other set of data.

Finally, the assessment of hemodynamic changes due to different graft length and material properties may be interesting too. The outcomes of this study may help the clinicians in the choice of the best graft for a specific patient.

5.3 Conclusions

To the best of this author's knowledge, this study constitutes the first work where the hemodynamic changes produced by surgical graft replacement of ascending aneurysmatic aorta are assessed on various patients by means of an FSI analysis.

For each patient the pre and post-intervention situations were analyzed through a patient-specific FSI simulation, exploiting the CMM-FSI formulation. This methodology proved its ability to accurately reproduce patient-specific fluid-dynamic and was able to provide important hemodynamic quantities. This analysis offered to the clinicians a deeper insight into fluid-dynamic changes due to this treatment, providing them with an additional tool to assess possible post-surgical risks.

Appendix A

RCR Values

Patient1	Pre-intervention			Post-intervention		
	R	C	R	R	C	R
BCA	0.0549	1.3559	1.2653	0.0329	2.3766	0.7203
LCCA	0.2418	0.2689	6.4158	0.1586	0.6055	2.7974
LSA	0.0569	1.4305	1.1945	0.0525	1.5828	1.0784
Outlet	0.0107	13.6946	0.1200	0.0102	13.6188	0.1212

Table A.1: RCR values for Patient 1. Values are given in MGS units: $g/s*mm^4$ and $s^2 * m^4/g$ for respectively R and C

Patient2	Pre-intervention			Post-intervention		
	R	C	R	R	C	R
BCA	0.0417	1.0888	1.6023	0.0324	1.1714	1.4958
LCCA	0.2402	0.2377	7.2897	0.2416	0.2040	8.5342
LSA	0.0393	1.1474	1.5208	0.0420	0.9330	1.8765
Outlet	0.0080	10.8096	0.1576	0.0074	12.0999	0.1406

Table A.2: RCR values for Patient 2. Values are given in MGS units: $g/s*mm^4$ and $s^2 * m^4/g$ for respectively R and C

Patient3	Pre-intervention			Post-intervention		
	R	C	R	R	C	R
BCA	0.0273	1.1568	1.5200	0.0258	0.9637	1.8317
LCCA	0.2791	0.1532	11.4034	0.3588	0.0978	17.9505
LSA	0.0293	1.0872	1.6171	0.0310	0.8226 2.1451	
Outlet	0.0081	13.3564	0.1259	0.0086	9.4701	0.1804

Table A.3: RCR values for Patient 3. Values are given in MGS units: $g/s*mm^4$ and $s^2 * m^4/g$ for respectively R and C

Patient4	Pre-intervention			Post-intervention		
	R	C	R	R	C	R
BCA	0.0320	1.9091	0.9056	0.0288	3.8235	0.4394
LCCA	0.1943	0.3979	4.3039	0.1835	0.7630	2.1626
LSA	0.0201	2.8580	0.6062	0.0261	4.1559	0.4046
Outlet	0.0075	14.7702	0.1137	0.0077	12.9830	0.1301

Table A.4: RCR values for Patient 4. Values are given in MGS units: $g/s*mm^4$ and $s^2 * m^4/g$ for respectively R and C

Patient5	Pre-intervention			Post-intervention		
	R	C	R	R	C	R
BCA	0.0295	2.0721	0.8343	0.0316	4.5656	0.3605
LCCA	0.2204	0.3610	4.7380	0.1897	0.9602	1.6746
LSA	0.1369	0.5463	3.1400	0.1266	1.3642	1.1855
Outlet	0.0081	9.9308	0.1721	0.0081	6.8719	0.2523

Table A.5: RCR values for Patient 5. Values are given in MGS units: $g/s*mm^4$ and $s^2 * m^4/g$ for respectively R and C

Appendix B

Mesh Quality Parameters
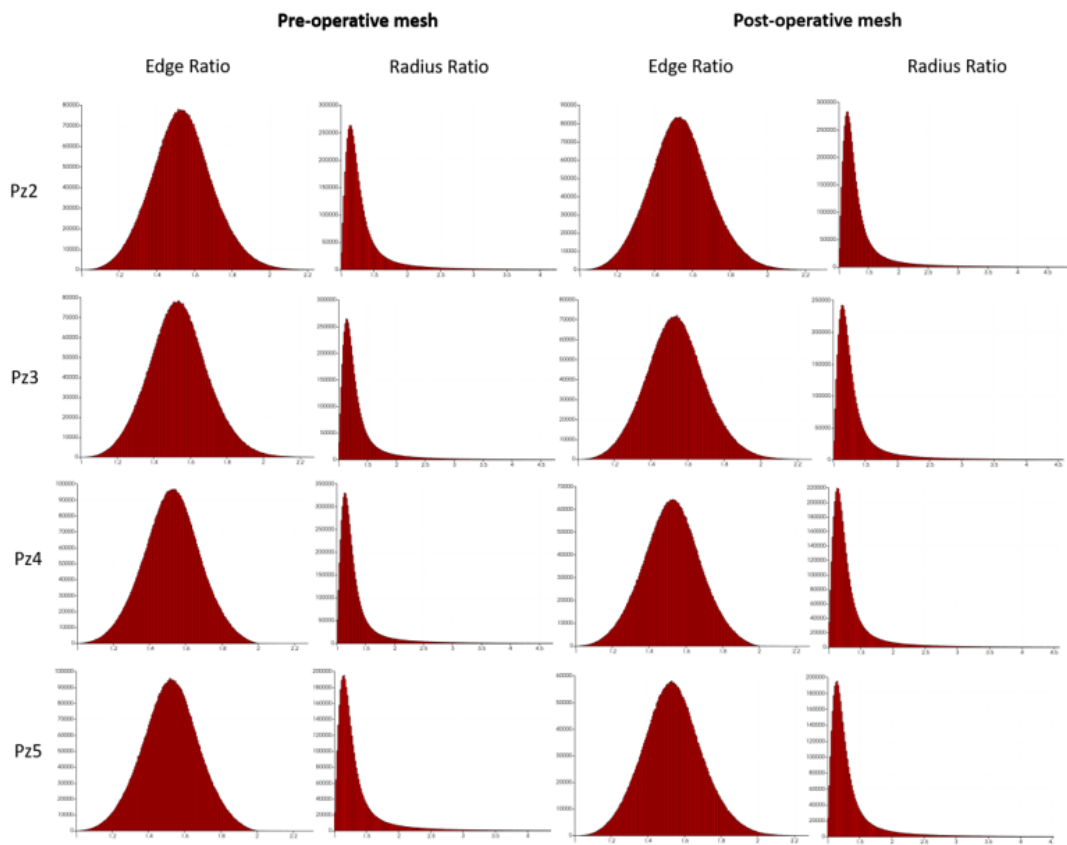
Figure B.1: Mesh quality parameters distribution

Appendix C

Hemodynamic and Biomechanical quantities

ProxOSI[-]	Pre-intervention			Post-intervention		
	10^{th}perc	Median	90^{th}perc	10^{th}perc	Median	90^{th}perc
Patient 1	0.014	0.044	0.223	0.047	0.111	0.287
Patient 2	0.080	0.146	0.265	0.070	0.144	0.262
Patient 3	0.057	0.1307	0.230	0.060	0.153	0.316
Patient 4	0.079	0.146	0.2867	0.053	0.206	0.370
Patient 5	0.052	0.1159	0.352	0.050	0.293	0.406

Table C.1: 10th percentile, Median and 90th percentile of pre and post intervention OSI in proximal portion of descending aorta

OSI[-]	Pre-intervention			Post-intervention		
	10^{th}perc	Median	90^{th}perc	10^{th}perc	Median	90^{th}perc
Patient 1	0.0136	0.051	0.260	0.048	0.113	0.279
Patient 2	0.085	0.155	0.280	0.0800	0.153	0.276
Patient 3	0.063	0.147	0.274	0.054	0.146	0.306
Patient 4	0.093	0.161	0.266	0.066	0.212	0.355
Patient 5	0.045	0.152	0.339	0.076	0.225	0.380

Table C.2: 10th percentile, Median and 90th percentile of pre and post intervention OSI of the whole descending aorta

ProxWSS[Pa]	Pre-intervention			Post-intervention		
	10^{th}perc	Median	90^{th}perc	10^{th}perc	Median	90^{th}perc
Patient 1	1.815	3.142	4.233	2.343	3.713	5.283
Patient 2	1.364	2.016	3.184	1.460	2.381	4.000
Patient 3	1.598	2.725	3.761	1.232	2.064	2.964
Patient 4	1.225	1.749	2.647	0.995	1.616	2.983
Patient5	1.390	2.109	3.194	0.567	1.282	2.128

Table C.3: 10th percentile, Median and 90th percentile of pre and post intervention WSS in the proximal portion of descending aorta

WSS[Pa]	Pre-intervention			Post-intervention		
	10^{th}perc	Median	90^{th}perc	10^{th}perc	Median	90^{th}perc
Patient 1	2.107	3.044	3.764	2.895	3.790	4.710
Patient 2	1.512	2.260	2.877	1.579	2.420	3.463
Patient 3	1.894	2.788	3.503	1.4337	2.169	2.760
Patient 4	1.322	1.962	2.491	1.102	1.993	2.725
Patient 5	1.526	2.044	2.810	0.727	1.217	1.866

Table C.4: 10th percentile, Median and 90th percentile of pre and post intervention WSS of the whole descending aorta

ProxStrains [%]	Pre-intervention			Post-intervention		
	10^{th}perc	Median	90^{th}perc	10^{th}perc	Median	90^{th}perc
Patient 1	4.428	5.355	6.702	4.626	5.551	7.008
Patient 2	4.992	6.665	8.751	5.053	6.358	8.706
Patient 3	5.167	6.393	8.037	5.931	7.449	9.906
Patient 4	4.856	5.754	7.695	4.735	5.594	7.681
Patient 5	3.838	5.510	7.273	3.415	4.630	6.628

Table C.5: 10th percentile, Median and 90th percentile of pre and post intervention Strain in the proximal tract of descending aorta

Strains[%]	Pre-intervention			Post-intervention		
	10^{th}perc	Median	90^{th}perc	10^{th}perc	Median	90^{th}perc
Patient 1	4.490	5.426	6.328	4.594	5.495	6.371
Patient 2	5.377	6.590	7.963	5.416	6.636	7.934
Patient 3	5.472	6.435	7.558	6.380	7.514	8.995
Patient 4	4.908	5.589	6.703	4.806	5.572	6.818
Patient 5	4.310	5.612	6.807	3.747	5.024	6.263

Table C.6: 10th percentile, Median and 90th percentile of pre and post intervention Strain of the whole descending aorta
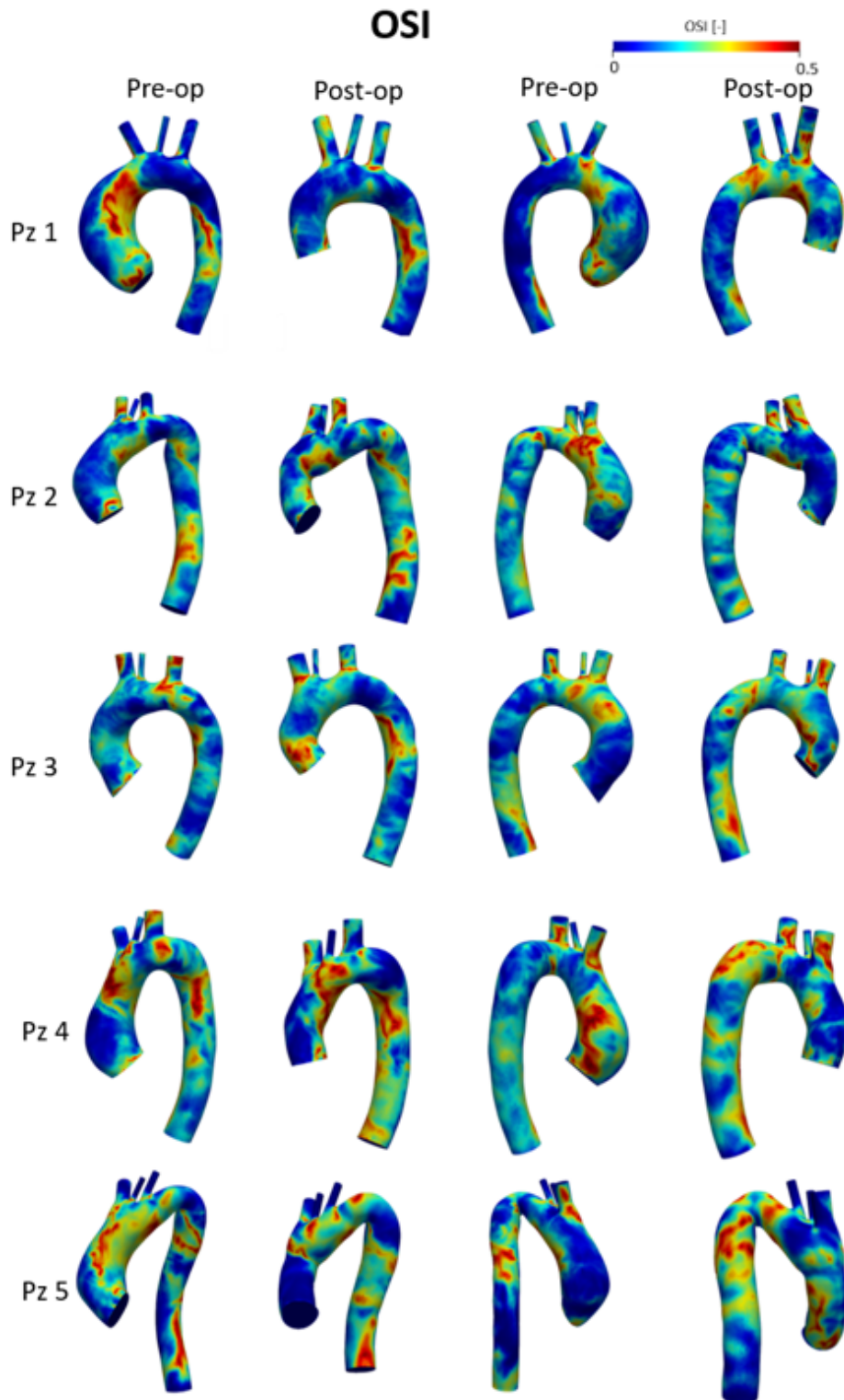
Figure C.1: OSI distribution in frontal and posterior aorta views for both pre and post-surgical cases
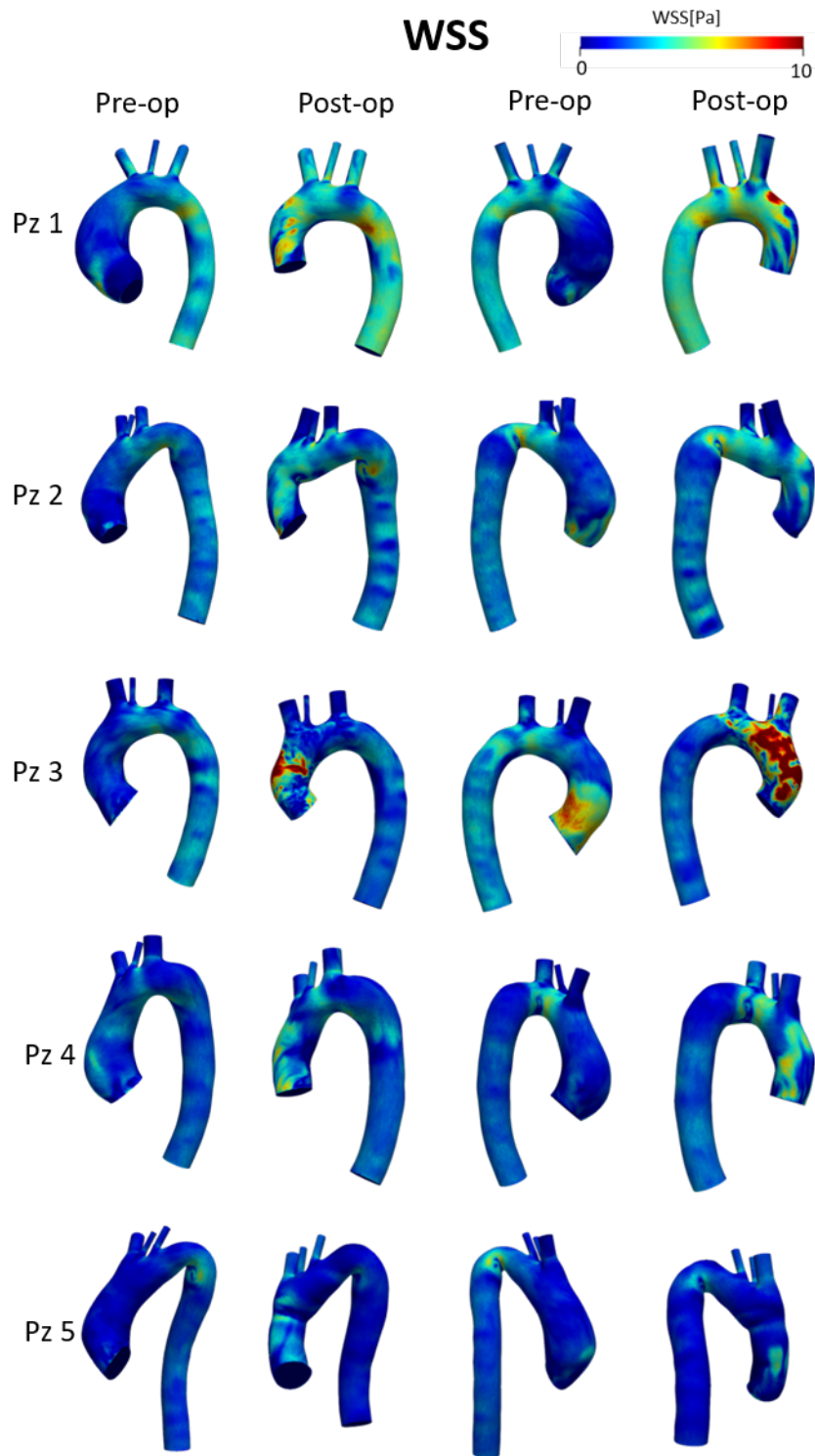
Figure C.2: WSS distribution in frontal and posterior aorta views for both pre and post-surgical cases
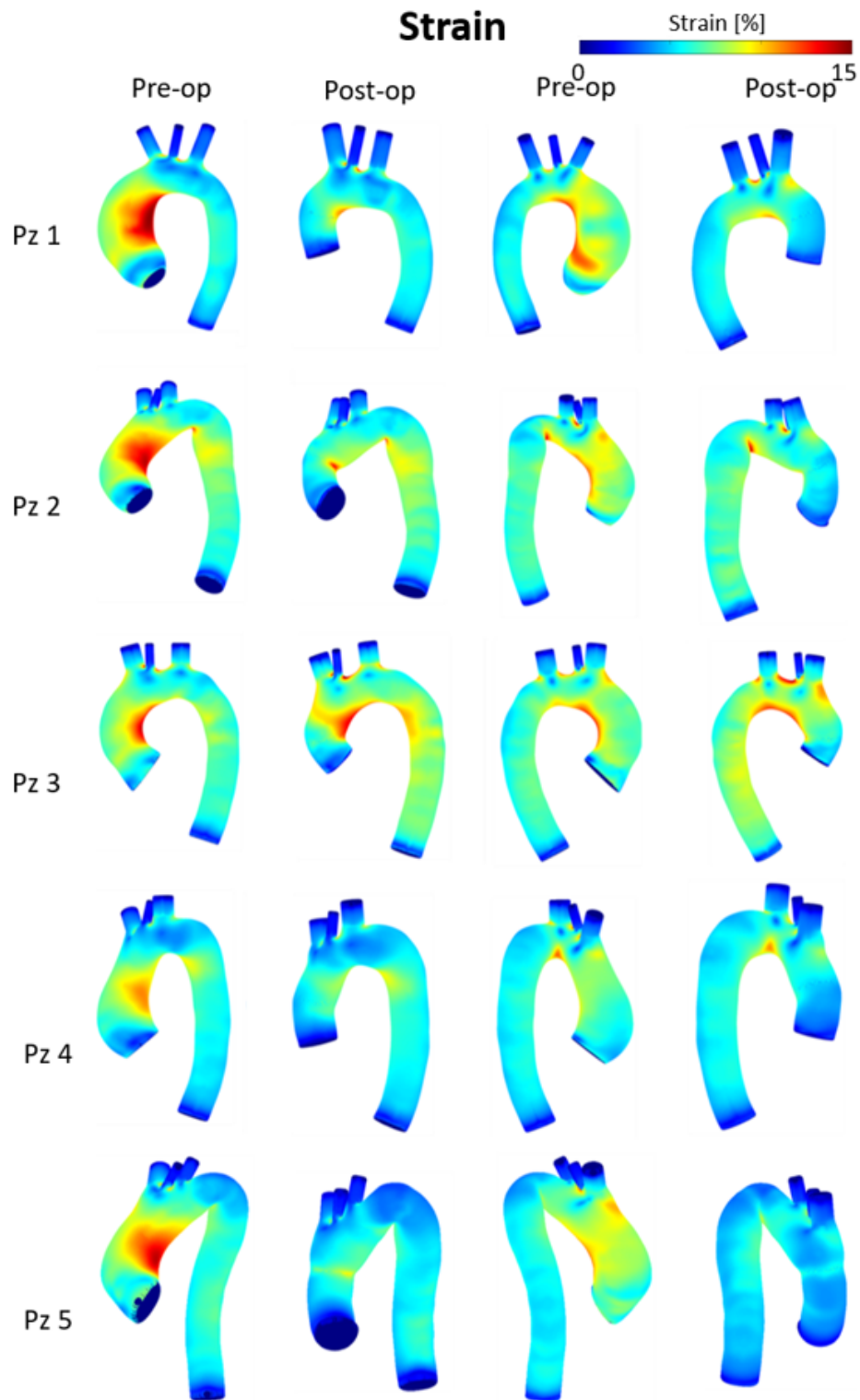
Figure C.3: Strain distribution in frontal and posterior aorta views for both pre and post-surgical cases

Bibliography

[1] J. A. Elefteriades, J. A. Rizzo. Acute aortic disease. *1st edn. Ch. 5 (ed. Elefteriades, J.) 89–98*, 2007.

[2] L. K. et al. Bickerstaff. Thoracic aortic aneurysms: a population-based study. *Surgery 92, 1103–1108*, 1982.

[3] W. D. et al Clouse. Improved prognosis of thoracic aortic aneurysms: a population-based study. *JAMA 280, 1926–1929*, 1998.

[4] Natural history of thoracic aortic aneurysms. *J. Vasc. Surg. 56, 565–571*, 2012.

[5] Centers for disease control and prevention. leading causes of death and injury. cdc https://www.cdc.gov/ injury/wisqars/leadingcauses.html. 2020.

[6] Kron IL Fonner E Crosby IK Gazoni LM, Speir AM. Elective thoracic aortic aneurysm surgery: better outcomes from high-volume centers. *J Am Coll Surg 210: 855–9; discussion: 859–60*, 2010.

[7] McCullough JN et al. Ehrlich MP, Ergin MA. Predictors of adverse outcome and transient neurological dysfunction after ascending aorta/hemiarch replacement. *Ann Thorac Surg 69: 1755–63*, 2000.

[8] O. Vardoulis, E. Coppens, B. Martin, P. Reymond, P. Tozzi, and N. Stergiopulos. Impact of aortic grafts on arterial pressure:

A computational fluid dynamics study. *European Society for Vascular Surgery. Published by Elsevier Ltd. All rights reserved. doi:10.1016/j.ejvs.2011.08.006*, 2011.

[9] Sagawa K. Cardiac contraction and the pressure-volume relationship. *New York: Oxford University Press;*, 1988.

[10] Karol Calò Valentina Mazzi Diego Gallo Francesca Condemi Solmaz Farzaneh Stéphane Avril Umberto Morbiducci Giuseppe De Nisco, Paola Tasso. Deciphering ascending thoracic aortic aneurysm hemodynamics in relation to biomechanical properties. *Medical Engineering Physics,Volume 82, pages 119-129*, 2020.

[11] Guido Nannini. Assessment of ascending thoracic aortic aneurysm prior and after valve sparing surgery: a patient tailored fluid-structure interaction model enhanced with 4d flow mri. Master's thesis, Politecnico di Milano, 2020.

[12] C. A. Figueroa. A coupled-momentum method to model blood flow and vessel deformation in human arteries: applications in disease research and simulation-based medical planning. *PhD Thesis*, 2006.

[13] P. A. Yushkevich et al. User-guided 3d active contour segmentation of anatomical structures: Significantly improved efficiency and reliability. *Neuroimage 31.3, pp. 1116-1128*, 2006.

[14] D. A. Bluemke C.-Y. Liu, D. Chen and W. G. Hundley. Evolution of aortic wall thickness and stiffness with atherosclerosis: Long-term follow up from the multi-ethnic study of atherosclerosis (mesa),. *HHS Public Access vol. 69, no. 1, pp. 110–120, doi: 10.1016/j.socscimed.2009.04.010*, 2015.

[15] W. Karel van den Hengel. Abdominal aortic wall thickness and compliance the possibilities to measure and the effect of variation in the analysis of aneurysms. *Blood, no. April*, 2008.

[16] J. Vappou P. Terdtoon T. Khamdaeng, J. Luo and E. E. Konofagou. Arterial stiffness identification of the human carotid artery using the stress – strain relationship in vivo,. *Ultrasonics, vol. 52, no. 3, pp. 402–411, doi: 10.1016/j.ultras.2011.09.006*, 2012.

[17] Matteo Selmi MS Emiliano Votta PhD Paola Redaelli MD Francesco Sturla PhD Alberto Redaelli PhD Giordano Tasca, MD and MD Amando Gamba. Aortic root biomechanics after sleeve and david sparing techniques: A finite element analysis. *The Society of Thoracic Surgeons 0003-4975/36.00 Published by Elsevier Inc*, 2017.

[18] Fraser M. Callaghan;Stuart M. Grieve. Normal patterns of thoracic aortic wall shear stress measured using fourdimensional flow mri in a large population. *Am J Physiol Heart Circ Physiol 315: H1174 –H1181; doi:10.1152/ajpheart.00017.2018*, 2018.

[19] C. K. Zarins D. N. Ku, D. P. Giddens and S. Glagov. Pulsatile flow and atherosclerosis in the human carotid bifurcation. positive correlation between plaque location and low and oscillating shear stress. *Arteriosclerosis, vol. 5, no. 3, pp. 293– 302, doi: 10.1161/01.atv.5.3.293*, 1985.

[20] simone Bartesaghi; Giorgio Colombo. Un processo virtuale automatico in supporto alla diagnosi e trattamento di un aneurisma dell'aorta addominale. *analisi e calcolo*, 2013.

[21] Simone Saitta; Selene Pirola; Filippo Piatti; Emiliano Votta; Federico Lucherini;Francesca Pluchinotta; Mario Carminati; Massimo Lombardi;

Christian Geppert;Federica Cuomo; Carlos Alberto Figueroa; Xiao Yun
Xu; Alberto Redaelli. Evaluation of 4d flow mri-based non-invasive
pressure assessment in aortic coarctations. *Journal of Biomechanics 94
13–21*, 2019.

[22] Rong LQ; Palumbo MC; Rahouma MM; Meineri M; Arguelles GR; Kim J
et al. Immediate of impact prosthetic graft replacement of the ascending
aorta on circumferential strain in the descending aorta. *Eur J Vasc
Endovasc Surg.10.1016/j.ejvs.2019.05.003*, 2019.

[23] E. M Isselbacher. Thoracic and abdominal aortic aneurysms. *Circulation
111, 816–828*, 2005.

[24] L. F. et al. Hiratzka. 2010 accf/aha/aats/acr/asa/ sca/scai/sir/sts/svm
guidelines for the diagnosis and management of patients with thoracic
aortic disease: a report of the american college of cardiology
foundation/american heart association task force on practice guidelines,
american association for thoracic surgery, american college of radiology,
american stroke association, society of cardiovascular anesthesiologists,
society for cardiovascular angiography and interventions, society of
interventional radiology, society of thoracic surgeons, and society for
vascular medicine. *Circulation 121, e266–e369*, 2010.

[25] R. et al. Erbel. 2014 esc guidelines on the diagnosis and treatment of
aortic diseases: document covering acute and chronic aortic diseases of
the thoracic and abdominal aorta of the adult. the task force for the
diagnosis and treatment of aortic diseases of the european society of
cardiology (esc). *Eur. Heart J.35, 2873–2926*, 2014.

[26] O.A. Jarral D.P. O'Regan J.R. Pepper T. Athanasiou X.Y. Xu S. Pirola,
Z. Cheng. On the choice of outlet boundary conditions for patient-specific

analysis of aortic flow using computational fluid dynamics. *Journal of Biomechanics*, 2017.

[27] Kromhout D on behalf of the Task Force. Sans S, Kesteloot H. Task force of the european society of cardiology on cardiovascular mortality and morbidity statistics. europe.18: 1231–48. *Eur Heart*, 1997.

[28] F. Dagenais. Aorta published in thoracic surgery clinics. *Pubmed*, 2011.

[29] Gerard J. Tortora. *Principles of Human Anatomy (Seventh ed.)*. Harper Collins, 1995.

[30] Christopher P. Cheng B. Ullery, G. Suh. Chapter 8 - thoracic aorta and supra-aortic arch branches. *Academic Press,ISBN 9780128157138*, 2019.

[31] Eagle K.A. Bossone, E. Epidemiology and management of aortic disease: aortic aneurysms and acute aortic syndromes,https://doi.org/10.1038/s41569-020-00472-6. *Nat Rev Cardiol*, 2020.

[32] Farkas EA Elefteriades JA. Thoracic aortic aneurysm clinically pertinent controversies and uncertainties. *J Am Coll Cardiol, 55: 841–57*, 2010.

[33] Böhm M Laufs U Lavall D, Schäfers HJ. Aneurysms of the ascending aorta. *Deutsches Ärzteblatt International,Dtsch Arztebl Int 2012; 109(13): 227–33*, 2012.

[34] Dietz HC Judge DP. Marfan's syndrome. *Lancet 2005; 366: 1965–76*, 2005.

[35] Mahoney D et al. Michelena HI, Khanna AD. Incidence of aortic complications in patients with bicuspid aortic valves. *JAMA,306: 1104–12.*, 2011.

[36] https://www.umcvc.org/conditions-treatments/bicuspid-aortic-valve-bav.

[37] Carlberg B Hannuksela M, Lundqvist S. Thoracic aorta—dilated or not? *Scand Cardiovasc 40: 175–8*, 2006.

[38] Rosing DR Bondy CA Matura LA, Ho VB. Aortic dilatation and dissection in turner syndrome. *Circulation; 116: 1663–70*, 2007.

[39] Waalewijn RA et al. Cozijnsen L, Braam RL. What is new in dilata - tion of the ascending aorta? review of current literature and practical advice for the cardiologist. *Circulation 123: 924–8*, 2011.

[40] C. C. et al. Lee. Oral fluoroquinolone and the risk of aortic dissection. *C J. Am. Coll. Cardiol. 72, 1369–1378*, 2018.

[41] Henderson WG Grover FL Oprian C Rahimtoola SH Hammermeister K, Sethi GK. Outcomes 15 years after valve replacement with a mechanical versus a bioprosthetic valve: final report of the veterans affairs randomized trial. *J Am Coll Cardiol 36: 1152–8*, 2000.

[42] U. K. A. et al. Sampson. Global and regional burden of aortic dissection and aneurysms: mortality trends in 21 world regions, 1990 to 2010. *Glob. Heart 9*, 2014.

[43] W. D. et al. Clouse. Acute aortic dissection: population-based incidence compared with degenerative aortic aneurysm rupture. *Mayo Clin. Proc. 79, 176–180*, 2004.

[44] I. et al. Mészáros. Epidemiology and clinicopathology of aortic dissection. *Chest 117, 1271–1278*, 2000.

[45] MD Sharif H. Ellozy. Classification of aortic pathologies. *ENDOVASCULAR TODAY NOVEMBER 2017 VOL. 16, NO. 11*, 2017.

[46] R. et al. Erbel. 2014 esc guidelines on the diagnosis and treatment of aortic diseases: document covering acute and chronic aortic diseases of the thoracic and abdominal aorta of the adult. the task force for the diagnosis and treatment of aortic diseases of the european society of cardiology (esc). *Eur. Heart J. 35, 2873–2926*, 2014.

[47] MD Christina Long. The near-fatal panic attack. *EM Resident, Cardiology*, 2018.

[48] https://sites.google.com/a/tamaki.ac.nz/mrs-smallwood-s-science-site/ spectroscopy/nuclear-magnetic-resonance-nmr.

[49] Kevin M Brindle. New approaches for imaging tumour responses to treatment - scientific figure on researchgate.

[50] Takeda K Higgins CB. Sakuma H, Kawada N. Mr measurement of coronary blood flow. *J Magn Reson Imaging; 10:728–733*, 1999.

[51] Christian Meier PhD Andreas Leppert MD Michael Galanski MD Joachim Lotz, MD. Cardiovascular flow measurement with phase-contrast mr imaging: Basic facts and implementation. *Ragiographics 22.3 pp. 651-671*, 2002.

[52] Julio Garcia Kelly B. Jarvis Michael Markl Zoran Stankovic, Bradley D. Allen. 4d flow imaging with mri. *Cardiovasc Diagn Ther,173-192*, 2014.

[53] Pelc NJ. Bernstein MA, Shimakawa A. Minimizing te in moment-nulled or flow-encoded two- and three-dimensional gradient-echo imaging. *J Magn Reson Imaging 583-8*, 1992.

[54] Shimakawa A et al. Pelc NJ, Bernstein MA. Encoding strategies

for three-direction phase-contrast mr imaging of flow. *J Magn Reson Imaging;1:405-13.*, 1991.

[55] Markl M. Johnson KM. Improved snr in phase contrast velocimetry with five-point balanced flow encoding. *Magn Reson Med 63:349-55*, 2010.

[56] Lorenz R et al. Bock J, Frydrychowicz A. In vivo noninvasive 4d pressure difference mapping in the human aorta: phantom comparison and application in healthy volunteers and patients. *Magn Reson Med; 66:1079-88*, 2011.

[57] Hardy CJ et al. Bolster BD Jr, Atalar E. Accuracy of arterial pulse-wave velocity measurement using mr. *J Magn Reson Imaging; 8:878-88.*, 1998.

[58] Kvitting JP et al. Dyverfeldt P, Sigfridsson A. Quantification of intravoxel velocity standard deviation and turbulence intensity by generalizing phase-contrast mri. *Magn Reson Med ;56:850-8.*, 2006.

[59] D. D. Blatter C. Tang and D. L. Parker. Accuracy of phase-contrast flow measurements in the presence of partial-volume effects. *J. Magn. Reson. Imaging, vol.3, no. 2, pp. 377–385, doi: 10.1002/jmri.1880030213*, 1993.

[60] D. D. Blatter C. Tang and D. L. Parker. Accuracy of phase-contrast flow measurements in the presence of partial-volume effects. *Journal of Magnetic Resonance Imaging 3.2, pp. 377 (385)*, 1993.

[61] McCormick M et al. Smith N, de Vecchi A. euheart: personalized and integrated cardiac care using patient-specific cardiovascular modelling. *Interface Focus;1:349–64.*, 2011.

[62] Swedenborg J et al. Gasser TC, Nchimi A. A novel strategy to translate the biomechanical rupture risk of abdominal aortic aneurysms to their

equivalent diameter risk: method and retrospective validation. *Eur J Vasc Endovasc Surg;47:288–95.*, 2014.

[63] A. D. Caballero and S. Laín. A review on computational fluid dynamics modelling in human thoracic aorta. *Cardiovasc. Eng. Technol., vol. 4, no. 2, pp. 103–130, doi: 10.1007/s13239-013-0146-6.*, 2013.

[64] Katsamouris AN Startchik I Kalangos A Licker MJ et al Ioannou CV, Stergiopulos N. Hemodynamics induced after acute reduction of proximal thoracic aorta compliance. *Eur J Vasc Endovasc Surg 2003 Aug;26(2):195e204*, 2003.

[65] Zamir M. Alderson H. Effects of stent stiffness on local haemodynamics with particular reference to wave reflections. *J Biomech Mar;37(3):339e48*, 2004.

[66] Takeda A. Murakami T. Enhanced aortic pressure wave reflection in patients after repair of aortic coarctation. *Ann Thorac Surg Sep;80(3):995e9*, 2005.

[67] Annie Ruimi Raja Jayendiran, Bakr Nour. Computational fluid–structure interaction analysis of blood flow on patient-specific reconstructed aortic anatomy and aneurysm treatment with dacron graft. *https://doi.org/10.1016/j.jfluidstructs.2018.06.008 0889-9746 Elsevier Ltd*, 2018.

[68] N.;Mekow J. Lan H. Marsden A. l. Updegrove A., Wilson and S. C Shadden. Simvascular - an open source pipeline for cardiovascular simulation. *Annals of Biomedical Engineering 45: 525 DOI:10.1007/s10439-016-1762-8*, 2017.

[69] Milewicz DiM Michel JB, Jondeau G. From genetics to response to injury: vascular smooth muscle cells in aneurysms and dissections of the

ascending aorta,. *Cardiovasc Res; 114:578–89, doi: 10.1093/cvr/cvy006 .*, 2018.

[70] Viallon M Croisille P Avril S. Condemi F, Campisi S. Relationship between as- cending thoracic aortic aneurysms hemodynamics and biomechanical proper- ties. *IEEE Trans Biomed Eng;67:949–56. doi: 10.1109/TBME.2019.2924955 .*, 2019.

[71] G.S.Settles M.J. Lawson B.A. Craven, E.G. Paterson. Development and verification of a high-fidelity computational fluid dynamics model of canine nasal airflow. *Journal of Biomechanical Engineering, vol 131 7 091002-1*, 2009.

[72] P. J. Roache. Verification and validation in computational science and engineering. *Hermosa, Albuquerque, NM*, 1998.

[73] W. L. Oberkampf. Verification and validation in computational simulation. *Transp. Task Force Meet, vol. 21, no. 3, pp. 359–367, 2004*, 2004.

[74] P. P. P´ebay D. Thompson C. J. Stimpson, C. J. Stimpson. *The Verdict Library Reference Manual.* 2007.

[75] Nasr Esfahany M. Nasiraei Moghaddam A. Saligheh Rad H. Firouznia K. Shakiba M. Ghanaati H. Wilkinson I.D. Frangi A.F. Sarrami-Foroushani, A. Velocity measurement in carotid artery: quantitative comparison of timeresolved 3d phase-contrast mri and image-based computational fluid dynamics. *Iran. J. Radiol. Q. J. Publ. Iran. Radiol. Soc. 12,.*, 2015.

[76] Freyberg M.A. Friedl P. Kaiser, D. Lack of hemodynamic forces triggers apoptosis in vascular endothelial cells. *Biochem. Biophys. Res. Commun. 231, 586–590*, 1997.

[77] M. Gaudino et al J. Aortic flow after valve sparing root replacement with or without neosinuses reconstruction. *Thorac. Cardiovasc. Surg., vol. 157, no. 2, pp. 455–465,*, 2019.

[78] Stephane Avril Rossella Campobasso; Francesca Condemi; Magalie Viallon; Pierre Croiselle; Salvatore Campisi. Evaluation of peak wall stress in an ascending thorcic aortic aneurysm using fsi simulations: Effect if aortic stiffness and peripheral resistane. *Cardiovascular engineering and technology, Vol 9, No 4, pp.707-722,https://doi.org/10.1007/s13239-018-00385-z*, 2018.

[79] Lisa Q. Rong; Maria C. Palumbo; Mohamed Rahouma; Massimiliano Meineri; Gabriel R. Arguelles; Jiwon Kim; Christopher Lau; Richard B. Devereux; Kane O. Pryor; Leonard N. Girardi; Alberto Redaelli;Mario F.L. Gaudino; Jonathan W. Weinsaft;. Immediate impact of prosthetic graft replacement of the ascending aorta on circumferential strain in the descending aorta. *European Journal of Vascular and Endovascular Surgery, Volume 58, Issue 4 Pages 521-528,*, 2019.

[80] Maria C. Palumbo, Lisa Q. Rong, Jiwon Kim, Pedram Navid, Razia Sultana, Jonathan Butcher, Alberto Redaelli, Mary J. Roman, Richard B. Devereux, Leonard N. Girardi, Mario F. L. Gaudino, and Jonathan W. Weinsaft. Prosthetic aortic graft replacement of the ascending thoracic aorta alters biomechanics of the native descending aorta as assessed by transthoracic echocardiography. *PLOS ONE*, 15(3):1–16, 03 2020.

[81] Maria Chiara Palumbo, Lisa Rong, Pedram Navid, Abbas Emaminia, Jiwon Kim, Yadong Wang, Alberto Redaelli, Mary J Roman, Richard B Devereux, Leonard N Girardi, Mario Gaudino, and Jonathan W Weinsaft. Abstract 12262: Prosthetic aortic graft replacement of the

ascending thoracic aorta augments distensibility of the native descending aorta assessed via circumferential vessel wall strain. *Circulation,* 140(Suppl_1):A12262–A12262, 2019.

[82] A. et al. Evangelista. Insights from the international registry of acute aortic dissection: a 20-year experience of collaborative clinical research. *Circulation 137, 1846–1860,* 2018.

[83] J. H. et al. Dean. Cocaine-related aortic dissection: lessons from the international registry of acute aortic dissection. *Am. J. Med. 127, 878–885,* 2014.

[84] Moridzadeh R et al. Mussa F, Horton J. Acute aortic dissection and intramural hematoma: a systematic review. *JAMA 316:754-763.,* 2016.

[85] Sundt TM 3rd Eagle KA. Ramanath VS, Oh JK. Acute aortic syndromes and thoracic aortic aneurysm. *Mayo Clin Proc.84:465-481.,* 2009.

[86] O'Gara PT. Bonaca MP. Diagnosis and management of acute aortic syndromes: dissection, intramural hematoma, and penetrating aortic ulcer. *Curr Cardiol Rep.16:536.,* 2014.

[87] T.J.R. Hughes C.A. Taylor and C.K. Zarins. Finite element modeling of blood flow in arteries. *Computer Methods in Applied Mechanics and Engineering 158, 155-196.,* 10998.

[88] T. Kobayashi N. Taniguchi M. Oshima, R. Torii and K. Takagi. Finite element simulation of blood flow in the cerebral artery. *Computer Methods in Applied Mechanics and Engineering 191(6-7),661-671,* 2001.

[89] K. Perktold and G. Rappitsch. Computer simulation of local blood flow and vessel mechanics in a compliant carotid artery bifurcation model. *Journal of Biomechanics 28(7) 845-856,* 1995.

[90] C.H.G.A. van Oijen D. Bessems T.W.M. Gunther A. Segal B.J.B.M. Wolters J.M.A. Stijnen F.N. van de Vosse, J. de Hart and F.P.T. Baaijens. Finite-element-based computational methods for cardiovascular fluid-structure interaction. *Journal of Engineering Mathematics 47(3/4) 335-368*, 2003.

[91] L. De Pater and J. Van Den Berg. An electric analogue of the entire human circulatory system. *Medical electronics and biological engineering 2 161-166.*, 1964.

[92] C.J. De Vries N. Westerhof, F. Bosman and A. Noordergraaf. Analog studies of the human systemic arterial tree. *Journal of Biomechanics 2 121-143.*, 1969.

[93] T.J.R. Hughes and J. Lubliner. On the one-dimensional theory of blood flow in the larger vessels. *Mathematical Biosciences 18(1-2) 161-170*, 1973.

[94] S.A. Spicer S. Strohband G.R. Feijoo T.J.R. Hughes J. Wan, B.N. Steele and C.A. Taylor. A one-dimensional finite element method for simulation-based medical planning for cardiovascular disease. *Computer Methods in Biomechanics and Biomedical Engineering 5(3) 195-206.*, 2002.

[95] von Tengg-Kobligk H et al. Morris PD, Narracott A. Computational fluid dynamics modelling in ardiovscualr medicine. *Heart;102:18–28.*, 2016.

[96] Chien S. Mechanotransduction and endothelial cell homeostasis: the wisdom of the cell. *Am J Physiol Heart Circ Physiol ;292:H1209–24*, 2007.

[97] Olson LE Molthen RC et al. LaDisa JF, Jr. Alterations in wall shear stress predict sites of neointimal hyperplasia after stent implantation in rabbit iliac arteries. *Am J Physiol Heart Circ Physiol;288:H2465–75.*, 2005.

[98] Nickisch H et al. Weese J, Groth A. Generating anatomical models of the heart and the aorta from medical images for personalized physiological simulations. *Med Biol Eng Comput; 51:1209–19.*, 2013.

[99] Marzo A et al. Brown AG, Shi Y. Accuracy vs. computational time: translating aortic simulations to the clinicj biomech 2012;45:516–23. *J Biomech;45:516–23.*, 2012.

[100] R. P. Deveja E. P. Kritharis D. Perrea G. D. Sionis K. Toutouzas et al. Iliopoulos, D. C. Regional and directional variations in the mechanical properties of ascending thoracic aortic aneurysms. *Med. Eng. Phys. 31(1):1–9. h ttps://doi.org/10.1016/j.medengphy.2008.03.002*, 2009.

[101] Salvatore Pasta, Antonino Rinaudo, Angelo Luca, Michele Pilato, Cesare Scardulla, Thomas G.Gleason, and David A. Vorp. Difference in hemodynamic and wall stress of ascending thoracic aortic aneurysms with bicuspid and tricuspid aortic valve. *2013ElsevierLtd. http://dx.doi.org/10.1016/j.jbiomech.2013.03.029*, 2013.

[102] James Thunes PhD Trevor Kickliter BS Marie Billaud PhD Julie A. Phillippi PhD David A. Vorp PhD Spandan Maiti PhD Leonid Emerel, MD and MD Thomas G. Gleason. Predissection-derived geometric and distensibility indices reveal increased peak longitudinal stress and stiffness in patients sustaining acute type a aortic dissection: Implications for predicting dissection. *The Journal of Thoracic and Cardiovascular Surgery*, 2018.

[103] P. J. Roache. Perspective—a method for uniform reporting of grid refinement studies. *ASME J. Fluids Eng., 1163, pp. 405–413*, 1994.

[104] G. Rizzo M. Cadioli A. Esposito F. De Cobelli A. Del Maschio F.M. Montevecchi A. Redaelli U. Morbiducci, R. Ponzini. In vivo quantification of helical blood flow in human aorta by time-resolved three-dimensional cine phase contrast magnetic resonance imaging. *Annals of Biomedical Engineering, Vol. 37, No. 3, March 2009 (2008) pp. 516–531, DOI: 10.1007/s10439-008-9609-6*, 2008.

[105] Palumbo MC; Rong LQ; Kim J; Navid P; Sultana R; Butcher J; Redaelli A; Roman MJ; Devereux RB; Girardi LN; Gaudino MFL; Weinsaft JW. Prosthetic aortic graft replacement of the ascending thoracic aorta alters biomechanics of the native descending aorta as assessed by transthoracic echocardiography. *PLoS One 15(3):e0230208*, 2020.

[106] D. N. Ghista S. C. M. Yu J. M. Zhang, L. P. Chua and Y. S. Tan. Numerical investigation and identification of susceptible sites of atherosclerotic lesion formation in a complete coronary artery bypass model. *Med. Biol. Eng. Comput., vol. 46, no. 7, pp 689–699*, 2008.

[107] Piatti F; Sturla F; Bissell MM; Pirola S; Lombardi M; Nesteruk I; Della Corte A; Redaelli ACL;Votta E. 4d flow analysis of bav-related fluid-dynamic alterations: Evidences of wall shear stress alterations in absence of clinically-relevant aortic anatomical remodeling. *Front. Physiol. 8:441.*, 2017.

[108] J. Bock1; B. W. Kreher1; J. Hennig1; and M. Markl1. Optimized pre-processing of time-resolved 2d and 3d phase contrast mri data. *Proc. Intl. Soc. Mag. Reson. Med. 15*, 2007.

[109] Laird: Smart Technology Delivered. *Datasheet UltraTECTM Series UT15-24-F2-5252 Thermoelctric Module*, 2016.

[110] Yen Kheng Tan. *Energy Harvesting Autonomous Sensor Systems*. Libri SANDIT, Boca Raton, Londono, New York, 2013.

List of Figures

List of Tables